Biophysical Mechanisms of Spike Generation in Direction Selective Ganglion Cells

---

A Thesis

Presented to

The Division of Mathematics and Natural Sciences

Reed College

In Partial Fulfillment

of the Requirements for the Degree

Bachelor of Arts

Owen Gross

May 2004

Approved for the Division
(Physics)

Johnny Powell	Patrick Roberts

Acknowledgements

I would like to express my gratitude to Johnny Powell and Patrick Roberts. I can not imagine a more ideal combination of advisors for this project. Johnny's passion for physics, and life in general, is nothing short of inspiring. This thesis would not be possible without his willingness to explore an unfamiliar topic with me, and his dedication to fully understanding the material has produced an invaluable attention to detail. Patrick's extensive knowledge of the subject allowed the research to proceed past a number of staggering obstacles. I am particularly appreciative of his patience and instruction as I plodded through introductory concepts, not to mention the time he sacrificed to fit me into an already busy schedule. Finally, I would like to thank Christin for her support through the entire process.

Table of Contents

List of Figures

Abstract

First-order Wiener kernels are calculated from extracellular and intracellular recordings of Direction Selective (DS) ganglion cells and used to predict spike bursts, which are compared to spike-train predictions from a Hodgkin-Huxley (HH) like model [T. F. Weiss, *Cellular Biophysics* Vol. 2 (MIT Press, Cambridge, MA, 1996)] of the cells created in *Mathematica*. A reverse correlation method is used to calculate the kernels [P. Dayan and L. Abbot, *Theoretical Neuroscience* (MIT Press, Cambridge, MA, 2001)], which are convolved with the stimulus to estimate the response. Approximately 75% to 85% of the bursts can be predicted using this method, as demonstrated in Chapter 5.

The HH spike-train predictions are generated by transforming the stimulus into a membrane current. This method is motivated by the hypothesis that the DS cells respond linearly to stimulus velocities. The HH predictions are generally less successful than the kernel generated burst predictions. The model remains to be improved through the optimization of the method of stimulus transformation and the electrical parameters used in solving the HH equations.

The stimulus consists of an edge between a dark side and a bright side of a computer monitor that moves with random velocities along the axis parallel to the DS cell's preferred direction to stimulate the neurons. This stimulus was devised as a likely candidate to generate a high signal-to-noise ratio. Unforeseen problems arise, however, due to the temporal autocorrelations of the edge.

Chapter 1

Introduction

> As much as possible of the brain is extracted through the nostrils with an iron hook, and what the hook cannot reach is rinsed out with drugs. [1]

When Herodotus observed the Egyptians disposing of the brain without giving it a second thought, he could not have known that neuroscience, the study of the nervous system, would become the focus of an entire legion of scientists over two thousand years later. The brain was handled with utter disregard relative to the heart, which was preserved and left in the corpse because it was believed to be the seat of the mind. This idea was championed by the likes of Aristotle and therefore dominated until Galen presented evidence from dissections and experiments that hinted at the actual significance of the brain in the second century AD. Since this time, curious minds have relentlessly explored the functions responsible for cognition, memory, and the intellect in ever-increasing numbers [2].

The human nervous system is undeniably one of the most advanced computation systems fathomable, and its extreme complexity often impedes even the most well-designed research. Such complications have motivated the integration of numerous academic fields including the physical sciences, mathematics, psychology, and the biological sciences. Today, physicists find that the mechanisms responsible for intercellular communication are as rich and challenging to their quantitative skills as radiation from celestial bodies or exotic subatomic particles, much to the benefit of both neuroscience and physics. The theoretical tools that a physicist brings to the table are both numerous and invaluable. Classical electrodynamics is necessary to model the electrical properties

of cells. Solid state theory is particularly relevant to the dynamics of complex proteins. Additionally, important experimental techniques such as fluorescence resonance energy transfer (FRET) and evanescent wave microscopy, which are used to view sub-cellular processes, can only be fully explained in the language of advanced physics. In 1991 the esteemed physicist Erwin Neher was the joint recipient of a Nobel Prize for "discoveries concerning the function of single ion channels in cells." Perhaps the most significant contribution of physicists, however, can be found in the unique way in which they approach new problems.

Arguably, physics is an attempt to explain observable phenomena, which are often rather complicated, in terms of basic principles and unambiguous mathematics. As part of the scientific process, such principles are often tested by new observations and may need to be altered to explain unexpected results. Similarly, new theories may necessitate the development of new experimental techniques for the purpose of validation. Thus experimentation and theory are responsible for motivating and inspiring mutual advances. For this reason, the mathematical tools wielded by a physicist may be invaluable in a field such as biology where there is a perceived de-emphasis on the theoretical component. Referencing an allegorical glass of wine, Richard Feynman reminds us of the importance of allowing our disciplines to intermingle,

> If our small minds, for some convenience, divide this glass of wine, this universe, into parts – physics, biology, geology, astronomy, psychology, and so on – remember that nature does not know it! So let us put it back together, not forgetting ultimately what it is for. [3]

This thesis is partially intended to serve as an example of the intertwining of disciplines advocated by Feynman. Characterizing the function of a nerve cell, or neuron, is a challenging task with several possible approaches. Many of these approaches hinge on observation of the chemical interactions that occur within the cell. Such research, which may more accurately be classified as biochemistry rather than physics, tends to yield results that are more qualitative in nature.

A different approach is necessary for the desired quantitative results. For the purposes of this thesis project, neurons are considered in the language of linear response theory [4], and the biochemical processes that occur within the cells are discussed only to develop a cogent background. In this perspective, a neuron is a system that produces an

approximately linear response to an external perturbation. Specifically, a neuron is perturbed by a time-dependent visual stimulus and responds with a measurable alteration in its electric signal. Here, a "stimulus" is understood to be a specific, mathematically describable feature of the environment that is known to elicit a response in the neuron. If the stimulus is known, and the response is recorded, then the relationship between the two can be derived using the tools of theoretical physics. Apparently, the "job" of the neuron is to describe a part of the physical world using a time-dependent function.

This document will focus on the mathematical strategies used to develop a quantitative theory of stimulus encoding in retinal ganglion cells, the neurons that transmit visual information from the eye to the brain. In order to appreciate the biophysical principles that underly the response function, it is necessary to develop a picture of the brain, and more generally the entire nervous system, as a network of interacting nerve cells, or neurons. It is equally necessary, then, to discuss the processes by which neurons interact. Because the work discussed here pertains to a specific cell-type found in a relatively small subsystem within the greater nervous system, a brief discussion of the retina is required to provide a context for the discussion of retinal ganglion cells. The cells themselves will necessitate a somewhat more detailed and elaborate introduction due to the specific characteristics that differentiate retinal ganglion cells from other cell types. Several sub-types of retinal ganglion cells must also be discussed in order to complete the picture.

1.1 The Nervous System

The nervous system, which includes the brain, the spinal cord, and the peripheral nervous system, is composed of two main types of cells: neurons and the much more numerous glial cells [5]. Of these two cell types, neurons perform most of the primary functions associated with the nervous system. Sensory functions, motor functions, and functions associated with cognition are carried out by specific sets of specialized neurons, which exchange excitatory and inhibitory signals with one another. Each type of neuron uniquely processes the signals it receives from other neurons and generates a new output determined by all of the inputs it has received in a given time frame. The sub-networks formed by these specific sets are all connected, directly or indirectly, to make up the nervous system.

From a particular, simplified perspective, then, the nervous system is essentially a network of intercommunicating cells. Correspondingly, a staggering number of researchers have considered it worthwhile to pursue an understanding of the mechanisms by which neurons generate, conduct, and exchange signals. Technological advances of the twentieth century, such as increasingly sophisticated microscopes and computers, catalyzed major successes in the field of neurophysiology, and ongoing research aims to elucidate these processes down to the sub-molecular scale and in novel contexts. Throughout the major advances in this field, the central importance of the relationship between structure and function has remained constant. As an example, changes in protein conformation are believed to be responsible for ion flow through the cellular membrane [6]. A brief discussion of neuronal structure is therefore necessary rather than digressive.

Although they tend to vary greatly in size and shape, most neurons exhibit several structural features that distinguish them from other cells. Most notable of these features are the long, thin protrusions from the central neuron body, or soma, which often branch out into multiple fingers. Two distinct varieties of these protrusions exist: dendrites and axons. The aptly termed dendrites receive signals from other cells at their termini. These signals are conducted along the length of the dendrites to the soma, where all incoming signals are integrated and processed to produce an outbound signal. The output is then conducted along the cell's axon and passed on to other cells at the ends of the axon. The singular axon generally has multiple terminals and a smaller cross-section than each of the numerous dendrites. A Purkinje cell is shown in Fig. 1.1 as an example of typical neuronal structure. It is important to note, however, that like the cells themselves, the axons and dendrites come in a wide variety of sizes and shapes.

Until the mid-twentieth century, physical boundaries between neural connections were not directly observable. That is, it was not at all obvious that the dendrites and axons of neighboring cells were not continuous with one another. Consequently, the preceding decades provided the setting for an intense polemic between proponents of the reticular theory, which described the nervous system as a continuous mesh of fibers, and advocates of the neuron theory. Once sufficient evidence supporting the neuron theory had been amassed, thanks in large part to the work of Santiago Ramón y Cajal [7], the focus of the neuroscience community shifted to the processes that occur at the junctions of two cells to facilitate intercellular communication. A connection between

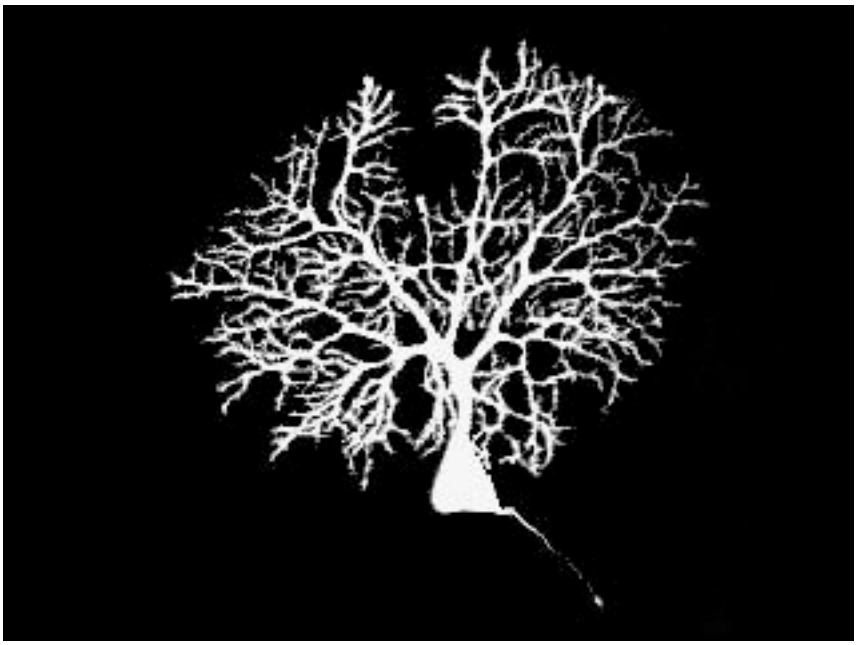

FIG. 1.1: The Purkinje cell exemplifies typical neuronal structure. The branch-like structures are dendrites. The large structure below the dendrites is the cell body or soma. The small protrusion to the bottom right is the neuron's axon. [Adapted from `www.ucl.ac.uk/lifesciences-faculty/research/neuro/`, 2004.]

an axon terminal of one cell and a dendrite of another cell is called a synapse. The region between the pre- and post-synaptic membranes is referred to as a synaptic cleft in the case of chemical transmission and a gap junction in the case of electrical transmission. A diagram of a synapse is shown in Fig. 1.2.

The main topic of discussion will be the generation of signals that are conducted along the axon to the pre-synaptic terminals, particularly in retinal ganglion cells. These signals, which are present in most types of neurons, are known as *action potentials*[1] or *spikes* for the sake of brevity. Action potentials are regenerative, non-attenuating electrical pulses. The word *action* is used to differentiate the brief (generally on the order of a milliseconds) voltage spike from the *resting* potential, which describes the negative electric potential of the materials inside of a resting neuron relative to the extracellular medium. The action potential arises when the cell becomes depolarized due to an ionic flux across the cellular membrane. The existence of the associated current was first suggested in

[1] Italics are used to emphasize terms that are centrally important to the main concepts in this document.

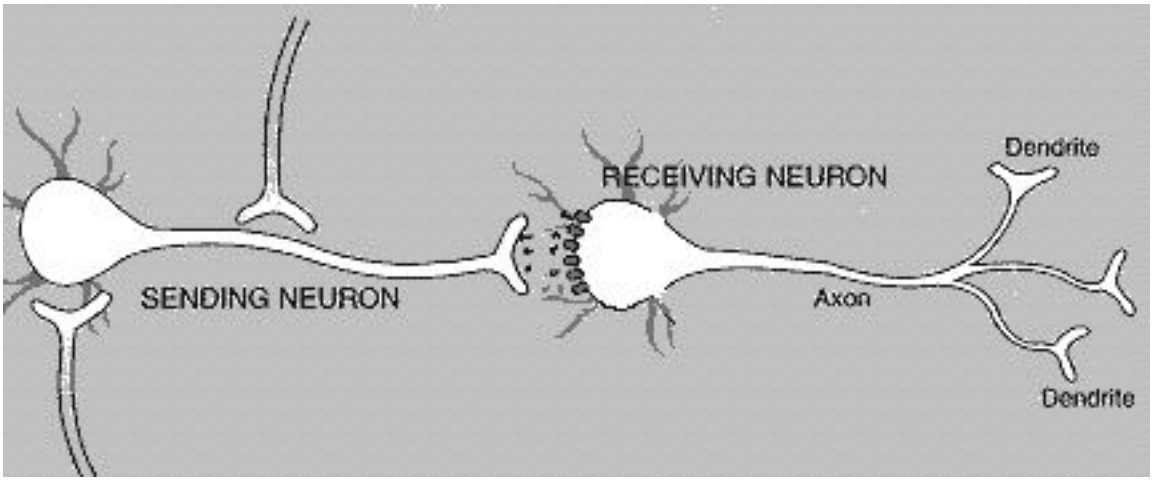

FIG. 1.2: Diagram of a synapse. The sending, or pre-synaptic, neuron releases neurotransmitter into the synaptic cleft, where it is detected by receptors on the receiving, or post-synaptic, neuron. [Adapted from `www.nap.edu`, 2004.]

1791 by an Italian physicist named Luigi Galvani, whose experimental observations led him to propose a principle he called "animal electricity." Galvani's simple experiment consisted of applying a current to the exposed tissue in the medulla of a live frog. The applied electricity caused the muscles in the frog's legs to contract [8]. From this, Galvani concluded that muscles and nerves contained electricity. Galvani's contemporaries, including the eminent scientist Alessandro Volta, questioned the bold hypothesis. Volta recognized that the frog's leg simply acted as a galvanometer responding to the the current initiated by the contact of metals used in the experiment [9]. It was apparent that the animal responded to externally applied electricity, although insufficient technology left Galvani unable to prove the existence of animal electricity by way of measurement.

In 1827 Leopoldo Nobili became the first to report measuring the current in frog tissue using an instrument of his own invention. The device, called an astatic galvanometer, was able to measure with a previously unobtainable sensitivity because it was designed to cancel the effect of Earth's magnetic field. This effect was achieved by mounting two needles in parallel, but with opposite poles adjacent to each other. The system has a net magnetic dipole moment of zero and therefore feels no net force from the Earth's magnetic field. When one of the needles is placed inside the coil carrying the current being measured, it experiences a torque, while the other needle is unaffected [10]. This

design permits the galvanometer to reach sensitivity levels sufficient for measuring the tiny (~ 1 nA) currents in living tissue.

The early measurements of biological currents mark the beginning of the field of electrophysiology, a field that is of central importance to the topics discussed in this thesis. Revelations subsequent to Nobili's experiment regarding the generation of action potentials will be discussed at length in Chapter 2.

1.2 The Retina

The voltage spikes that constitute the data for this thesis are created by retinal ganglion cells, a specific cell type in the retina. The retina, a thin tissue (~ 250 μm) at the back of the eye, possesses several attributes which make it a particularly attractive system to researchers. Most importantly, it is easy to control the input signal and possible to measure the output signal. The input is simply patterns of light, and the output consists of trains of action potentials from ganglion cells. Additionally, only five major classes of cells are involved in processing and conducting the signals, which makes the retina a relatively simple system. These five cell types are the photoreceptors, horizontal cells, bipolar cells, amacrine cells, and ganglion cells.

Although only the ganglion cells are of primary importance to this document, the organization of the retina provides a context for understanding the function of the ganglion cells and is quite interesting in itself. For the most part, each cell type constitutes its own physical layer in the tissue, as depicted by the primitive rendition of the retina in Fig. 1.3. The backmost layer relative to the lens contains the photoreceptors, which are responsible for detecting light. Rods and cones, the two main varieties of photoreceptors, are named for their distinctive shapes. The other cellular layers, which lie between the photoreceptors and the lens, must therefore be optically transparent. The frontmost layer contains mostly ganglion cells. The long axons of the ganglion cells are bundled together to form the optic nerve, which carries spikes from the retina to the brain.

A surprising amount of information processing occurs within the retina. Photoreceptors contain an abundance of the pigment rhodopsin, which undergoes a conformational change when it absorbs a photon [11]. This causes a cascade of chemical events within the cell that results in the generation of an electric signal. Bipolar cells convey these

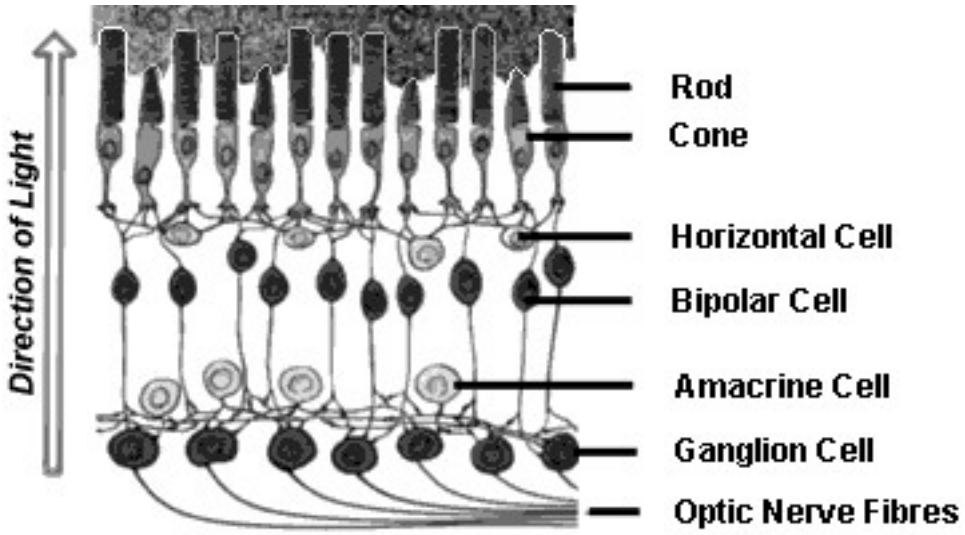

FIG. 1.3: A simplified diagram of the retina. Note the direction of the light, which passes through several cell layers before being absorbed by the photoreceptors. [Adapted from `www.catalase.com`, 2004.]

signals to the ganglion cells directly and indirectly. Direct signal conveyance generally occurs between ganglion cells and the photoreceptors nearest to them. Indirect conveyance involves horizontal cells and amacrine cells, which process information coming from more distant photoreceptors. Bipolar, horizontal, and amacrine cells will be referred to collectively as *interneurons* throughout this thesis.

Ganglion cells receive the incoming signals and produce spike trains that contain precise temporal and spatial information about the patterns of light initially detected by the photoreceptors. There are numerous types of ganglion cells, each of which conveys information about a specific feature of an image detected by the photoreceptors [11]. The next section of this chapter, however, will focus on the specific type of ganglion cell that is analyzed in the present work.

1.3 Direction Selectivity

The mammalian retina contains approximately 20 different types of ganglion cells, most of which respond to one or more specific features of a visual image, such as contrast, color, or motion [12]. Most ganglion cells produce action potentials, even when unstim-

ulated. Information about a visual stimulus is relayed to the ganglion cells in the form of excitatory or inhibitory inputs, which cause spiking frequency in the ganglion cells to increase or decrease correspondingly. When referring to a neuron that produces action potentials such as a ganglion cell, the word *response* generally refers to a notable change in spike production.

A majority of ganglion cell types are motion sensitive, meaning they respond to temporal changes in luminance within their receptive fields, corresponding both to images moving across the field of vision as well as to self-motion of the organism. The *receptive field* of a given ganglion cell is the region of the retina containing the photoreceptors that communicate with the ganglion cell through the interneurons. Exposing the receptive field of a given ganglion cell to the appropriate stimulus will elicit a response from that ganglion cell. The spatial receptive field of a ganglion cell is closely related to the area spanned by its dendrites, although studies have noted that the fields may be significantly shifted relative to one another [13]. Spatial orientation of receptive fields was an important consideration during the data analysis discussed in Chapter 5.

A subset of motion sensitive cells responds differentially to the directions of stimulus motion. These Direction Selective (DS) ganglion cells exhibit a number of interesting properties, most of which have been explored extensively throughout the last 40 years. The receptive field properties were first subjected to rigorous analysis by Barlow and Levick in 1965 [14]. They deduced that inhibitory inputs to a DS cell override excitation for movement in the cell's *null* direction, while excitatory inputs are strongly facilitated for movement in the opposite, *preferred* direction. Movement in intermediate directions produces correspondingly intermediate levels of inhibition or excitation.

Research conducted on rabbit retinas has revealed two distinct types of DS ganglion cells in the retina – On-Off DS cells and On DS cells [12]. On-Off DS cells demonstrate the characteristic DS response to the movement of a stimulus that is lighter or darker than the background field, while On DS cells are excited only by objects that are lighter than the background. Several other properties distinguish On-Off DS cells from On DS cells. Generally, On-Off DS cells respond to a wide range of stimulus speeds. On DS cells, in contrast, respond optimally to stimuli moving at slow speeds.

Four subtypes of On-Off DS cells can be classified by the orientation of the preferred direction of the cell, which points to one end either the horizontal or vertical ocular axis.

Each of the four types responds preferentially to objects moving either to the left, right, top, or bottom. The retina is completely tiled by the receptive fields of each subtype of On-Off DS cell. On DS cells comprise only three distinct subtypes; the preferred directions of each On DS cell points in one of three directions aligned with a different set of axes.

Data examined in this thesis was gathered exclusively from On-Off DS cells. Collecting data from the On-Off DS cells is somewhat simpler because they outnumber the On DS cells by about ten to one. Also, there is some interest in potential asymmetries between the responses from bright object stimulation versus the responses of dark object stimulation. Future references to DS cells will imply the On-Off variety.

1.4 Outline

Most studies of neuronal signaling over the years have been restricted to the qualitative realm. In recent years, however, advances in cellular recording techniques and cellular response theory have led to increasingly rigorous quantitative analyses of neuronal responses [15, 16]. Both the results and the methods of these recent experiments are interesting biophysical topics. This thesis combines several of these newer quantitative methods with one of the most classic results of neuroscience, the Hodgkin-Huxley (HH) model. Using these methods, more questions were raised than were answered, although the analysis of DS cell recordings found in Chapter 5 suggests several interesting possibilities. In particular, an approximately linear relationship apparently exists between the stimulus velocity and the spiking frequency of the DS cells.

The remainder of thesis is divided into two parts. The next two chapters deal purely with conceptual developments, theoretical models, and mathematics. Chapter 2 contains theory relevant to the electrical properties of neuron membranes and includes a conceptual development of the HH model, which describes major features of the membrane potential including spike generation and is used to model the response of a DS cell in the analysis section. A chronological survey of major conceptual developments is particularly useful for understanding models of the electrical properties. The theoretical background is further developed in Chapter 3 with a discussion of information coding in spike trains.

The final two chapters focus on data gathered from a series of experiments in which stimuli were presented to DS cells and their electrical responses were recorded. Chapter 4 describes the experiment used to collect data from the ganglion cells. This data is presented and analyzed extensively in Chapter 5. This chapter also summarizes the conclusions that can be drawn from the experiment and suggests potential directions for future research.

Chapter 2

Electrical Properties of Excitable Membranes

All neurons are bounded by an insulating membrane that separates the electrochemical compartment inside the cell from the surrounding extracellular space. An electric potential exists across the cellular membrane as a result of inhomogeneity in the distribution of ions between the inside and the outside of the neuron. The membrane is composed of a lipid bilayer with transmembrane proteins that serve various crucial functions. One important function of these proteins is to modulate the electric potential in response to environmental stimuli by opening and closing small pores known as *ion channels*. Because the probability of each ion channel being open depends on the value of the membrane potential, they are said to be voltage gated. In the absence of an external stimulus, the potential is held at a non-zero constant known as the resting potential, which is on the order of -40 mV in most cells. If the membrane potential is at or near the resting potential, the membrane is said to be *polarized*. When neurons receive chemical or electrical signals from other cells, they begin to depolarize. If the signals are relatively weak, the depolarization is correspondingly small and approximately linear in relation to the input. These slight depolarizations are often referred to as *graded* potentials because the amplitude decays as the potential travels along the membrane. If the signal is sufficiently strong, however, the neuron will depolarize completely and rapidly. This depolarization, known as an action potential, is brief but may occur repeatedly in a short frame of time in response to an extended or particularly strong stimulus. The amplitude of an action potential is maintained as it is conducted, as we shall see later in this chapter.

Both graded potentials and action potentials are analyzed in the experimental portion of this thesis. It is therefore desirable to discuss the basic model of membrane excitation.

The 1963 Nobel Prize in medicine was awarded to Andrew F. Huxley and Alan L. Hodgkin for their theoretical model of electrically excitable membranes and the unprecedented measurements of the membrane current [17]. The techniques used to collect the data found within this thesis are fundamentally reliant on the contributions of Hodgkin, Huxley, and their predecessors. The HH model provides a basic framework for explaining the occurrence of action potentials, a feat that eluded preceding models. Earlier models did, however, provide valuable insight regarding electrical excitation and membrane conductance. Most of these models were devised with the squid giant axon in mind, as its large size and simple cylindrical shape made it the most prominent research subject in the early years of neurophysiology, although they are generalizable to most neurons.

2.1 The Core Conductor Model

The term *electrically small* is used to describe a cell in which the membrane potential is the same along each point of the membrane at a given time. In contrast, the membrane potential of a neuron varies with position along the membrane. Consequently, neurons are said to be *electrically large* cells [18]. A comparison of an electrically small cell and an electrically large cell is shown in Fig. 2.1. Communication within and between cells relies on the propagation of localized potentials along the membrane. The core conductor model initially developed by J. Hermann explains the passive spread of potentials without reference to the excitable nature of the membrane and is thus one of the most primitive models [19]. Because of its simplicity, however, the model is a valuable pedagogical tool.

Several assumptions lie at the center of the core conductor model. The fundamental assumption poses the membrane as a boundary between two homogeneous electric conductors, the intracellular and extracellular materials. A cylindrical shape is assumed, although the results are applicable to more exotic cell shapes. The cylinders are taken to be long but with a small radius so that electrical parameters vary with the horizontal coordinate z but are independent of azimuthal coordinate θ.

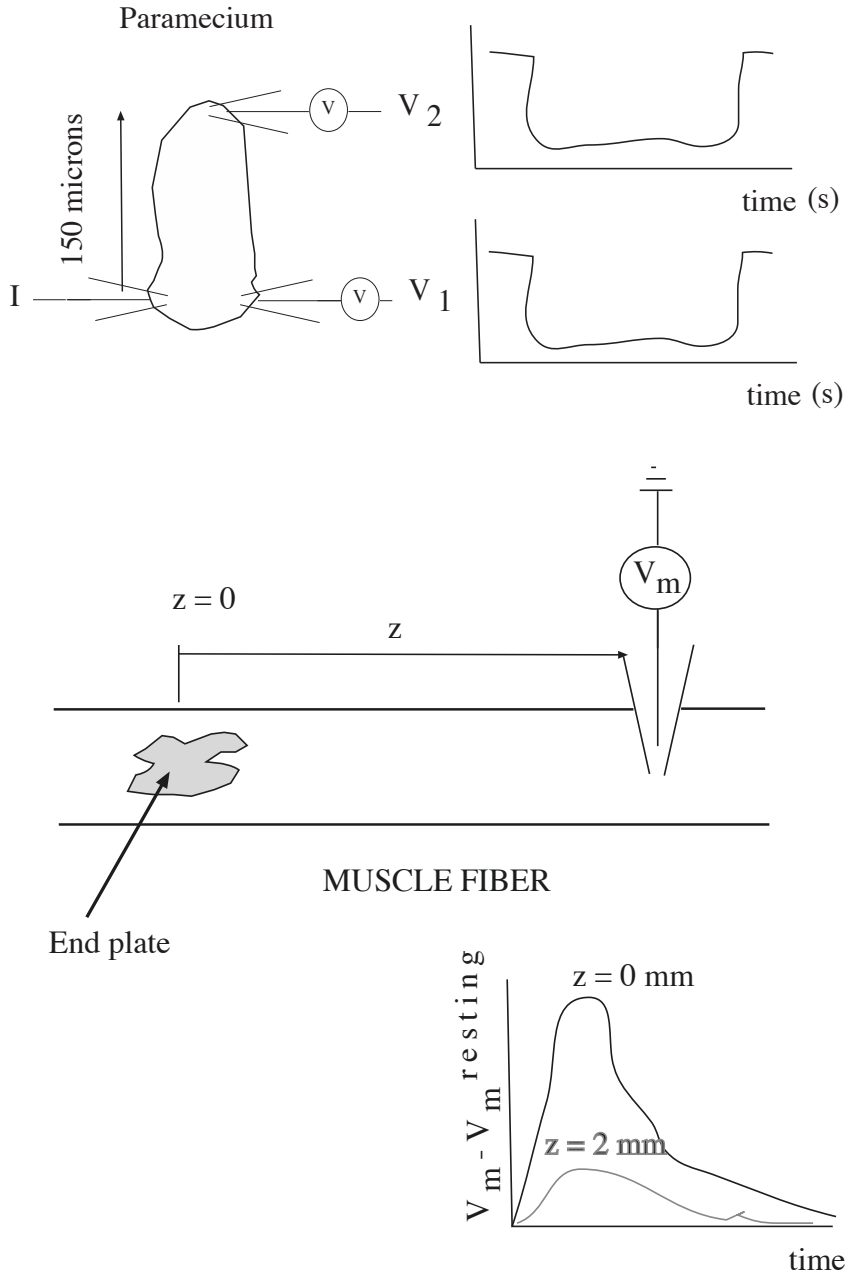

FIG. 2.1: Diagram of electrically small cell (*top*) and electrically large cell (*bottom*). The paramecium is an example of an electrically small cell; at a given time, the membrane potential is the same along each point of the membrane. On the other hand, a cell with a long axon is electrically large, and the potential attenuates as it travels along the z-axis of the axon.

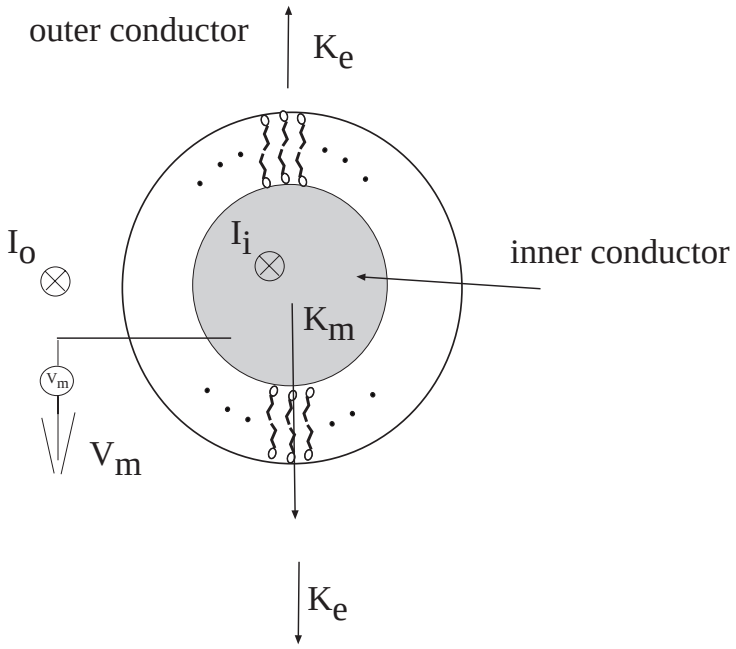

FIG. 2.2: A cross-sectional diagram of a neuron in the core conductor model. The currents I_o and I_i flow in the z direction into the page. The membrane current per unit length K_m is perpendicular to these currents. K_e is an externally applied current per unit length.

In the core conductor model, a neuron can be represented as a simple circuit [18]. Application of Kirchhoff's laws to this circuit yields an equation that describes very generally the flow of a local current around a cell membrane. Figs. 2.2 and 2.3 show a current, denoted by I_i, traveling in the z direction along the inner conductor and a current, I_o, traveling in the z direction along the outer conductor in order to form a circuit. A membrane current flows perpendicular to these currents from the inner conductor to the outer conductor. This current is expressed as a current per unit length K_m. Most experiments in which currents are measured use an externally applied current to simulate excitation from other cells. This external current, K_e, is also expressed as a current per unit length. Each of these currents depends on the position variable z as well as time. They are not denoted as vectors because they are each confined to travel along a particular axis.

Citing Kirchhoff's current rule in the context of Fig. 2.3, we can legitimately claim that

$$I_i(z,t) = I_i(z+\Delta z,t) + K_m(z,t)\Delta z\ . \tag{2.1}$$

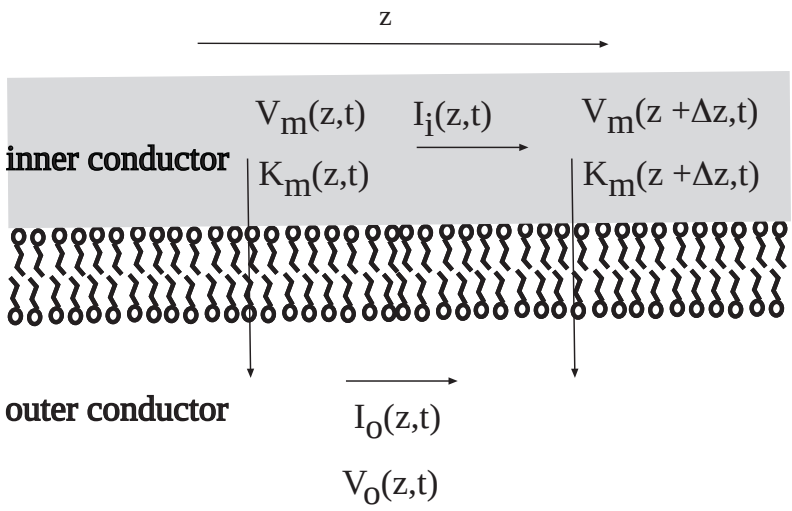

FIG. 2.3: Diagram of a small section of the membrane in the core conductor model. Note that the membrane potential $V_m(z,t)$ varies with position as well as time.

A similar application of Kirchhoff's current rule to Fig. 2.2, which shows the current due to external electrodes, yields the equation:

$$I_o(z,t) + K_m(z,t)\Delta z = I_o(z+\Delta z,t) + K_e(z,t)\Delta z\ . \tag{2.2}$$

If a resistance per unit length is defined for both the inner conductor r_i and the outer conductor r_o then the membrane shown in Fig. 2.3 can be represented in the slightly more useful form found in Fig. 2.4, and the current relations above are less obscure.

In Fig. 2.4, it should be obvious that the membrane potential V_m is the difference between the potential of the inner conductor V_i and the potential of the outer conductor V_o at a given value of z. Applying Ohm's law to the inner and outer potentials gives the following equations:

$$V_i(z,t) = V_i(z+\Delta z,t) + r_i\Delta z I_i(z+\Delta z,t), \tag{2.3}$$

$$V_o(z,t) = V_o(z+\Delta z,t) + r_o\Delta z I_o(z+\Delta z,t). \tag{2.4}$$

Eqs. (2.1), (2.2), (2.3), and (2.4) become quite suggestive if they are rearranged in a

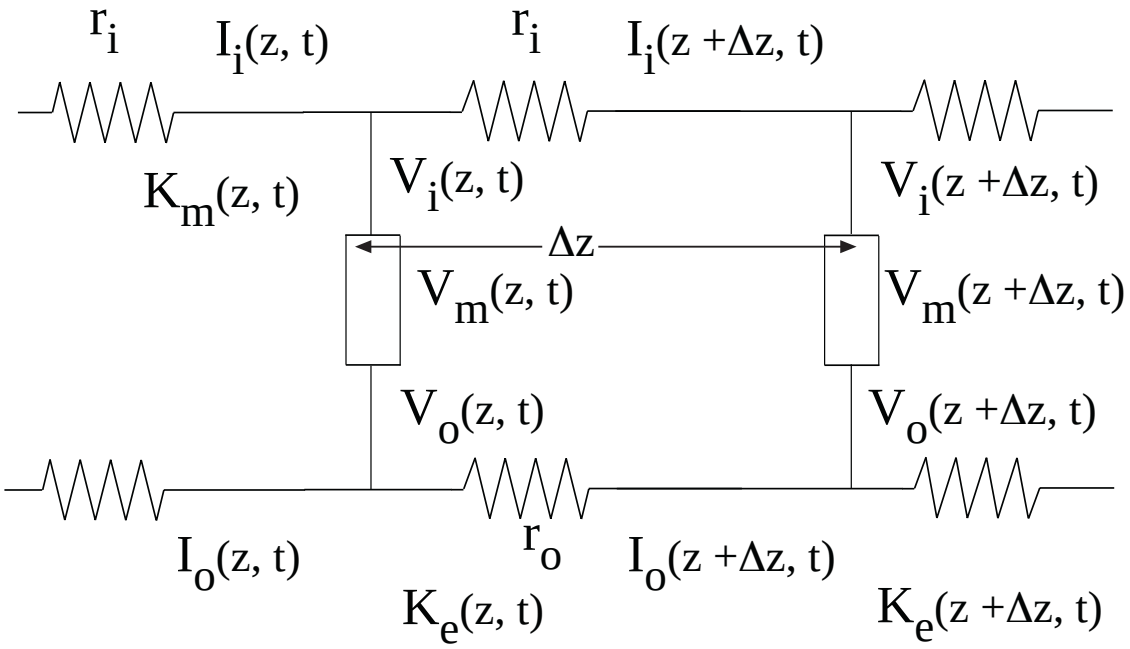

FIG. 2.4: Circuit diagram for a small section of the cellular membrane in the core conductor model. Empty boxes are used as circuit elements because the electrical properties of the cellular membrane are unspecified in the core conductor model. A factor of Δz is implied for variables expressed as linear densities such as r_o and K_i.

particular manner:

$$\frac{I_i(z+\Delta z,t)-I_i(z,t)}{\Delta z} = -K_m(z,t), \tag{2.5}$$

$$\frac{I_o(z+\Delta z,t)-I_o(z,t)}{\Delta z} = K_m(z,t)-K_e(z,t), \tag{2.6}$$

$$\frac{V_i(z+\Delta z,t)-V_i(z,t)}{\Delta z} = -r_i I_i(z+\Delta z,t), \tag{2.7}$$

$$\frac{V_o(z+\Delta z,t)-V_o(z,t)}{\Delta z} = -r_o I_o(z+\Delta z,t). \tag{2.8}$$

In the limit $z \to \infty$, we obtain the *core conductor equations*:

$$\frac{\partial I_i(z,t)}{\partial z} = -K_m(z,t), \tag{2.9}$$

$$\frac{\partial I_o(z,t)}{\partial z} = K_m(z,t)-K_e(z,t), \tag{2.10}$$

$$\frac{\partial V_i(z,t)}{\partial z} = -r_i I_i(z+\Delta z,t), \tag{2.11}$$

$$\frac{\partial V_o(z,t)}{\partial z} = -r_o I_o(z+\Delta z,t). \tag{2.12}$$

Combining Eqs. (2.11) and (2.12) with the definition of V_m leads to the relation

$$\frac{\partial V_m(z,t)}{\partial z} = -r_i I_i(z,t)+r_o I_o(z,t). \tag{2.13}$$

Taking the derivative of both sides and combining with Eqs. (2.9) and (2.10) yields

$$\frac{\partial^2 V_m(z,t)}{\partial z^2} = (r_o+r_i)K_m(z,t)-r_o K_e(z,t). \tag{2.14}$$

Eq. (2.14) is generally referred to as the *core conductor equation* [18]. Neither the membrane current or the membrane voltage can be calculated without some specific knowledge of the electrical properties of the membrane.

As it stands, however, the core conductor equation explains several properties of elec-

tric signals. Because part of the data for this thesis consists of extracellular spike train records, it is particularly important that an action potential can be detected outside of a cell, a possibility predicted by the core conductor model. If there are no externally applied currents in the vicinity of the membrane, i.e. $K_e = 0$, then Kirchhoff's current law demands $I_i(z,t) = I_o(z,t)$, in which case Eq. (2.13) can be rewritten as

$$I_o(z,t) = \frac{1}{r_o + r_i} \frac{\partial V_m(z,t)}{\partial z}. \tag{2.15}$$

Because an action potential is a sharp depolarization of the membrane potential followed by a somewhat less steep repolarization, it will be accompanied by a biphasic spike in the current outside of the cell. If $K_e \neq 0$, then the membrane current, and consequently the membrane potential, is effected accordingly. An appropriately positioned electrode with a low resistance can draw the membrane current for the purpose of recording membrane responses or apply an external current that will elicit a response from the membrane. This property is centrally important to the field of electrophysiology. Additional implications of the core conductor model are covered extensively in the relevant biophysics literature [18], though it is necessary now to consider the electric properties of the membrane itself.

2.2 The Resting Potential

In a series of papers published between 1881 and 1887, Sydney Ringer demonstrated the necessity of definite proportions of sodium, potassium, and calcium ions to the continued function of living tissue, particularly in the heart. By the mid-twentieth century it was known that the neuronal membrane is selectively permeable to certain ions, and that each type of ion flows through an independent ion channel. A measurable potential across the membrane results from different concentrations of the ions inside and outside of the cell. In the absence of outside forces, an equilibrium is achieved when diffusional forces caused by concentration differences are balanced by the electric force caused by the electric potential. The Boltzmann distribution says that the number of particles found in the z^{th} state of a system at equilibrium is proportional to $e^{-u_z/kT}$ where u_z is the potential energy of the z^{th} state, k is Boltzmann's constant, and T is absolute temperature [20].

For this two state system, the ratio of the number of particles outside the membrane to the number of particles inside the membrane is

$$\frac{n_o}{n_i} = e^{-(u_o - u_i)/kT} . \tag{2.16}$$

Here o and i are used to denote the outside and the inside of the membrane, respectively. By changing dimensions so that a number n becomes a molar concentration of some ion S and energy u becomes energy per mole U, this equation can be rewritten as

$$\frac{[S]_o}{[S]_i} = e^{-(U_o - U_i)/RT}, \tag{2.17}$$

where R is the gas constant. Taking the logarithm of both sides yields

$$U_i - U_o = RT \ln \frac{[S]_o}{[S]_i} . \tag{2.18}$$

The change in chemical potential energy, $U_i - U_o$, is equal to the work done, W, which is related to the electric potential difference across the membrane by the simple electrostatics equation $W = Q(V_i - V_o)$. If each ion S has a charge of z_S, then the equation can be written once more as

$$V_S \equiv V_i - V_o = \frac{RT}{z_S F} \ln \frac{[S]_o}{[S]_i} , \tag{2.19}$$

where F is Faraday's constant (9.648×10^4 C $\cdot$ mol^{-1}). The equilibrium potential V_S was first derived in the late nineteenth century by Walther Nernst of Göttingen, who consequently received the Nobel Prize [21].

A Nernst equilibrium potential exists for each type of ion. The overall membrane potential necessarily falls somewhere between the most negative and most positive of these individual ion equilibrium potentials, depending on how many of each type of ion channel are open. For most unexcited neurons, the membrane is much more permeable to K^+ than to any other type of ion. As a result, the overall resting potential is very close to the Nernst equilibrium potential of K^+.

2.3 The Cable Model

Although the resting potential is an important property of neurons, deviations from the resting potential are of much greater interest. *Excitation* occurs when the resting potential equilibrium is perturbed, usually by a signal from another cell or a current applied by an experimenter, and an ionic flux across the membrane occurs. For every neuron, there is a range of input amplitudes that will elicit a linearly proportional change in the membrane potential. Over this range, the waveform of the potential will mimic the waveform of the stimulus to a scaling factor. Linear responses to small perturbations may be called *sub-threshold* responses, as a stimulus that exceeds the range of linearity generally causes an action potential, which is highly non-linear.

The cable model combines the core conductor model with several additional assumptions regarding the electrical properties of the membrane to describe the voltage-current relations for small electrical perturbations. Experiments at the beginning of the twentieth century demonstrated that each section of the cell membrane can be well represented by a resistor-battery series parallel to a capacitor in the regime of linear voltage responses [22]. By replacing the nondescript empty box that represents the membrane in Fig. 2.4, with the new circuit element, we obtain the circuit diagram shown in Fig. 2.5. The battery, denoted by V_q, is the resting potential of the membrane. Per convention, the resistive element is described in terms of its conductance g_m per unit length, where conductance is defined as the inverse of resistance. The element c_m is the membrane capacitance per unit length.

The total potentials V and total currents K and I can be expressed as a sum of quiescent values V^0, K^0, I^0, which represent the values for a resting cell, and incremental values v, k, i, which express deviation from the quiescent values, so that $K_m(z,t) = K_m^0 + k_m(z,t)$, etc. With this modified notation, Eq. (2.14) can be rewritten

$$\frac{\partial^2[V_m^0(z) + v_m(z,t)]}{\partial z^2} = (r_o + r_i)[K_m^0(z) + k_m(z,t)] - r_o[K_e^0(z) + k_e(z,t)]. \qquad (2.20)$$

Noting that V_m^0 is constant in time and setting the incremental variables to zero yields

$$(r_i + r_o)K_m^0 - r_o K_e^0 = 0. \qquad (2.21)$$

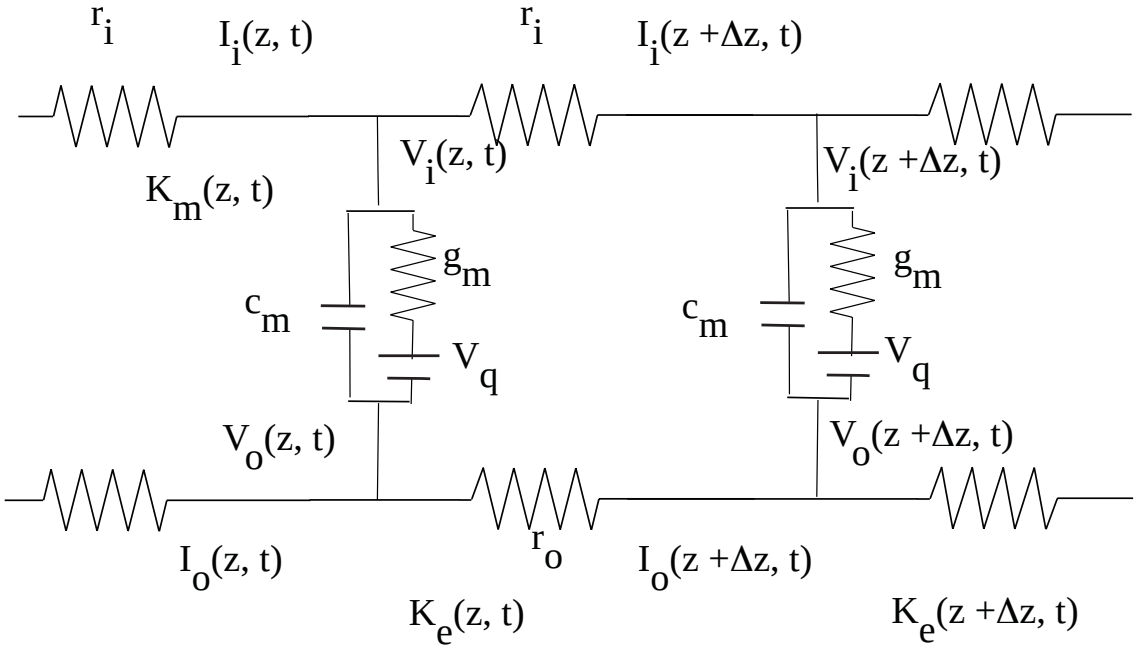

FIG. 2.5: Cable model representation of a small section of the cellular membrane for linear voltage-current relations. This circuit differs from the core conductor circuit in the representation of the membrane. V_q is the (quiescent) resting potential g_m denotes conductance per unit length, which is the inverse of resistance per unit length, and c_m is capacitance per unit length. Again, a factor of Δz is implied for all linear densities.

Subtracting Eq. (2.21) from Eq. (2.20) gives the familiar equation

$$\frac{\partial^2 v_m(z,t)}{\partial z^2} = (r_o + r_i)k_m(z,t) - r_o k_e(z,t). \tag{2.22}$$

Kirchhoff's current law allows us to express k_m as

$$k_m(z,t) = g_m v_m(z,t) + c_m \frac{\partial v_m(z,t)}{\partial t}. \tag{2.23}$$

Plugging Eq. (2.23) into Eq. (2.22) yields the *cable equation*, which was originally used to describe the transmission of electric signals along sub-oceanic cables:

$$\frac{\partial^2 v_m(z,t)}{\partial z^2} = (r_o + r_i)g_m v_m(z,t) + (r_o + r_i)\frac{\partial v_m(z,t)}{\partial t} - r_o k_e(z,t). \tag{2.24}$$

The cable model is useful in a large variety of contexts [18]. It was introduced here to serve primarily as a stepping stone to our short-term goal, derivation of the Hodgkin-Huxley model.

2.4 The Hodgkin-Huxley Model

The observation that ionic conductance changes during an action potential [23] sits at the heart of the Hodgkin-Huxley model. An experimental technique called voltage clamping, which uses an operational amplifier (op-amp) to directly control the membrane potential, allowed Hodgkin and Huxley to pinpoint Na^+ and K^+ as the ions that play the most significant role during action potential generation [24]. As a neuron becomes excited, it is depolarized slightly according to the cable model. At a specific membrane potential, the linear relationship between voltage and current breaks down, and the Na^+ channels are *activated*, meaning they open rapidly. Activation leads to increased ion conductance into the cell and rapid depolarization. When the potential reaches another specific potential, the slightly slower process of *inactivation* occurs, Na^+ channels begin to close, and depolarization slows, eventually leading to repolarization [6]. The K^+ channels, which conduct ions *out* of the cell, are also activated at a specific potential, although they do not undergo inactivation during an action potential. Rather, they close slowly after the potential returns to its rest value.

The term voltage gating describes the process of voltage regulated activation and inactivation. The molecular processes responsible for voltage gating remain an important topic for study in biophysics [6]. Fortunately, a complete understanding of these mechanisms is not necessary to develop the HH model or to make calculations of electrical responses to a given stimulus. Expressed as a circuit, the HH model does not differ

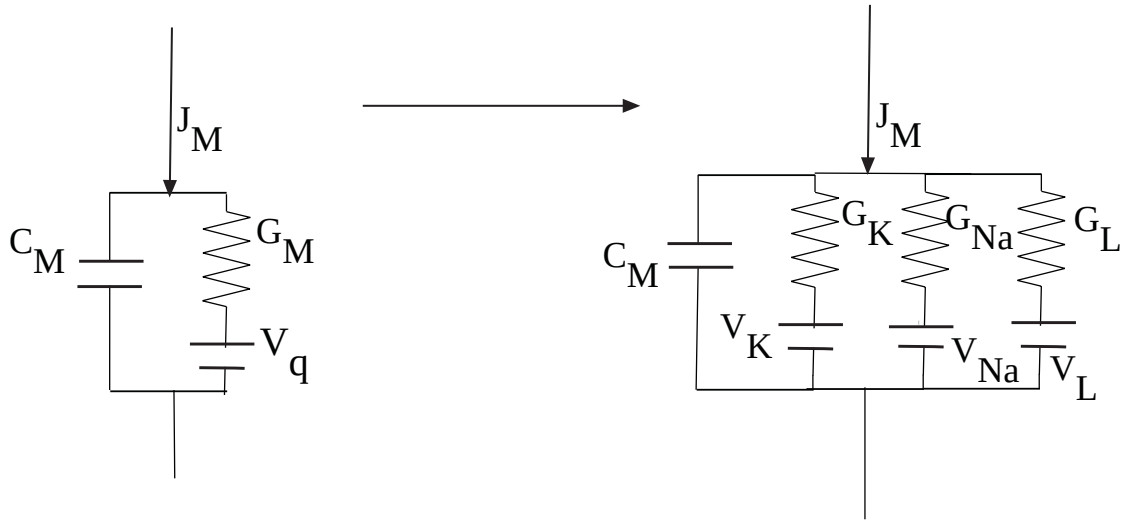

FIG. 2.6: Transformation of circuit element representing the membrane from the cable model to the HH model. The G_K and G_{Na} conductances are time and membrane potential dependent, while G_L is independent of both of these variables. The potentials are the equilibrium potentials of the subscripted ions.

greatly from the cable model, the important difference being the circuit element that represents the membrane, which is modified in the HH model to account for individual ion currents. Since membrane capacitance is unaffected during excitation [6], only the resistive element must be replaced. This transformation is shown in Fig. 2.6. The new resistive element consists of three parallel branches, each with a resistor and a source of electric potential. Each of the circuit elements in Fig. 2.6 now represents a small two-dimensional patch of membrane, so the current is now represented by J_m, an *area* density rather than a linear density. It is important to note that the conductance densities G_K and G_{Na}, which correspond to specific ionic conductances, are dependent on both time and the membrane potential. The associated potentials V_K and V_{Na} are the Nernst equilibrium potentials for Na^+ and K^+. The third branch carries the *leakage* current, which is independent of the membrane potential and accounts for all of the current not

associated with the primary excitable channels.

According to Kirchhoff's current law, the membrane current is the sum of the currents through each of the four branches:

$$J_m = J_C + J_K + J_{Na} + J_L, \tag{2.25}$$

or, multiplying both sides by the area element,

$$I_m = I_C + I_K + I_{Na} + I_L. \tag{2.26}$$

Rewriting each of the individual currents using Ohm's law for resistors and the constitutive law for the capacitor yields

$$I_m = c_m \frac{\partial V_m}{\partial t} + g_K(V_m, t)(V_m - V_K) + g_{Na}(V_m, t)(V_m - V_{Na}) + g_L(V_m - V_L). \tag{2.27}$$

In the absence of external stimulation,

$$I_m \to \frac{1}{r_o + r_i} \frac{\partial^2 V_m(z,t)}{\partial z^2}$$

per Eq. (2.14). In this case, Eq. (2.27) is a refinement of the core conductor model that takes into account the electrical properties of the membrane. On the other hand, if the conductances are taken to be constants, then the HH model (Eq. (2.27)) reduces to the cable model (Eq. (2.24)).

To find the membrane potential as a function of the membrane current, individual conductances, which depend on the membrane potential, must be known. By placing the squid giant axon in chemical baths prepared with specific ion deficiencies, Hodgkin and Huxley were able to measure the conductance for each type of ion individually over the course of an action potential [25]. Their findings prompted them to write the conductances as

$$g_K(V_m, t) = n^4(V_m)\bar{g}_K, \tag{2.28}$$

$$g_{Na}(V_m, t) = m^3(V_m)h(V_m)\bar{g}_{Na}, \tag{2.29}$$

where $\bar{g}_K$ and $\bar{g}_{Na}$ are the maximum conductances for the K^+ and Na^+ ions, respectively,

and n, m, and h are probabilities.

To obtain Eq. (2.28) Hodgkin and Huxley proposed the idea that the mechanism controlling each K channel can be represented by four independent membrane-bound "particles," each of which is in one of two possible states: the "permissive" state allows ion flow through the channel, and the "non-permissive" state prevents ions from flowing through the channel. A K^+ channel is open when all of the particles are permissive and closed if any of the particles is in the non-permissive state. The probability that any one of the particles is permissive is represented by n, which makes transitions with an exponential time course when the membrane potential is changed. The probability that all four particles are permissive is then n^4. This idea was motivated by fitting the g_K time course with an exponential curve, as almost nothing was known about the actual molecular structure of ion channels at the time.

Although the time course for g_{Na} is more complicated because the channels experience activation and inactivation, the logic is similar. In this case, three particles, each with probability m of being permissive, control activation, and one particle, with probability h of being permissive, controls inactivation. The probability that a channel is open is m^3h. Because Hodgkin and Huxley had little knowledge of the molecular mechanisms involved in opening channels their logic was rather abstract, though the results have proven to be extremely powerful.

Each probability n, m, and h is a function of both time and the membrane potential. If x_o and x_c represent the probabilities of an arbitrary particle being in the permissive state and non-permissive state respectively, then transitions between the permissive and non-permissive states can be described by the first order reaction

$$x_c \underset{\alpha_x}{\overset{\beta_x}{\rightleftharpoons}} x_o \ ,$$

with rate constants $\alpha_x(V_m)$ for the transition from non-permissive to permissive and $\beta_x(V_m)$ for the reverse transition. These rate constants can be found experimentally; they are generally equal for similar cells although they can vary significantly between cell types. The differential equations that describe these transitions for the probabilities

n, m, and h, which by definition cannot be greater than one, are:

$$\frac{dn}{dt} = \alpha_n(1-n) - \beta_n n, \tag{2.30}$$

$$\frac{dm}{dt} = \alpha_m(1-m) - \beta_m m, \tag{2.31}$$

$$\frac{dh}{dt} = \alpha_h(1-h) - \beta_h h. \tag{2.32}$$

For a fixed membrane potential, each probability reaches a limiting, or *steady-state* value at $t \to \infty$, which can be expressed:

$$n_\infty(V_m) = \frac{\alpha_n}{\alpha_n + \beta_n}, \tag{2.33}$$

$$m_\infty(V_m) = \frac{\alpha_m}{\alpha_m + \beta_m}, \tag{2.34}$$

$$h_\infty(V_m) = \frac{\alpha_h}{\alpha_h + \beta_h}. \tag{2.35}$$

The voltage-dependent *time constants* with which the probabilities approach this limit are given by:

$$\tau_n(V_m) = \frac{1}{\alpha_n + \beta_n}, \tag{2.36}$$

$$\tau_m(V_m) = \frac{1}{\alpha_m + \beta_m}, \tag{2.37}$$

$$\tau_h(V_m) = \frac{1}{\alpha_h + \beta_h}. \tag{2.38}$$

The steady-state values and time constants can be calculated from the rate constants, which are obtained by fitting experimental data. Hodgkin and Huxley originally fit the

rate constants of the squid giant axon [17] with the expressions

$$\begin{aligned}
\alpha_n &= \frac{0.01(V+55)}{1-e^{-0.1(V+55)}}, \\
\beta_n &= 0.125e^{-0.0125(V+65)}, \\
\alpha_m &= \frac{0.1(V+40)}{1-e^{-0.1(V+40)}}, \\
\beta_m &= 4e^{-0.0556(V+65)}, \\
\alpha_h &= 0.07e^{-0.05(V+65)}, \\
\beta_h &= \frac{1}{1+e^{-0.1(V+35)}}.
\end{aligned}$$

The numbers in these expressions vary widely from from cell to cell, as can be seen in the rate constants used for DS cells in Chapter 5, although the functional forms of each equation have become convention. The steady-state values and time constants that correspond to these expressions are shown in Fig 2.7.

Expressed in terms n, m, and h, Eq. (2.27) becomes,

$$I_m = c_m\frac{\partial V_m}{\partial t} + n^4\bar{g}_K(V_m - V_K) + m^3h\bar{g}_{Na}(V_m - V_{Na}) + g_L(V_m - V_L)\,. \qquad (2.39)$$

Eqs. (2.39), (2.30), (2.31), and (2.32) are know collectively as the Hodgkin-Huxley equations. This set of coupled differential equations is the culmination of the Hodgkin-Huxley model. If the membrane capacitance, equilibrium potentials, maximum conductances, and rate constants are known for a given cell type, the HH equations can be solved numerically for V_m with a given I_m. That is, the HH equations can be used to predict action potentials for a given stimulus. Because several approximations were made to construct this model, and the actual response is somewhat stochastic, this prediction is not exact. In the appropriate context, however, the HH model is an extremely useful tool.

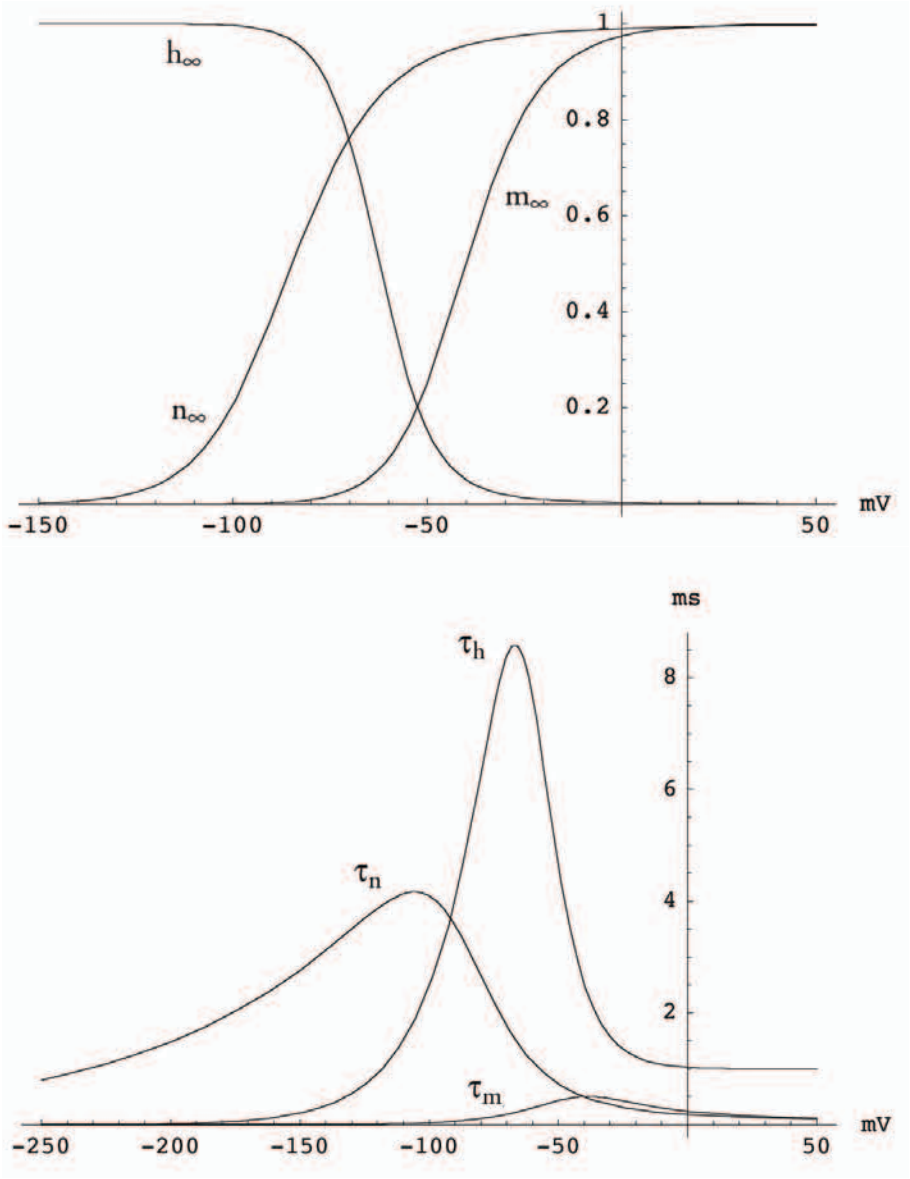

FIG. 2.7: Steady-state values (*top*) and time constants (*bottom*) for the squid giant axon. As probabilities, the steady-state values are unitless, and all variables are independent of time. The steady-state value is the permissive probability limit for a given voltage. The time constant graphs show how long it takes to reach the steady state value for a given membrane potential.

The derivation of the HH equations serves a dual purpose in this thesis. On one hand, it constitutes a basic theory of electrically excitable membranes, which is necessary to explain the origin of the data discussed in Chapter 5. Additionally, a modified version of the HH model will be used to model the response of a DS cell during the data analysis.

Chapter 3

Neural Encoding

The Hodgkin-Huxley model considers the problem of how a cell responds to an electrical stimulus. In this chapter, we will address a related problem using a completely different approach. The goal is to understand how information about a stimulus is encoded in the output signal of a neuron. In general, this output signal consists of a series of action potentials commonly called a *spike train*. Spike trains are the primary method of communication between neurons. In 1948 Max Born noted,

> The messages which the brain receives have not the least similarity with the stimuli. They consist in pulses of given intensities and frequencies, characteristic for the transmitting nerve-fiber, which ends at a definite place of the cortex. All the brain 'learns' ... is a distribution or 'map' of pulses. [26]

Apparently, the nervous system must have a method for encoding and processing sensory information.

Because action potentials are abrupt changes in membrane potential, they can be detected by measuring the current just outside of a neuron's soma or axon. An example of a recorded spike train is shown in Fig. 3.1[1]. The individual spikes last for only a few milliseconds, with most of the structure being confined to an even smaller window of time. It is useful to treat the spikes as instantaneous events that can be characterized completely by the time at which they occur. In this case, a spike train containing n

[1] Note that the horizontal axis for each graph labeled with an 's' in this thesis is assumed to represent time (units of seconds) unless explicitly noted otherwise. Similarly, each vertical axis labeled 'nA' should be taken to represent current (units of nano-Amps).

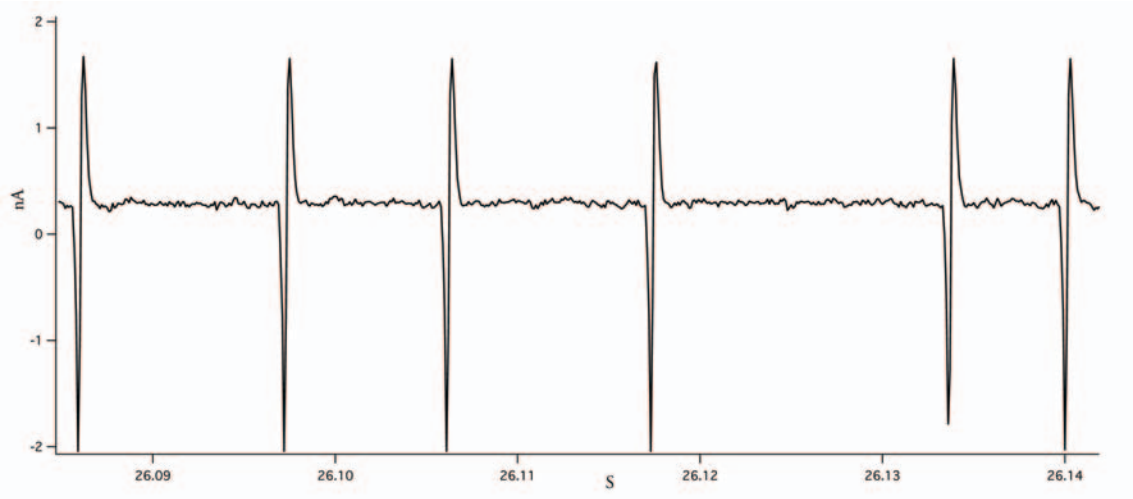

FIG. 3.1: Sample spike train segment. This recording was made outside of the soma of a DS ganglion cell. Note individual spike are only a few milliseconds long. Consequently, they can easily be transformed into delta functions.

spikes can be represented as a sequence of times at which each spike occurs t_i where $i = 1, 2, ..., n$ on the interval $0 \leqslant t_i \leqslant T$.

3.1 The Neural Response Function

The *neural response function* $r(t)$ is a sum of Dirac delta functions (δ) located at points defined by the spike times:

$$r(t) \equiv \sum_{i=1}^{n} \delta(t - t_i). \tag{3.1}$$

According to the definition of the Dirac delta function [2],

$$\int_0^T r(\tau)d\tau = n. \tag{3.2}$$

If the *spike-count rate* is defined $r \equiv n/T$, then

$$r = \frac{1}{T}\int_0^T r(\tau)d\tau. \tag{3.3}$$

[2]Note that the letter τ here is not related to the time-constants discussed in the previous chapter

At this point, most of the literature proceeds to define the time dependent firing rate in terms of the trial-averaged neural response function, which requires multiple presentations of the same stimulus [27, 28]. Since each data set analyzed in this thesis was generated using a unique stimulus, it is necessary to follow a different, though analogous, route. Unless otherwise specified, the firing rate will be equivalent to the neural response function. When it is necessary to define a firing rate that is different from the response function, $r(t)$ is usually reserved for the firing rate and $\rho(t)$ is used for the response function.

3.2 The Spike-Triggered Average

Ideally, a neuron will respond primarily to a single physical feature of a presented stimulus. The significant feature can be expressed as a time dependent variable $s(t)$, and the other attributes of the stimulus can be ignored. For each spike time t_i there is a corresponding section of the stimulus, $s(t_i - \tau)$, which begins a certain time before the spike occurs. The *spike-triggered average* (STA), written $C(\tau)$, is the average of each of these stimulus segments:

$$C(\tau) = \frac{1}{n} \sum_{i=1}^{n} s(t_i - \tau). \tag{3.4}$$

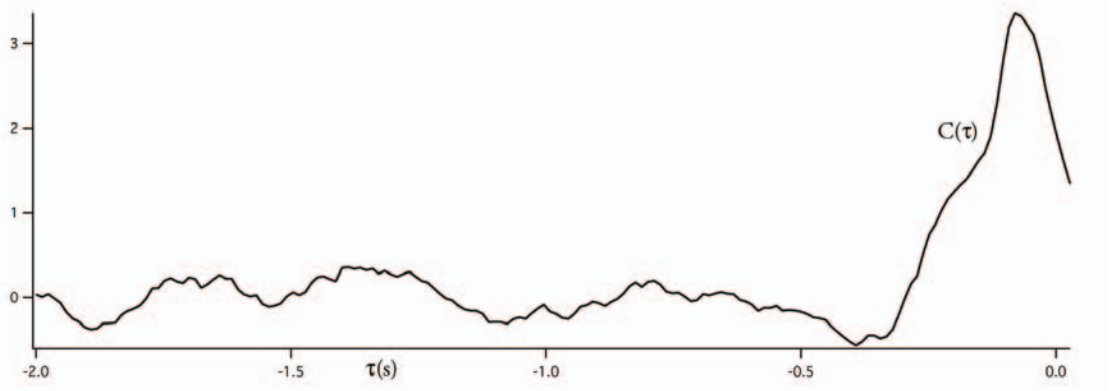

FIG. 3.2: Sample spike-triggered average over the interval $-2 < \tau < 0$. The spike-triggered average $C(\tau)$ corresponds to an arbitrary s(t) and does not have specific units. Note that all of the structure occurs between -0.5 and 0. The rest of the displayed segment of the STA is approximately zero, discounting noise.

The sample STA in Fig. 3.2 reveals several significant features of a cell's response to the specific stimulus used to generate the spike train. This STA is not generalizable to all stimuli, however, because the temporal autocorrelation (Fig. 3.3) of a specific stimulus will bias the STA. The autocorrelation of the stimulus is defined

$$Q_{ss}(\tau) \equiv s(t) \star s(t) = \frac{1}{T}\int_0^T s(t)s(t+\tau)dt. \tag{3.5}$$

where $\star$ denotes correlation. Q_{ss} describes how the value of the function at a given time depends on the value of the function at previous times and how it will effect the value of the function at future times. The influence of the stimulus autocorrelation can be seen in Fig. 3.2, when $C(\tau)$ fails to vanish for the acausal interval $\tau \geqslant 0$. The STA represents the average stimulus that elicits a spike. Obviously, the cell cannot spike in response to concurrent or future actions of a stimulus. In order to create a function which describes a cell's response to a *general* stimulus, it is necessary to remove the stimulus autocorrelations from the STA.

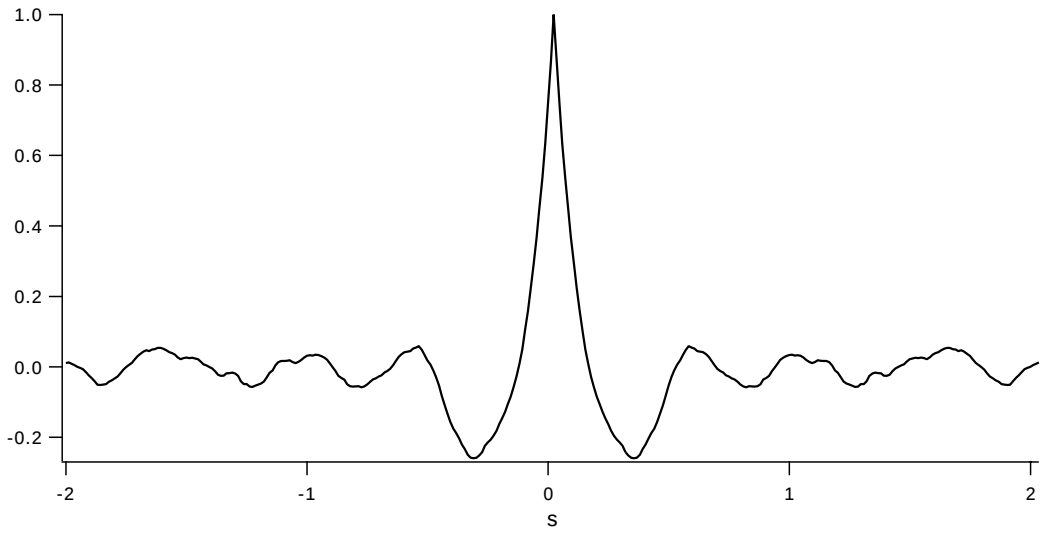

FIG. 3.3: Sample stimulus autocorrelation. The stimulus is strongly correlated with itself near $\tau = 0$ and shows slight periodicity over the interval $-2 \leqslant \tau \leqslant 2$. We would expect to see similar features in the STA for this stimulus.

3.3 Reverse Correlation Function

The STA can also be expressed in the form of an integral by utilizing the conveniently defined neural response function. According to Eqs. (3.1) and (3.4), we can write

$$C(\tau) = \frac{1}{n}\int_0^T r(t)s(t-\tau)dt. \tag{3.6}$$

The integral form of $C(\tau)$ is particularly useful if we note that the cross-correlation of $r(t)$ and $s(t)$, which are both real functions, is defined as

$$Q_{rs}(\tau) \equiv r(t) \star s(t) = \frac{1}{T}\int_0^T r(t)s(t+\tau)dt. \tag{3.7}$$

The relationship given by combining Eqs. (3.6) and (3.7) is

$$C(\tau) = \frac{n}{T}Q_{rs}(-\tau) \tag{3.8}$$

Apparently the STA can also be obtained by scaling and reflecting Q_{rs} about the vertical axis; therefore $C(\tau)$ is frequently referred to as the *reverse correlation function*. The relationship shown in Eq. (3.8) is particularly important to removing the stimulus autocorrelation influence from the STA.

3.4 The Wiener Kernel

The response function $r(t)$ depends on the time-dependent function $s(t)$ and could therefore be written as a functional $r(s(t))$. Thus, the response function can be expressed as a Volterra expansion, which is the functional analog to Taylor expansion [29]. The Volterra expansion of $r(s(t))$ describes its relationship to $s(t)$ in terms of a set of kernels $D_n(\tau)$:

$$r(t) \approx r_0 + \int D_1(\tau)s(t-\tau)d\tau + \int D_2(\tau_1,\tau_2)s(t-\tau_1)s(t-\tau_2)d\tau_1 d\tau_2 + ... \tag{3.9}$$

The zeroth order term r_0 corresponds to random background firing, and can be ignored because it is insignificant compared to stimulus invoked spiking. Additionally, higher order terms can generally be disregarded unless it is apparent that the stimulus-response

relationship is non-linear. Consequently, an estimate of the response requires only one kernel, $D = D_1$:

$$r_{est}(t) = \int D(\tau)s(t-\tau)d\tau. \tag{3.10}$$

$D(\tau)$ is called the first order *Wiener kernel*, or simply the Wiener kernel, after Norbert Wiener, whose modifications of the Volterra expansion made it easier to use. According to Eq. (3.10), the relationship between $r(t)$ and $s(t)$ can be estimated using only the function D. If this kernel can be calculated, then it is possible to reproduce or predict the response to a given stimulus, as shown in Chapter 5.

The Wiener kernel can be found by minimizing the squared difference between the actual response and the estimated response. If a function E is defined

$$\begin{aligned} E(D) &\equiv \frac{1}{T}\int_0^T (r_{est}(t) - r(t))^2 dt \\ &= \frac{1}{T}\int_0^T \left(\int_0^\infty D(\tau)s(t-\tau)d\tau - r(t) \right)^2 dt, \end{aligned} \tag{3.11}$$

then the appropriate choice for D satisfies the condition $\partial E/\partial D = 0$, or equivalently $E(D+\delta D) = E(D)$ for small δD. Letting $D \to D + \delta D$ gives

$$E(D+\delta D) = \frac{1}{T}\int_0^T \left(\int_0^\infty \big(D(\tau) + \delta D(\tau)\big)s(t-\tau)d\tau - r(t) \right)^2 dt. \tag{3.12}$$

Squaring the t integrand yields:

$$\begin{aligned} E(D+\delta D) = E(D) + \frac{1}{T}\int_0^T \Bigg[\int_0^\infty \int_0^\infty \Big(& 2D(\tau')\delta D(\tau)s(t-\tau)s(t-\tau') \\ & + \delta D(\tau)\delta D(\tau')s(t-\tau)s(t-\tau') \Big) d\tau d\tau' \\ & - 2\int_0^\infty \delta D(\tau)s(t-\tau)d\tau\, r(t) \Bigg] dt. \end{aligned} \tag{3.13}$$

Since, δD is small, the $\delta D(\tau)\delta D(\tau')$ term is negligible compared to the other terms and falls out of Eq. (3.13), leaving

$$\begin{aligned} E(D+\delta D) - E(D) = \frac{1}{T}\int_0^T \Bigg[\int_0^\infty \int_0^\infty & \Big(2D(\tau')\delta D(\tau)s(t-\tau)s(t-\tau') \Big) d\tau d\tau' \\ & - 2\int_0^\infty \delta D(\tau)s(t-\tau')d\tau\, r(t) \Bigg] dt = 0. \end{aligned} \tag{3.14}$$

Rearranging the terms and simplifying gives

$$\int_0^\infty D(\tau') \int_0^T s(t-\tau)s(t-\tau')dtd\tau' - \int_0^T r(t)s(t-\tau)dt = 0. \tag{3.15}$$

Using the definitions of Q_{rs} (see Eq. (3.7)) and Q_{ss} (see Eq. (3.5)), this equation can be written

$$\int_{-\infty}^\infty D(\tau')Q_{ss}(\tau-\tau')d\tau' = D(\tau) * Q_{ss}(\tau) = Q_{rs}(-\tau) \tag{3.16}$$

where $*$ denotes convolution (remember $\star$ is used for correlation).

The convolution theorem states that the Fourier transform of a convolution is the product of the Fourier transforms of the two functions being convolved. Implementing this theorem and taking the Fourier transform of both sides yields

$$\hat{D}(\omega)\hat{Q}_{ss}(\omega) = \hat{Q}_{rs}(-\omega). \tag{3.17}$$

where $\hat{}$ denotes the Fourier transform of the function beneath it. Solving for $\hat{D}$, we have

$$\hat{D}(\omega) = \frac{\hat{Q}_{rs}(-\omega)}{\hat{Q}_{ss}(\omega)}. \tag{3.18}$$

Taking the inverse Fourier transform of both sides yields a final expression for D in terms of the response function and the stimulus function:

$$D(\tau) = \frac{1}{2\pi}\int_{-\infty}^\infty \frac{\hat{Q}_{rs}(-\omega)}{\hat{Q}_{ss}(\omega)} e^{-i\omega\tau}d\omega. \tag{3.19}$$

The Wiener kernel, D, predicts (to first order) how strongly and with what sign an arbitrary stimulus at time $t-\tau$ will affect the neural response at time t. With the right tools, the kernel can be calculated if both the stimulus and the response function are known. In most experiments, including the one described in this thesis, the stimulus is defined and parameterized beforehand, and the spike train response is recorded with an electrode.

3.5 Continuous Neural Responses

Some of the neural responses discussed in this document do not take the form of a spike train. Rather, they are continuous intracellular current recordings, as shown in Fig. 3.4. The benefit of the intracellular recording is that, assuming a high sampling rate, it contains many more non-trivial sample points per second than does a spike train. Using this alternate method would ideally improve the signal-to-noise ratio. Since there are no spikes, however, it is necessary to adapt our definition of the neural response function $r(t)$ for these data sets.

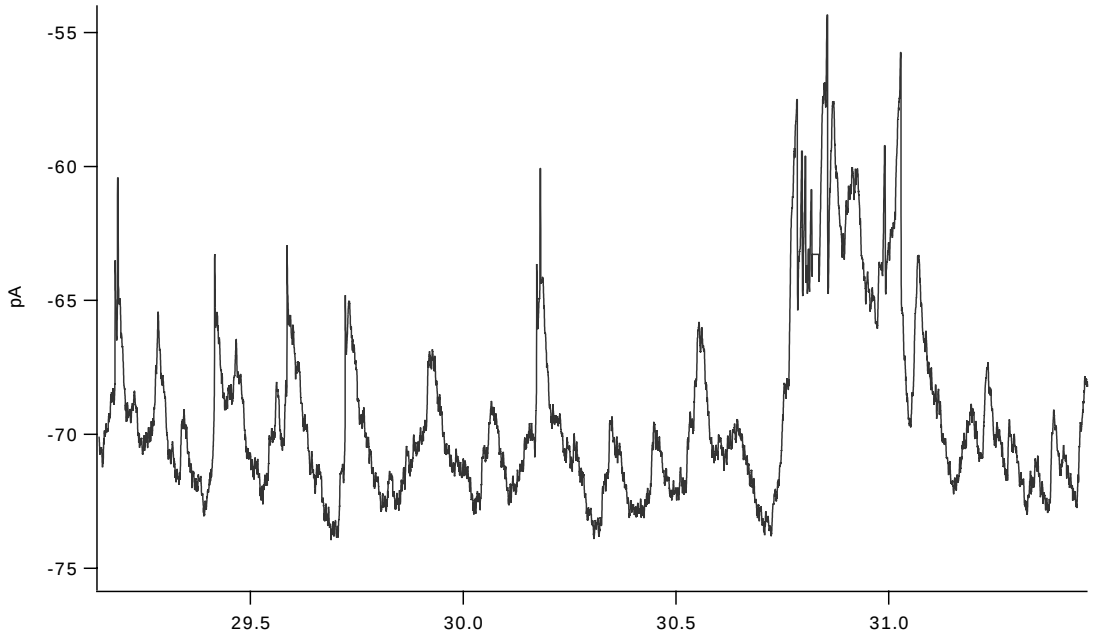

FIG. 3.4: Sample recording of the intracellular current. The spikes have been removed using a computer so that the response may be regarded as a continuous function. This record contains many more sample points per second than a spike train.

For the sake of simplicity, the intracellular neural response function r_i will be defined

$$r_i(t) \equiv \gamma(I_i(t) - I_0), \tag{3.20}$$

where $I_i(t)$ is the intracellular current, I_0 is the average intracellular current (excluding spikes), and γ normalizes the function by setting the maximum response at 1. Con-

veniently, this definition allows us to maintain our previous notation. Just as a burst of spikes indicates a strong response to a stimulus, an elevated intracellular current indicates strong excitation. Although $C(\tau)$ can no longer accurately be called the spike-triggered average, this quantity still describes how strongly a cell responds to specific stimulus. Similarly, the Wiener kernel still estimates the strength of correlation between a general stimulus and the newly defined response function.

Chapter 4

Recording from Direction Selective Cells

The traditional stimulus for exploring the properties of neural encoding in DS ganglion cells consists of a computer monitor divided into a grid [12], and focused onto the receptive field of a DS cell. At every refresh of the monitor, each section of the grid flashes either grey, dark, or bright. Occasionally the cell will detect motion from one point of the grid to another and generate spikes. Although the flashing-grid stimulus has the benefit of being white and does not impose any predefined notion of movement, there are several inherent problems. The signal-to-noise ratio (SNR) is rather low, and the data is difficult to interpret even when it is clean. An initial goal of this research was to develop an alternative stimulus that could be more easily analyzed.

4.1 The Edge

Knowing that the cells of interest were motion sensitive allowed us to design a stimulus that could exploit this fact to yield a high SNR. The essence of the stimulus is an edge that divides a dark portion of a computer screen from a bright portion. The screen is divided into 202 pixels along the axis of the DS cell's preferred direction and has an update frequency of 85 Hz. An edge speed of 1 pixel/frame on the monitor corresponds to a speed of 144 μm/s on the retina. A positive velocity corresponds to motion in the preferred direction. A random number generator is used to manipulate the edge in two distinct ways. At each screen update, the velocity of the edge is randomly incremented in steps of either -1, 0, or +1 pixels/frame, though it is not allowed to exceed the user specified speed limit or to leave the screen entirely. It is then randomly multiplied by a

factor of -1 or +1. The next refresh of the monitor reflects this change and moves the edge accordingly. The frequency with which each of these adjustments occurs can be altered individually. The net effect is a bounded random walk in velocity with random direction flipping. When the stimulus is started, the edge begins in the middle of the screen. It begins to move when the first non-zero velocity adjustment is generated and proceeds to move back and forth across the screen with random velocities within a defined range until it is terminated by the experimenter.

The stimulus was originally programmed in *C* for driving the video stimulus and then recreated for the purposes of data analysis in the data processing program *Igor*[1]. The code used to reproduce the velocity of the stimulus can be found in the *Igor* code in Appendix A.

The edge stimulus provides two major benefits over the flashing-grid stimulus. Although the edge occasionally has zero velocity, it spends most of its time moving in either the preferred direction or the opposite direction. Consequently, the neuron constantly experiences either excitation or inhibition. The number of spikes produced by the stimulus far outweighs the number due to stochastic spiking so the SNR is high compared to that of the flashing-grid stimulus, and less data is required to obtain a well-defined spike-triggered average. The ease with which the stimulus can be described mathematically constitutes another clear advantage. Parameterization of the flashing-grid stimulus proves to be a cumbersome task because each cell of the grid must be described by its own time-dependent function. The relationships between these functions are generally complex and difficult to untangle. In contrast, the edge stimulus can be fully described in terms of a single time-dependent function, usually position or velocity. A graph of the velocity of the edge as a function of time is shown in Fig. 4.1. Analyzing the relationship between the neural response and the stimulus is comparatively straight forward.

Despite the convenience it affords, the edge stimulus is not without its disadvantages. Specifically, there is necessarily strong temporal autocorrelation in a random walk. Because the edge moves continuously, the position of the edge at a time t is equal to the the position before the last refresh plus the value of the velocity at $t - 1$. The velocity at any time is also strongly correlated to the velocity at the previous instant, though the randomly occurring factor of -1 makes this correlation periodically negative. The rela-

[1] *Igor Pro* Version 4.08, Wavemetrics, Lake Oswego, OR.

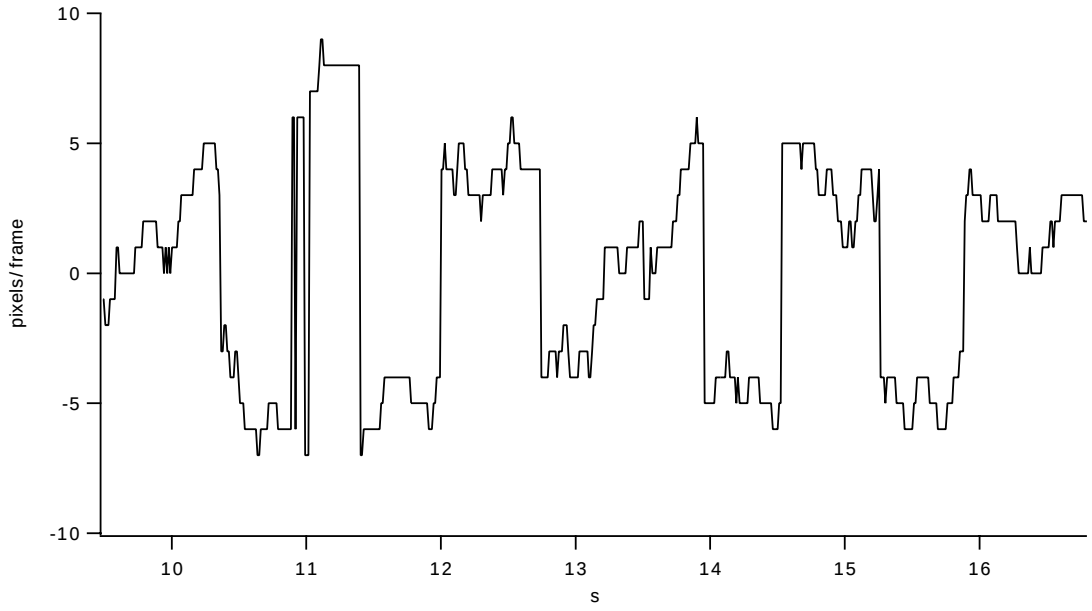

FIG. 4.1: Graph of edge velocity as a function of time. Unlike a flashing-grid stimulus, the edge is easily parameterized and graphically represented.

tionship of the stimulus autocorrelation to the spike-triggered average will be analyzed more rigorously in Chapter 5.

4.2 Extracellular Recording

All data was collected in the lab of Rowland Taylor at the Neurological Sciences Institute, a research division of Oregon Health and Science University. I was present in the lab during the trials and participated by designing and controlling the stimulus.

The edge stimulus was presented to the receptive fields of DS cells in a live piece of rabbit retinal tissue. A slice of the retina was removed from a rabbit and placed in a small compartment filled with oxygenated Ames solution, a substance that is rich in the ions and other chemicals upon which living tissue is dependent, at 35° C. The tissue is able to survive in this medium for several hours after dissection. If the photoreceptors are not exposed to bright light, the retina continues to function as though it were in a living organism.

A light microscope (40x magnification) was used to view individual cells within the tissue on a video monitor. To avoid damaging photoreceptors by overexposure to visible

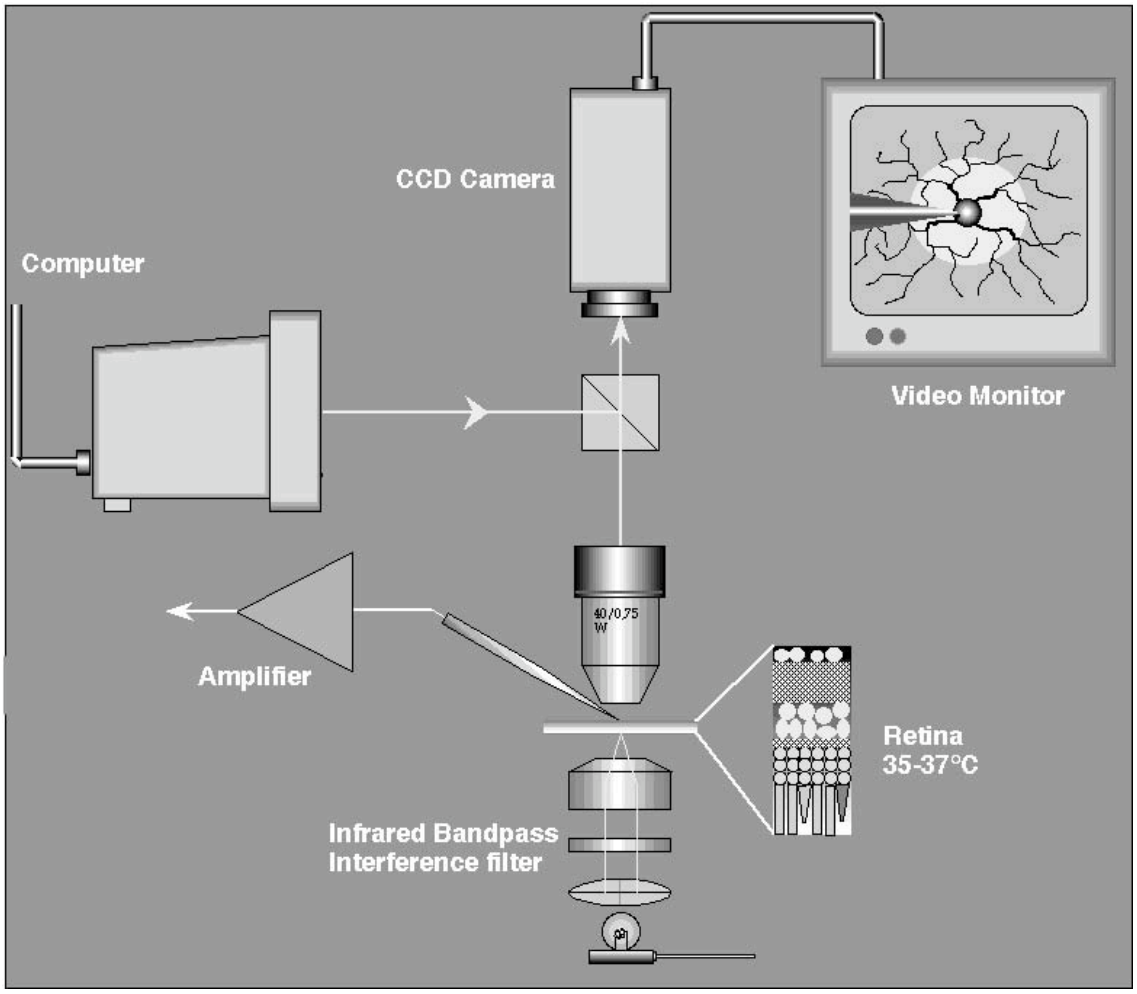

FIG. 4.2: Illustration of experimental setup. A beam splitter is used to view the cell and electrode through a light microscope (40x magnification) while the stimulus is being presented. Infra-red light is used to avoid overexposing the photoreceptors. The CCD is necessarily chosen to be particularly sensitive. Graphic adapted from `http://jcsmr.anu.edu.au/~dns/rowland/Set-up.html`, 2004.

light, infra-red light (~ 900 nm) was passed through the tissue into the objective. A charge-coupled device (CCD) camera capable of detecting this light was used to capture the image and present it on the video monitor. Because the retina is transparent, the CCD could be focused on the ganglion cell layer without obstruction by other cells. When a suspected DS ganglion cell was located on the monitor, an electrode was positioned against, but not penetrating, the membrane of the neuron's soma, which carries the same signal as the axon and is considerably easier to locate.

As shown in Fig. 4.2, a beam splitter was used to focus the stimulus onto the area of the retina that is displayed on the monitor. When a ganglion cell was found, a test stimulus was presented to check for direction selectivity. The test stimulus consists of a bright bar that moves from one side of the computer screen to the other, changing directions by 30° after each trip across the screen. The moving bar generates two spike bursts when it is near the preferred direction of an On-Off DS cell: the first burst occurs when the bar enters the receptive field and excites the On channel, and the second occurs when the bar leaves the receptive field and excites the Off channel. The spikes that occur for each orientation of the bar are counted, and the preferred direction is defined as that which resulted in the most spikes. If the preferred direction obviously falls between two of these directions, the test stimulus is presented again with direction changes of 15°.

After a DS cell was found and the preferred direction was determined, the edge stimulus was aligned with the appropriate axis and presented to the cell in runs that generally lasted 40-55 seconds. During this period, the cell's spikes were recorded using a commercial oscilloscope emulation software made by *HEKA*, which sampled at 10,000 Hz. The time for each trial was limited by the memory of the computer running the oscilloscope.

The membrane current splits into a current that flows parallel to the membrane and a current drawn by external electrodes, as demonstrated by the core conductor model in Chapter 2. An electrode with an extremely low resistance is used in order to draw all of the membrane current. The electrode is located in a glass pipette with a microscopic fire-polished opening at the end. An action potential results in a sharp biphasic spike in the recorded current similar to those shown in Fig. 3.1. The computer that presents the stimulus is synchronized with the computer that records the spike train to a precision of 0.1 ms.

4.3 Patch-clamp Recording

In addition to extracellular recording, intracellular currents were recorded and subjected to similar analyses. The process of obtaining intracellular current recordings is notably more complicated than that of obtaining spike trains [30]. In this case, the pipette containing the electrode is filled with a solution that is chemically similar to the cytoplasm positioned against the soma, just as it was for extracellular recordings. Unlike extracellular recording, however, a slight suction is applied to the large end of the pipette, causing the glass to form a high resistance seal with the cell membrane. This seal is generally on the order of 10-100 GΩ [18] so that current does not leak out at the pipette/membrane boundary.

Once the seal is formed, another slight suction is administered, and the membrane inside the pipette is ripped from the rest of the cell. The pipette becomes continuous with the cell membrane, and the fluid within the pipette becomes continuous with the cytoplasm. An illustration of this procedure is shown in Fig. 4.3. The record obtained with this recording configuration is distinctly different from an extracellular spike train. The sample section of an intracellular recording in Fig. 4.4 reveals subthreshold membrane responses. Also, individual spikes no longer appear as biphasic bursts of current, since the electrode is effectively recording from within the cell.

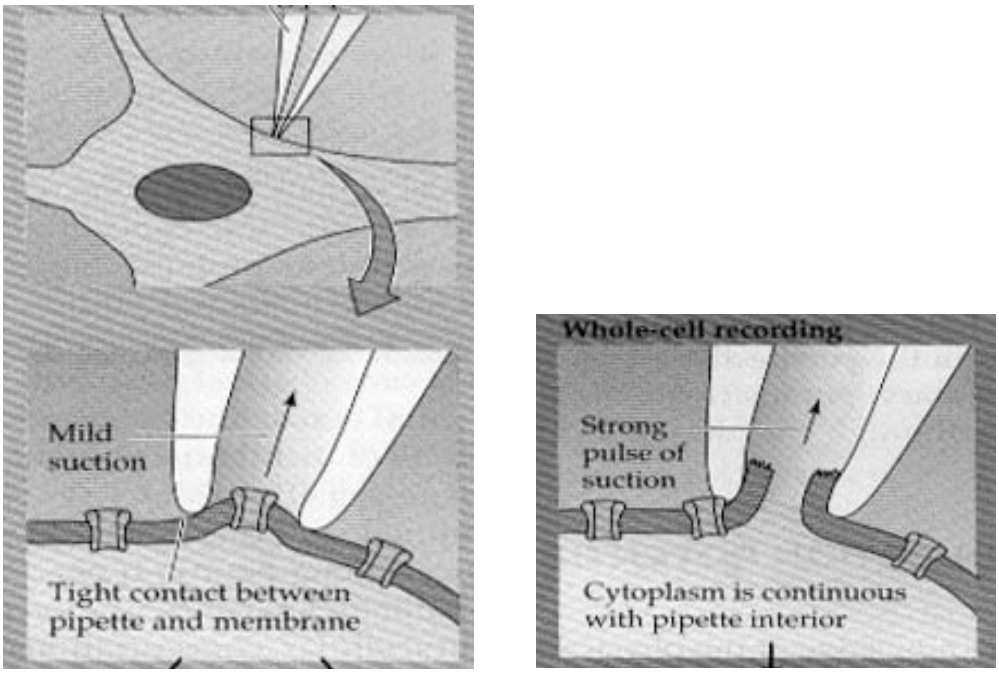

FIG. 4.3: Schematic for whole-cell patch recording. [Adapted from `http://www.life.nthu.edu.tw`, 2004.]

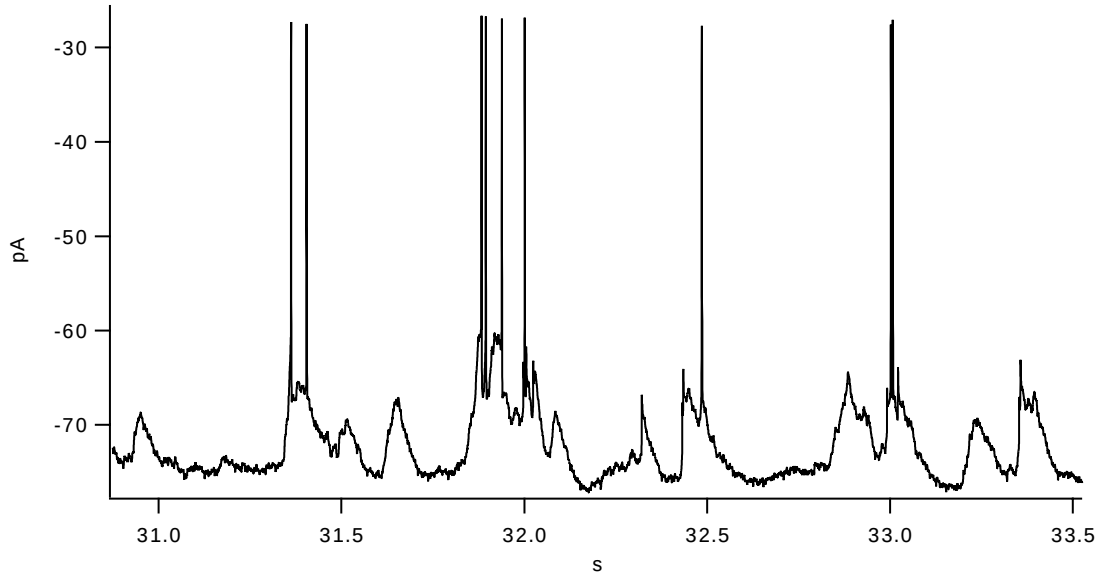

FIG. 4.4: Sample recording of intracellular current. Note that the spikes are not biphasic, as they were for extracellular recordings (see Fig. 3.1).

Chapter 5

Data and Analysis

Extracellular and intracellular records were imported into *Igor* from the oscilloscope emulator. Each record is identified by a number that corresponds to the trial from which it was produced. All analysis and manipulations of the recordings were performed with original code found in Appendix A unless otherwise noted.

Results of the spike train analysis encourage an attempt to model the neural response by solving the Hodgkin-Huxley equations in *Mathematica*[1]. Appendix B is comprised of the *Mathematica* notebook, which contains the commands and sample graphs relevant to this portion of the experiment.

5.1 Finding Spikes

Recording such small intracellular and extracellular signals from neurons requires delicate equipment that is prone to detecting noise from ambient sources. The amplitude of the noise frequently has a magnitude near that of the spikes, as shown in Fig. 5.1. Obviously, a clean spike train is necessary to develop a relationship between the neural response and the stimulus. A two-step filtering method was developed to remove the noise from the data. First, two thresholds are set based on the appearance of the spike train. An upper threshold and a lower threshold are selected above and below the baseline noise. For recording 1-57 shown in Fig. 5.1, the baseline (average) current is approximately -0.5 nA, and the upper and lower thresholds were selected at -0.2 nA and -1.0 nA, respectively.

[1] *Mathematica* version 4.2, Wolfram Research, Inc., Champaign, IL.

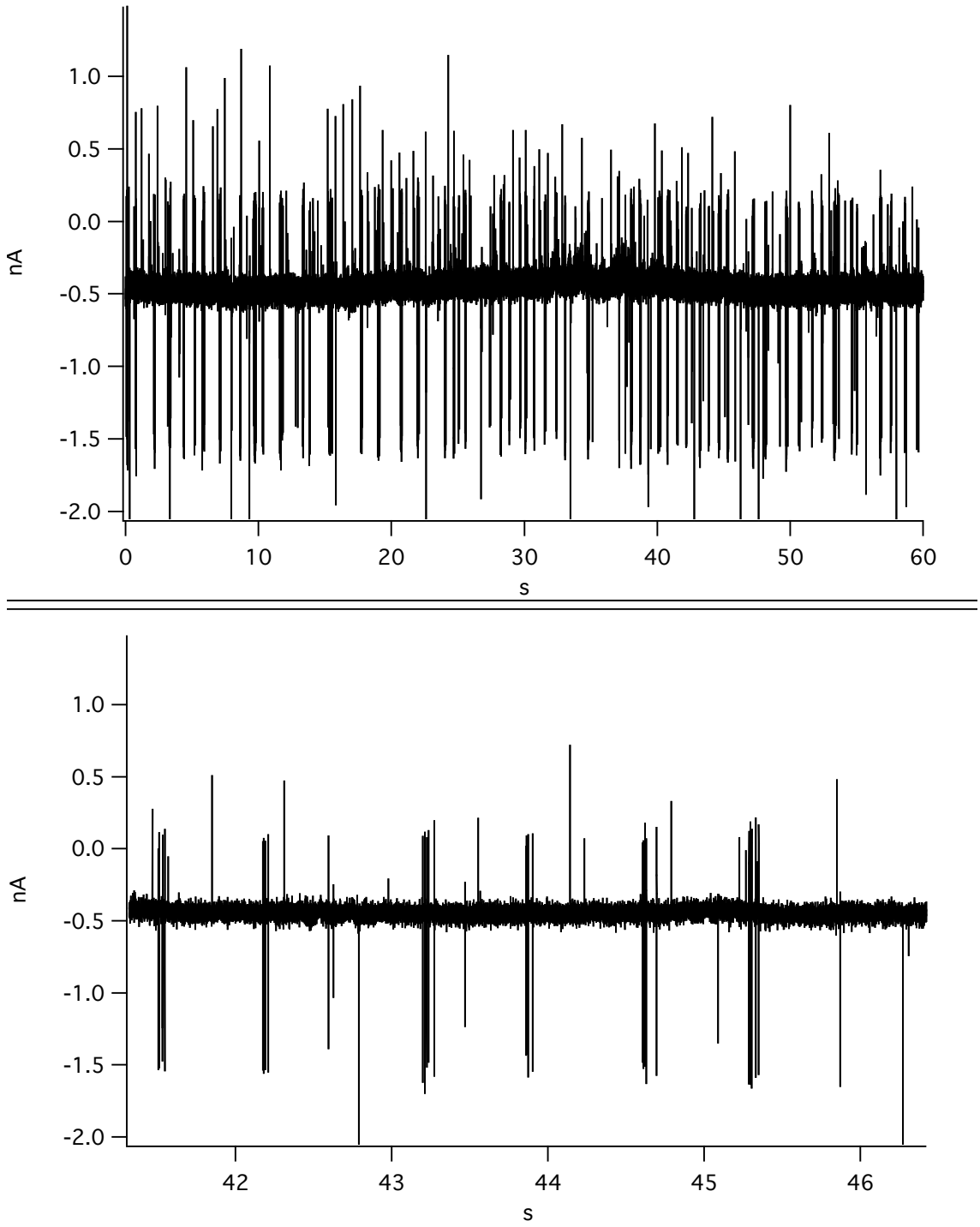

FIG. 5.1: Spike train 1-57. **Top:** The extracellular current record for the edge stimulus is cluttered with noise. **Bottom:** An expanded segment of the spike train shows that some of the noise, identifiable as the spike-like structures that do not occur in bursts, is of the same amplitude as the spikes. Noise occasionally produces a biphasic spike-like structure.

Any 3 ms section of the recording that exceeds both the upper and lower threshold is preserved; the remainder of the recording is set equal to the average current for the entire trial. Spike train 1-57 is shown after the first step of filtering in Fig. 5.2. Apparently, this step successfully removes most of the noise, including noise with amplitude comparable to that of the spikes. Occasionally the noise mimics the spikes in amplitude and shape as seen in Fig. 5.3, or a legitimate spike fails to surpass one of the thresholds. The second step of the filtering process is an attempt to correct both of these problems.

The 3 ms window around each maximum in the filtered record is averaged together to produce a spike "template." The template is compared to the original recording at each point of the spike train, by summing the squared difference of the spike train and the record, to produce a new function that relates the shape of each spike-like structure to the average spike shape. A lower threshold is defined, and at points where the new function exceeds this threshold the corresponding time becomes an element in a list of spike times. A segment of the spike-matching function for spike train 1-57 is shown in Fig. 5.5; an appropriate threshold for this function would be 1.

5.2 Acausal Elements of the Spike-Triggered Average

The filtering process converts an extracellular recording to a list of spike times. The spike-triggered average (STA) is obtained by summing sections of the spike stimulus per Eq. (3.4). The STA for a single 60 second trial is generally quite noisy, as shown in Fig. 5.6. Averaging together the STAs of several trials on the same cell effectively extends the trial period and reduces the noise significantly. The average STA for spike trains 1-57, 1-58, 1-73, 1-75, 1-77 and 1-81 is displayed in Fig. 5.7. The corresponding spike trains and stimuli can be found in Appendix C.

The peak of the STA at 5 pixels/frame despite an average stimulus velocity of 0 demonstrates the neuron's preference for motion in the positive (preferred) direction. Unfortunately, additional information about the neuron is obscured by the effects of the temporal autocorrelation (AC) of the stimulus shown in Fig. 5.8, which produces minima of a similar structure.

The STA seems to suggest that the cell responds optimally to periodic variations in velocity in the recent history as well as the near future. It is likely, however, that both of

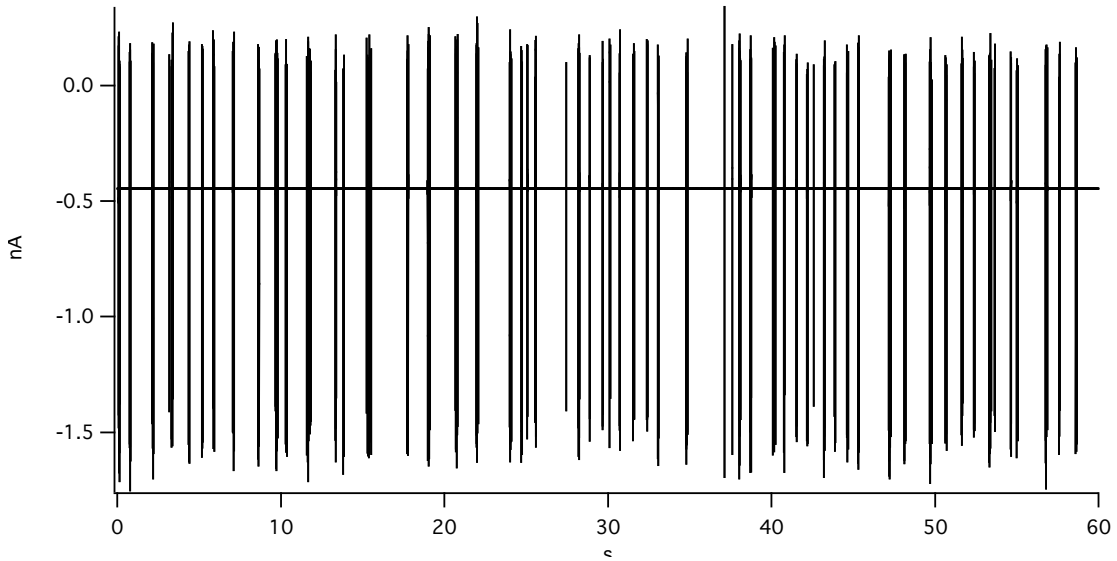

FIG. 5.2: Partially filtered version of spike train 1-57. The first filtering step, which relies on an upper and lower threshold, removes the baseline noise and most of the noise with high amplitude as well. Unfortunately, some of the spikes are also lost.

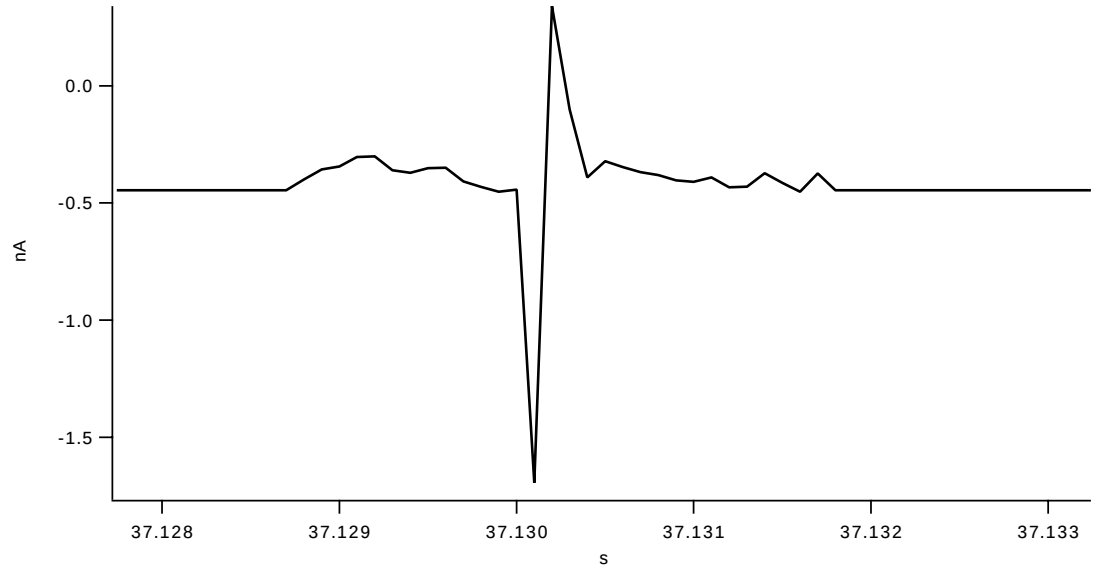

FIG. 5.3: Spike-like noise which was not removed after first filtering step. Although this "false" spike surpasses both thresholds, it does not have the characteristic spike shape defined by the template in Fig. 5.4. Features of the recording such as this are removed by the template matching step.

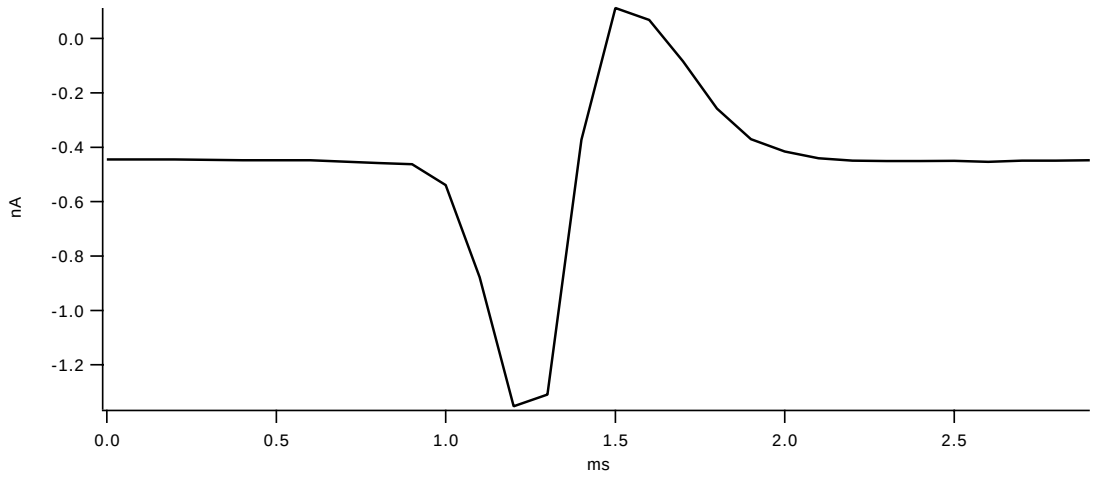

FIG. 5.4: Average spike shape from filtered spike train 1-57. When convolved with the original record, the average spike serves as a template for picking out spikes.

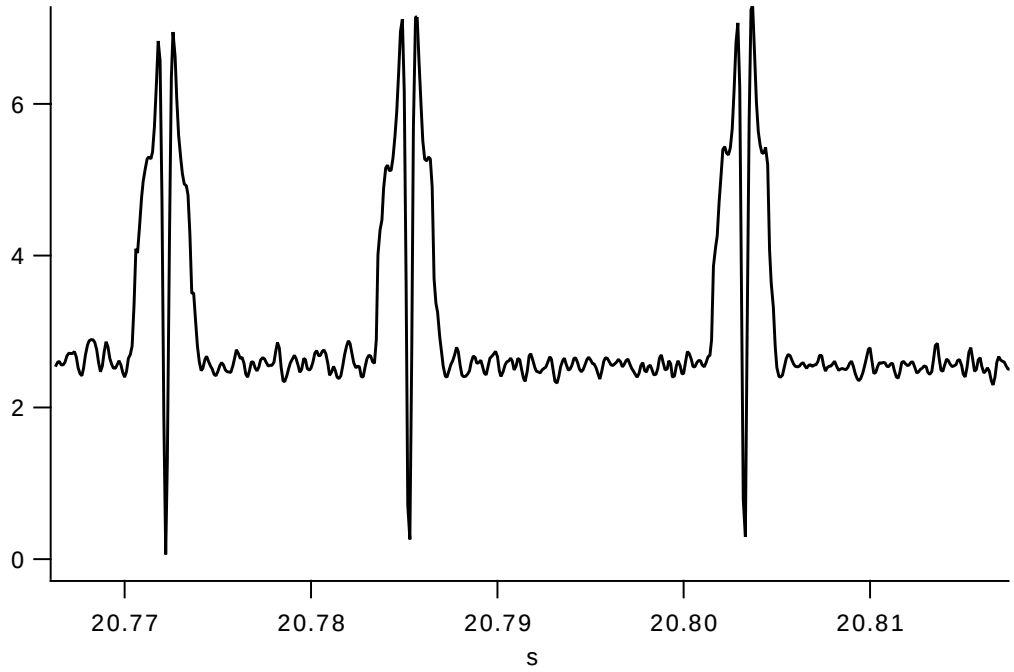

FIG. 5.5: Spike-matching function (in arbitrary units) created by convolving the spike template with the original recording. A threshold is selected below the baseline to pick out the spikes.

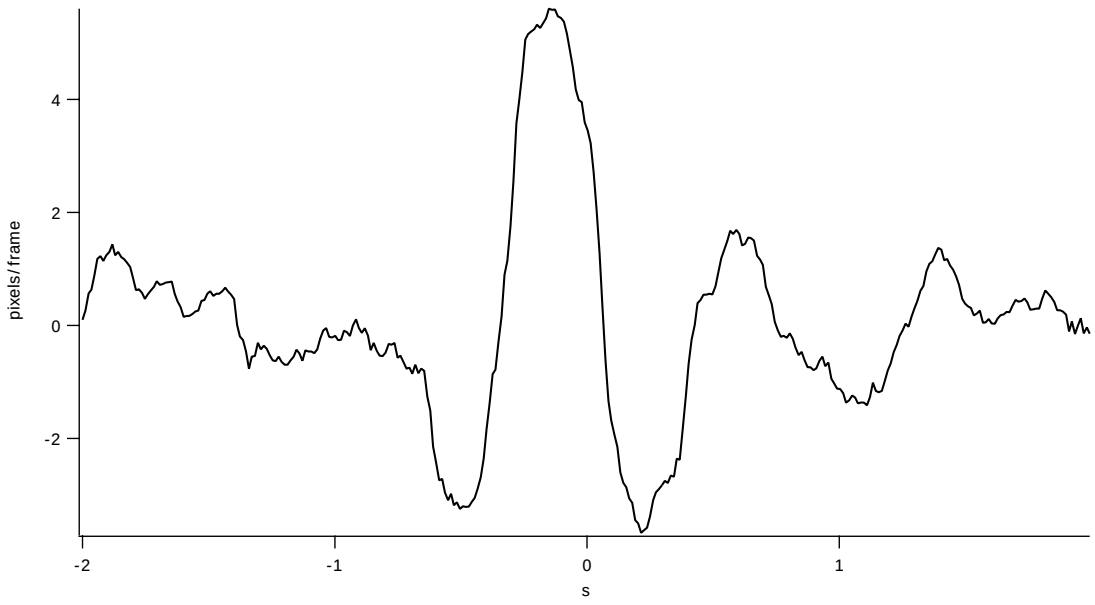

FIG. 5.6: STA for spike train 1-57 over the interval $-2\text{ s} \leqslant \tau \leqslant 2\text{ s}$. The spike-triggered average for a single 60 s trial is rather noisy, and there appears to be structure in the region $\tau > 0$.

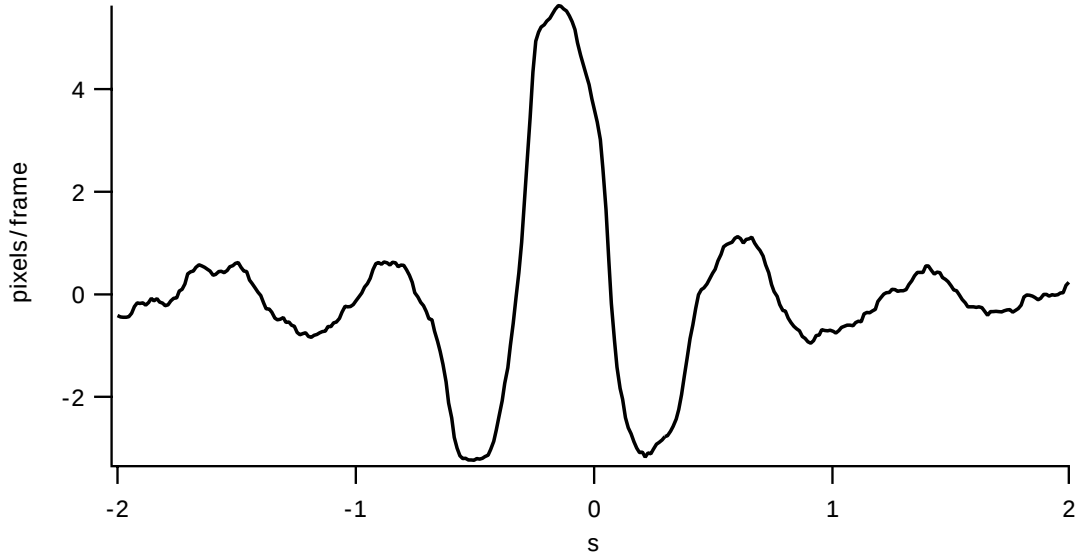

FIG. 5.7: Average STA of several trials on the same cell for the interval $-2\text{ s} \leqslant \tau \leqslant 2\text{ s}$. This STA is much cleaner, though the effects of stimulus autocorrelation are even more pronounced.

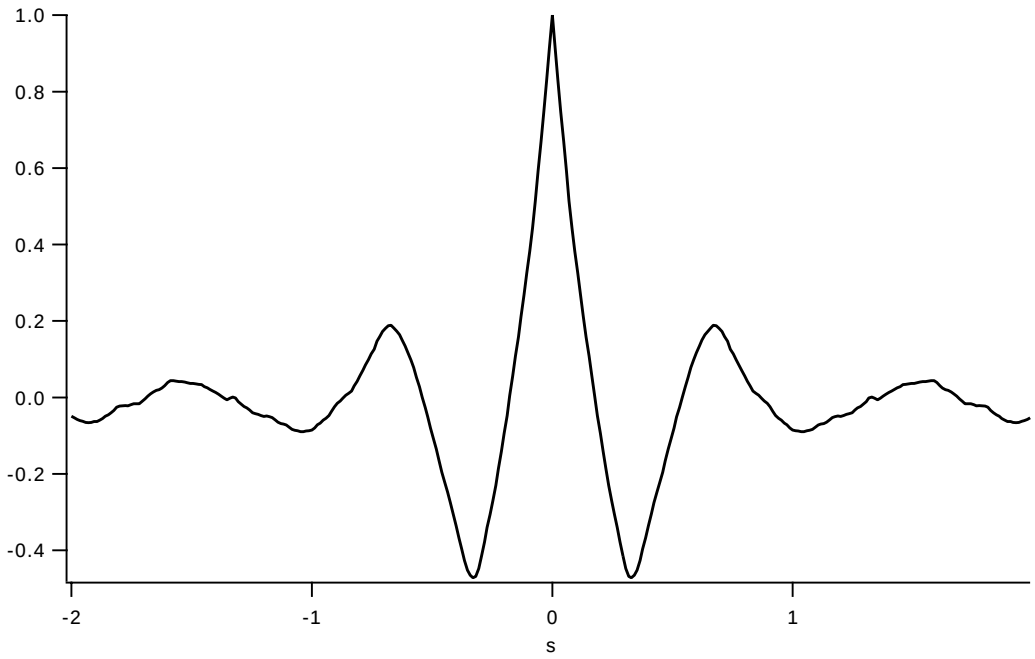

FIG. 5.8: Temporal autocorrelation of stimulus 1-57. The periodic, exponentially decaying autocorrelation of the edge stimulus closely resembles the resultant STA. Note that units of the AC are dropped per convention.

these features are the result of a strong influence of the stimulus AC. Although the AC can be manipulated somewhat by adjusting the probabilities for random velocity changes (see Appendix A), it cannot be completely avoided if the edge is meant to approximate continuous motion. It is hoped that the reverse correlation method discussed in Chapter 3 will be of some use in revealing more subtle properties of the DS cell.

5.3 False Frequencies in the Wiener Kernel

As previously noted, the Wiener kernel approximates the effect that an arbitrary stimulus at time $t-\tau$ will have on the neural response at time t. The Fast Fourier Transform (FFT) and Inverse Fast Fourier Transform (IFFT) functions built into *Igor* are used to calculate the Wiener kernels according to Eq. (3.19). The success of this procedure is limited by the refresh rate of the monitor. Frequencies above 85 Hz cannot legitimately contribute to the power spectrum of the stimulus, because the stimulus simply cannot move that fast. When $\hat{Q}_{rs}$ is divided by $\hat{Q}_{ss}$, the small values of $\hat{Q}_{ss}$ at high frequencies divide the values of $\hat{Q}_{rs}$ at high frequencies, which causes them to blow up. Consequently, these higher frequencies are over-represented in D, as seen in Fig. 5.11. The STA and AC for this trial (2-55) are presented in Figs. 5.9 and 5.10.

This false frequency problem was attacked in a number of different ways, but every method considered has essentially the same concept at its core: throw away the high frequencies. This task can be accomplished using *Igor's* built-in Gaussian smoothing routine. This method of smoothing removes high frequencies by adjusting the value of each point to an average of neighboring point values weighted according to a Gaussian of user-defined width. When the higher frequencies are neglected some of the actual structure is lost as well, the effect of which can be seen in the smoothed kernel corresponding to spike train 2-55 (Fig. 5.12). Although the signal is extremely noisy, it is encouraging to note that the kernel returns to the region of baseline noise before $\tau = 0$. Additionally, there is no evidence of the exponentially decaying periodicity seen in the autocorrelation of the stimulus.

Averaging kernels from multiple trials helps to reduce the noise and makes the actual structure somewhat clearer, as demonstrated in Fig. 5.13. This kernel is constructed from data for trials 2-55, 2-57, 2-61, 2-63, 2-65, 2-61a, 2-63a, 2-66, and 2-68. The

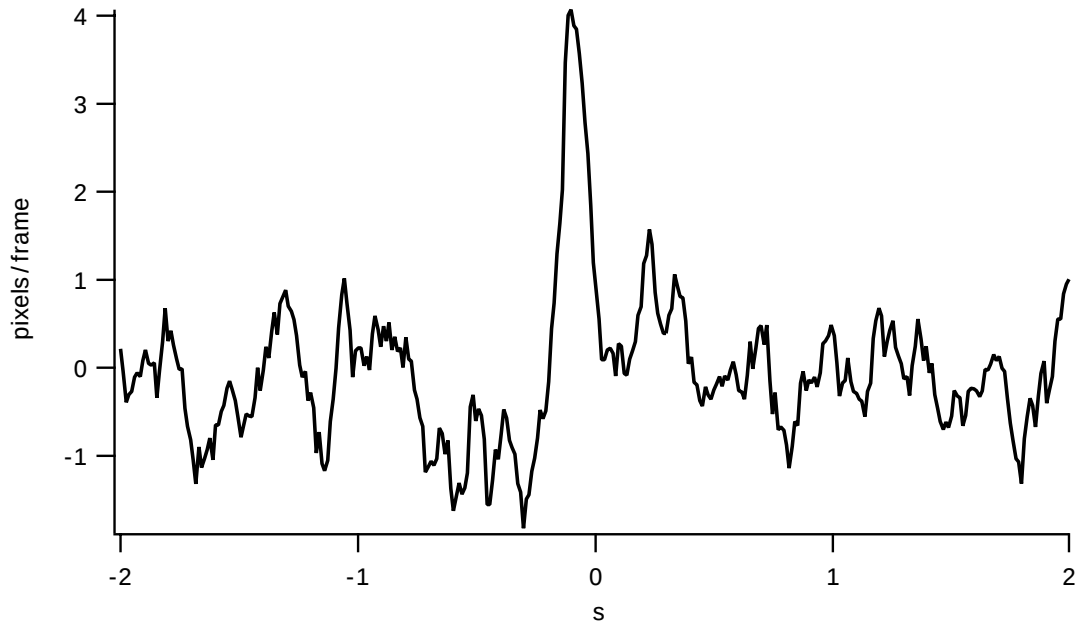

FIG. 5.9: Spike-triggered average for spike train 2-55. Note the acausal element is slightly different than that of Fig. 5.6.

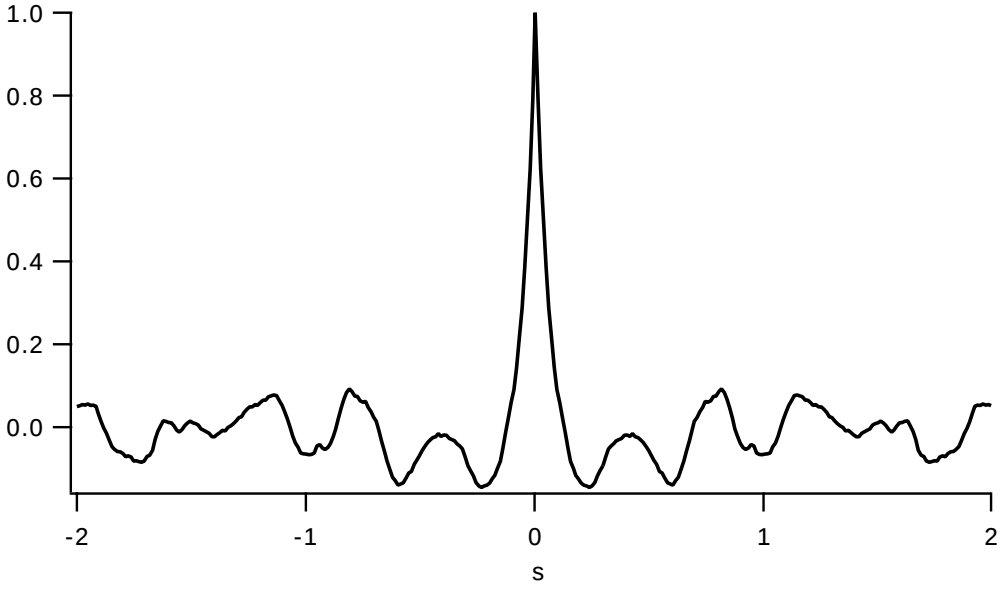

FIG. 5.10: Autocorrelation function for stimulus 2-55. The periodic variance matches that of the STA in Fig. 5.9.

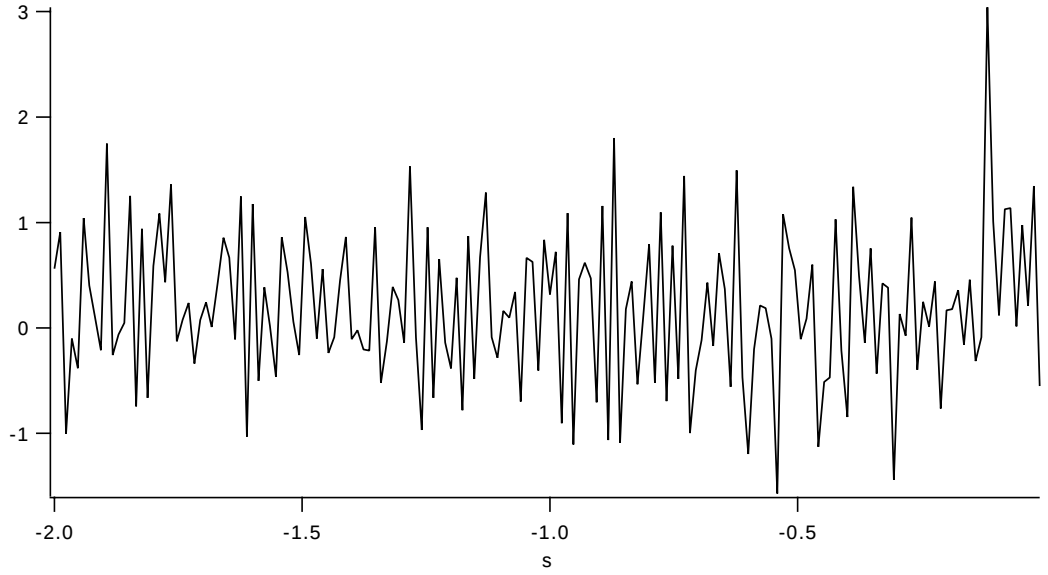

FIG. 5.11: Wiener kernel for spike train 2-55. Division by small numbers in Fourier space causes high frequencies to destroy the shape of the function.

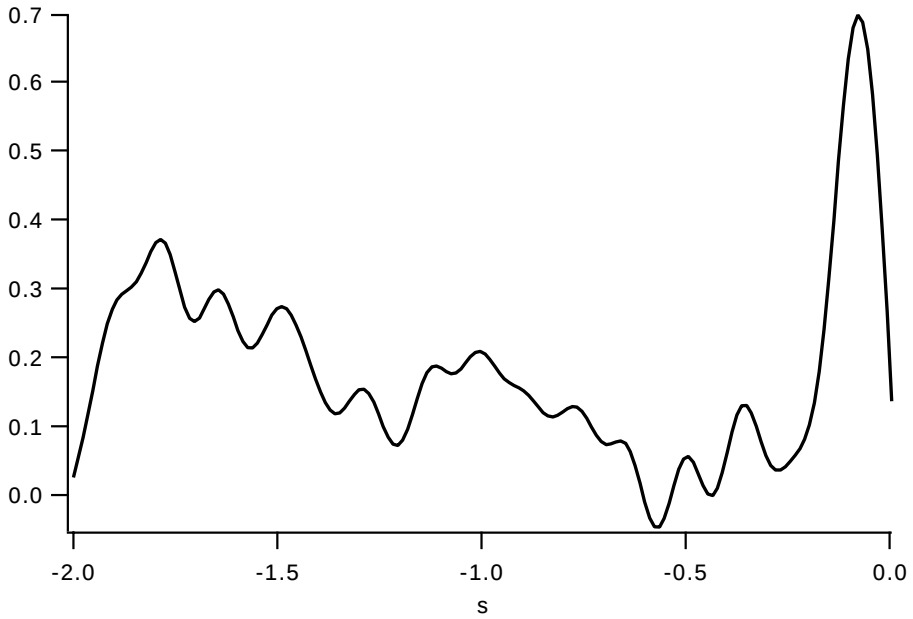

FIG. 5.12: Smoothed kernel for spike train 2-55, the first of nine data sets used to construct the kernel in Fig. 5.13. High frequencies have been removed at the cost of resolution, and the signal is still quite noisy. Note that the Wiener kernel, like the autocorrelation, does not carry meaningful units.

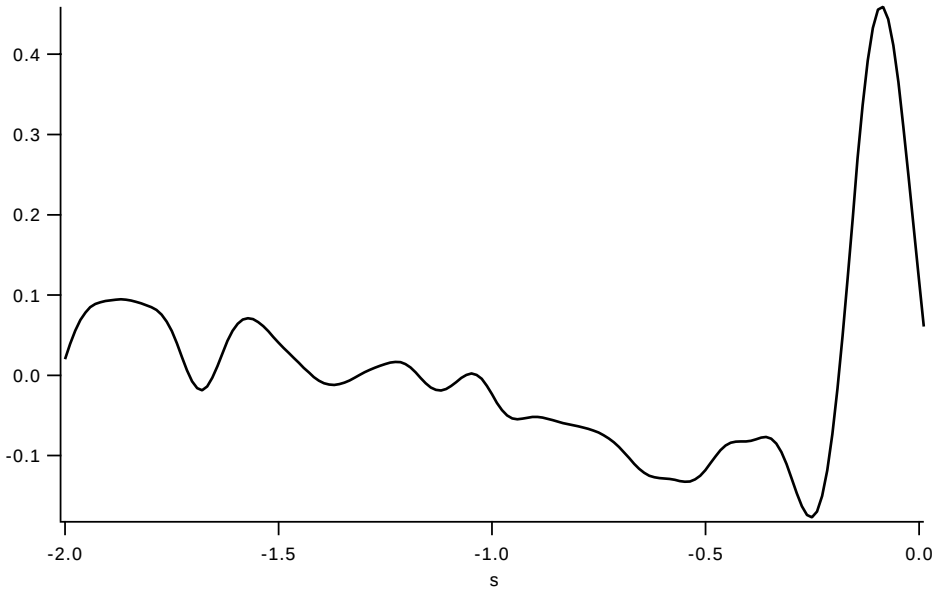

FIG. 5.13: Average of smoothed kernels from multiple trials. The average smoothed kernel is much clearer than the kernel from a single trial.

smoothed and averaged kernel clearly demonstrates a strong positive correlation between the stimulus and the response for $\tau \approx 100$ ms. The kernel also suggests a much weaker negative relationship between the stimulus and response for $\tau \approx 250$ ms. Several neurons are known to respond more strongly when excitation follows inhibition. It is unclear if the negative correlation in the Wiener kernel indicates that DS cells exhibit this behavior, or if the negative correlation should be attributed to noise. A possible extension of this thesis would be to investigate this problem explicitly with an appropriately designed experiment.

5.4 Intracellular Results

Intracellular recordings were made with the intent that more non-trivial data points could be obtained per experimental trial, and the SNR would be improved. When the spikes are removed from the data, the neural response can be represented as a continuous function as shown in Section 3.5. As demonstrated in the following analysis, the attempt to generate a better SNR proved to be only partially successful. The results from analysis of intracellular recordings closely match those from the extracellular data.

Intracellular data consists of a spike train on top of a continuous membrane current. All of the analysis performed on the spike trains recorded externally can be applied to the spike trains of the intracellular data. Additionally, the spikes can be removed, and the membrane current can be analyzed by itself. Spikes were removed from the data using the knowledge that a spike results in a very sharp rise in the current, which implies a high current time derivative at the beginning of a spike. When the current derivative reached a certain value, the current amplitude was held constant until the spike was over and the current returned to that amplitude. Thus a spike free data set was obtained.

According to Eqs. (3.6) and (3.20), correlating the stimulus with the response should produce a function equivalent to the flipped STA for the stimulus, unless there is a significant difference between the data contained in the intracellular current and the data contained in the spike train. An immediate attempt to perform this correlation does not produce the expected results. Rather, the correlation function is swamped in noise.

Investigation of this problem revealed that the cell only responded to the stimulus during part of the trial. The stimulus was presented to an area of the retina that was significantly larger than the receptive field of the neuron. The cell's response can not be correlated with the stimulus when the two are not spatially aligned. Since the receptive field is much smaller than the domain of the stimulus, the correlation function is significantly diluted. This problem did not arise in the analysis of the spike train data because spikes only occur when the cell *does* respond to the stimulus.

One-dimensional maps of the neuron's receptive field are used to overcome this issue. The receptive field map, such as the one calculated for trial 2-159 and displayed in Fig. 5.14, is created by assigning each spike a position that corresponds to where the stimulus was at a time just before the spike occurred. The time delay is determined by the maximum value of the Wiener kernel, obtained from the neuron's spike train. A new stimulus function is created by scaling the original stimulus velocity by a position dependent gaussian. If the edges of the receptive field are defined as x_1 and x_2 and the

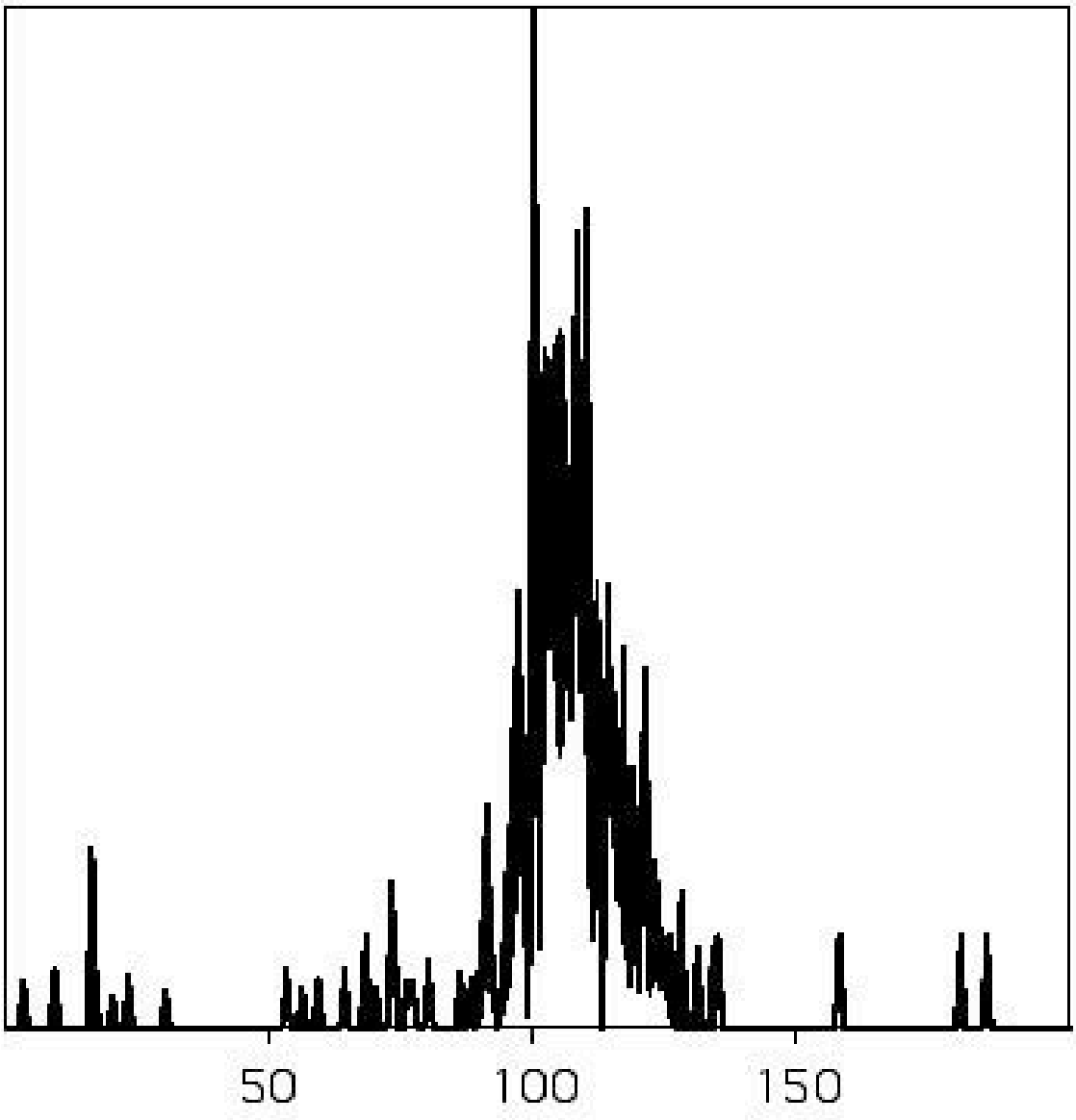

FIG. 5.14: One dimensional receptive field map of a DS cell. The spikes counted are from trial 2-159. The x axis is aligned with the axis of the preferred direction. Specific values of the y coordinates are arbitrary. The range of x corresponds to the 202 pixels of the screen. Most of the spikes are confined to $x_1 = 75 < x < 140 = x_2$. The rest of the spikes are attributed to stochastic firing.

position of the stimulus is $x(t)$, then the stimulus transforms as

$$s(t) \rightarrow \begin{cases} s(t)e^{[(x(t)-x_1)/30]^2} & \text{if } x(t) < x_1 \\ s(t) & \text{if } x_1 < x(t) < x_2 \\ s(t)e^{[(x(t)-x_2)/30]^2} & \text{if } x(t) > x_2. \end{cases} \tag{5.1}$$

This transformation is shown in Fig. 5.15 for the stimulus used in trial 2-159.

Using the transformed stimulus in the correlation function produces a result that is quite similar to the reverse STA, though there is necessarily a scaling factor, as seen in Fig. 5.16. There appears to be less noise in the intracellular correlation function, in the sense that the signal is less jagged. On the other hand, intracellular correlation is more heavily influenced by the stimulus autocorrelation. The stimulus autocorrelation corresponding to the intracellular correlation function is slightly different than the stimulus autocorrelation corresponding to the STA because a transformed stimulus was used to calculate the correlation function. The two autocorrelation functions are compared in Fig. 5.17.

Because the intracellular correlation function so closely resembles the STA and the autocorrelation functions are good approximations of one another, it is reasonable to expect the Wiener kernel calculated from the intracellular correlation function to mimic the Wiener kernel calculated from the STA. This is confirmed in Fig. 5.18 for trial 2-161. The similarity between the two kernels demonstrates that, in the first-order approximation, there is little or no information lost as the continuous membrane potential is converted into a spike train.

If the stimulus is inverted so that the dark side becomes the bright side and vice versa, the Wiener kernel for intracellular data becomes negatively correlated with the stimulus, as can be seen in the intracellular Wiener kernel of trial 2-160 (Fig. 5.19). This effect varies with changes in luminance. Since the spikes only relate excitation, however, the extracellular Wiener kernel exhibits the usual positive correlation. It may be possible to use this fact to explore relationships between inhibition and excitation or On-channel and Off-channel stimulation. The data collected for this thesis is not sufficient for this purpose, though it seems to be a logical extension.

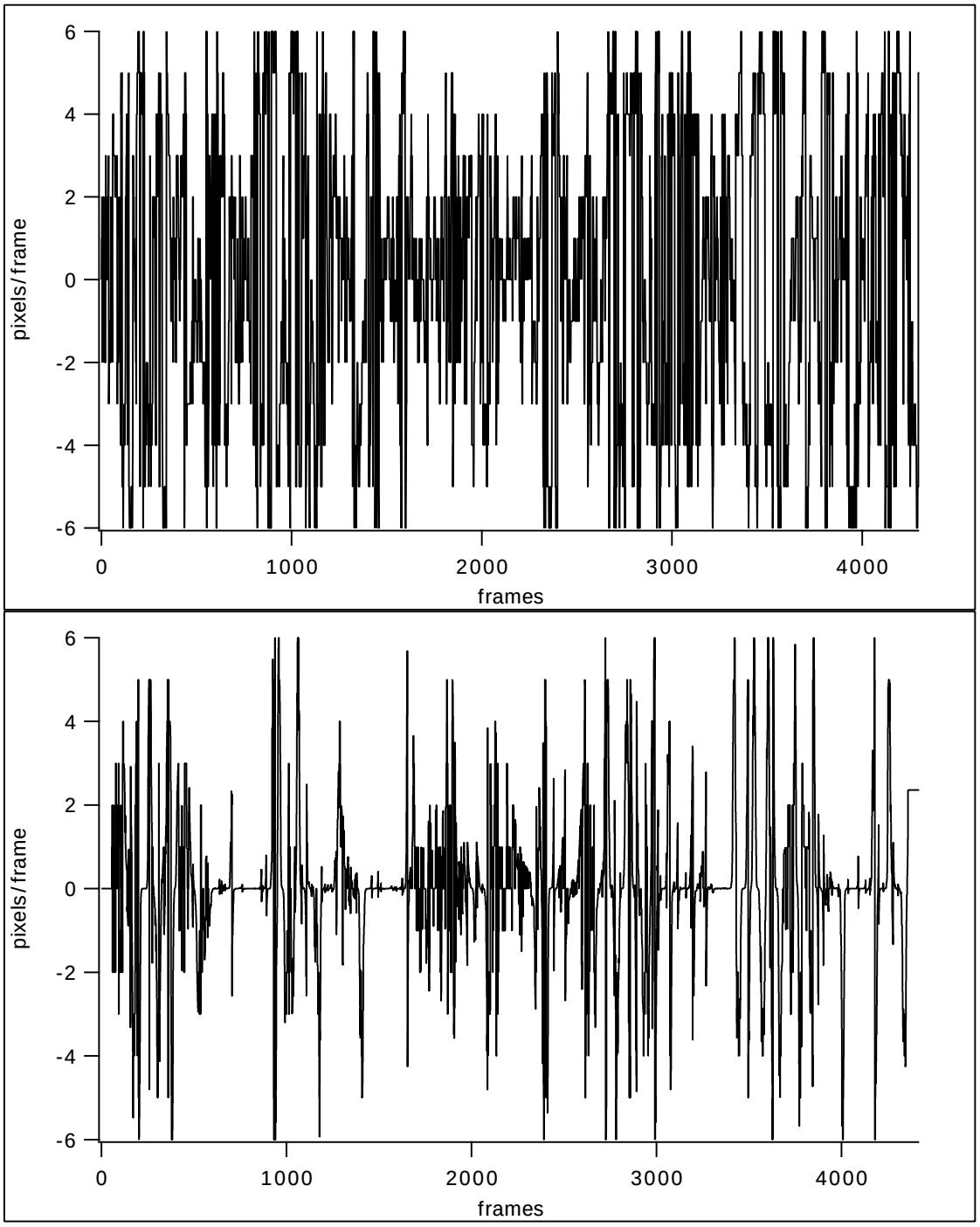

FIG. 5.15: Stimulus transformation for trial 2-159. The stimulus is scaled with a position dependent gaussian.

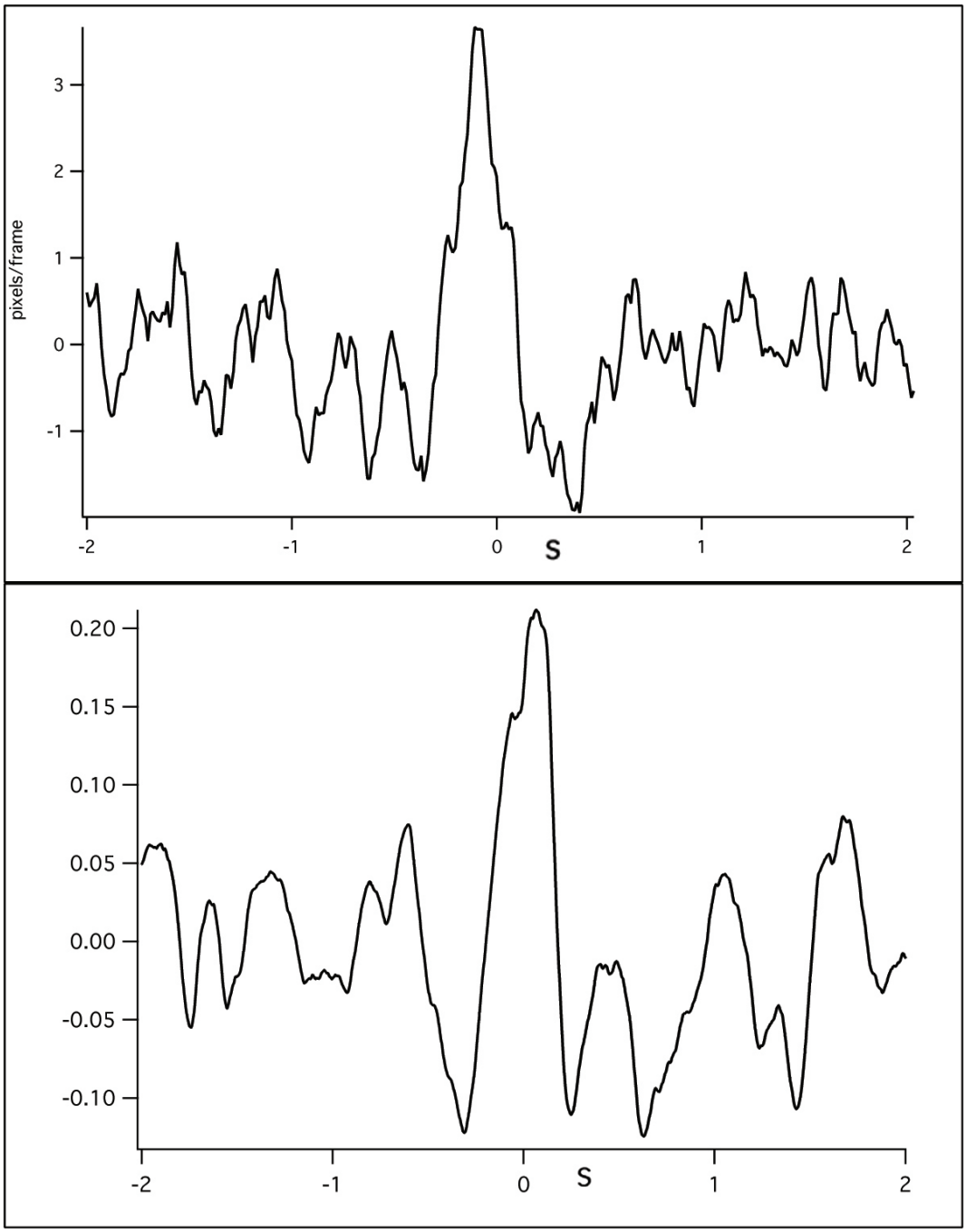

FIG. 5.16: The STA (*top*) calculated from spike train 2-161 compared with the reverse correlation function (*bottom*) calculated from the intracellular data of the same trial. Note that the peak of the STA occurs before zero, while the peak of the bottom graph occurs after zero. The shapes are quite similar, although they are influenced by different stimulus autocorrelations since the intracellular correlation function was calculated using the transformed stimulus. There is also a difference in scale.

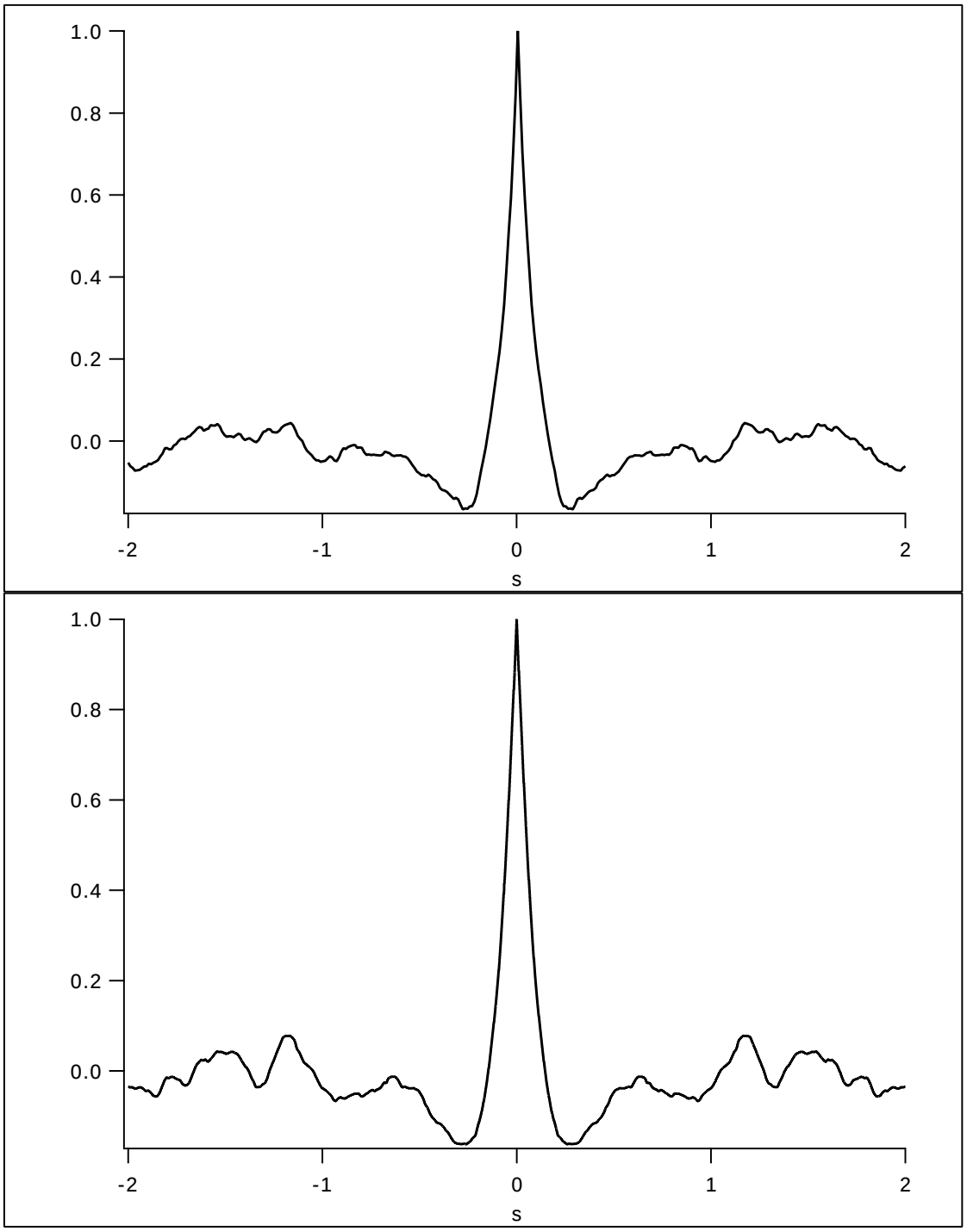

FIG. 5.17: Comparison of autocorrelation functions for original stimulus (*top*) and transformed stimulus (*bottom*).

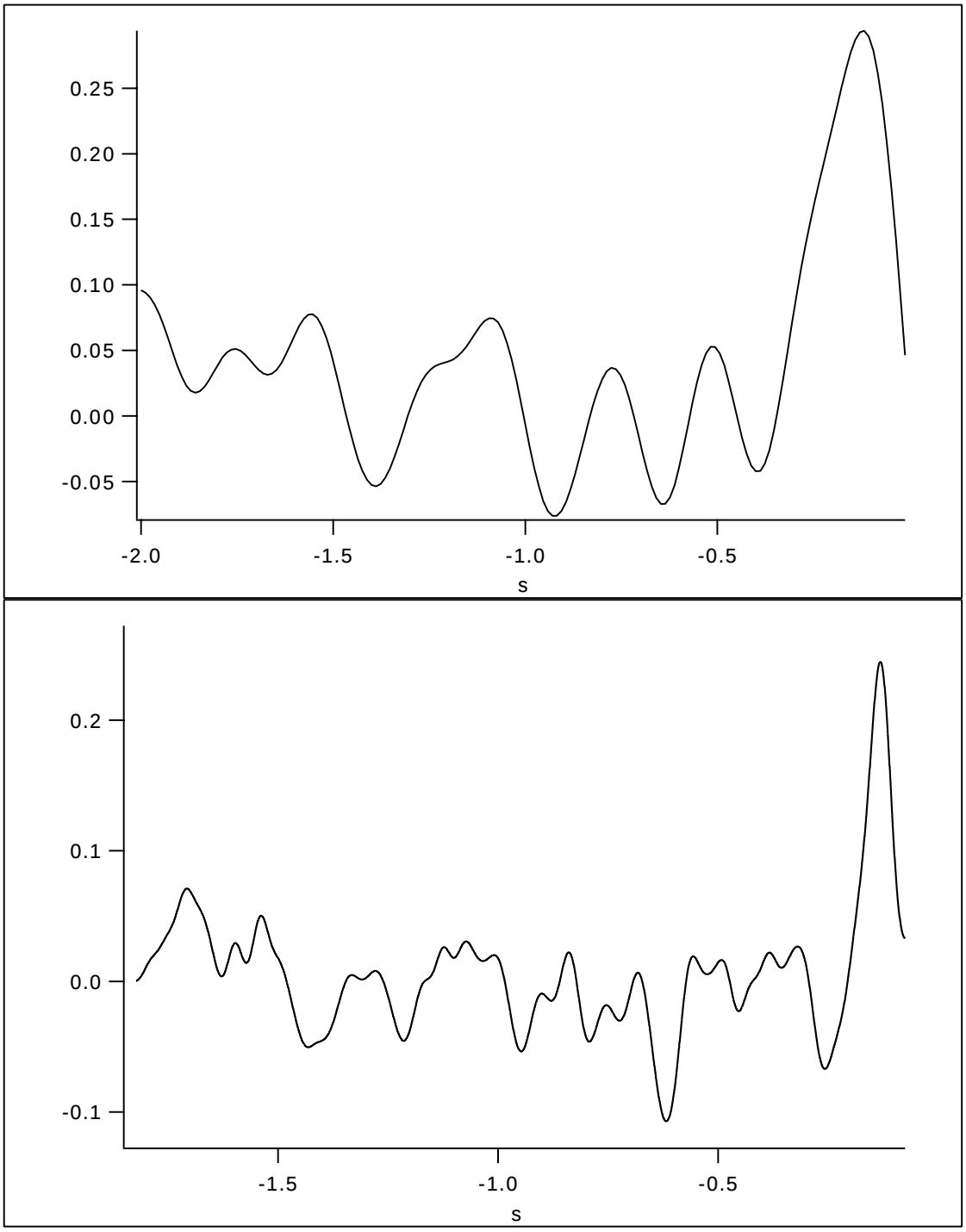

FIG. 5.18: Comparison of Wiener kernel calculated using STA (*top*) and intracellular correlation function (*bottom*) of trial 2-161. Discounting noise, the kernels are approximately similar. The somewhat broader correlation period shown in the extracellular kernel is likely due to differences in smoothing.

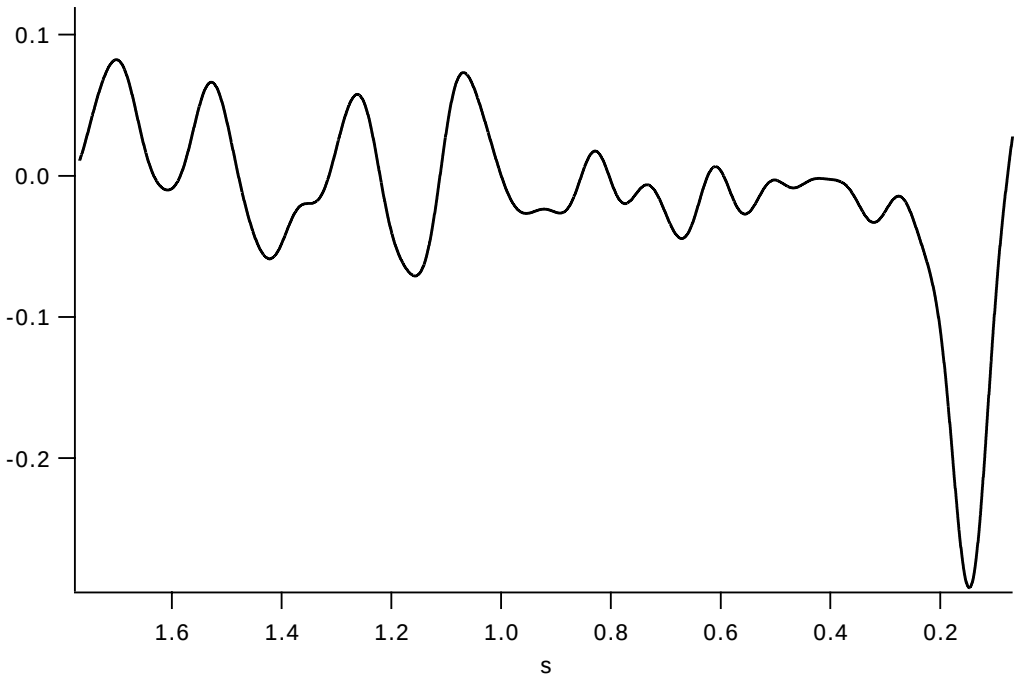

FIG. 5.19: Wiener kernel for intracellular data from inverted version of stimulus 2-161. The stimulus is negatively correlated with the response because On-channel inhibition overpowers Off-channel excitation.

5.5 Predicting Spike Bursts

The data collected shows that DS cells tends to respond to the edge stimulus with clusters, or *bursts*, of spikes. The surprising success of predicting these bursts with a first-order Wiener kernel validates the first order approximation. According to Eq. (3.10), the neural response can be estimated by convolving the kernel with the stimulus. It is again necessary to use the transformed stimulus, because that is all that the neuron "sees." The neural response estimate for trial 2-159 is shown in Fig. 5.20. Apparently, this convolution does not constitute a prediction of the spike train in itself.

The actual spike times are generally stochastic in nature [27], and it is difficult to predict individual spikes with this method. The response estimate does predict the times at which spikes are likely to occur. A threshold is applied to the response estimate to produce an "outline" of the spike train, as seen in Fig. 5.21. This threshold can be tweaked until the prediction accounts for most of the spikes. Presumably, the threshold is related to the intensity of the stimulus, although there is currently a lack of data to confirm this. Once an appropriate threshold has been determined, it is possible to use an average kernel from several sets of data to predict the spike bursts for a different set of data.

Fig. 5.21 shows that the prediction can be quite accurate. Twelve bursts correspond directly to predicted bursts; three bursts occur slightly before a predicted burst; and only two appear to be completely unrepresented in the prediction. Consequently, it can be concluded that the original first-order approximation is valid, and there is little to be gained from the labor of calculating higher-order kernels. Presumably, however, more sophisticated models could be generated to account for missed bursts.

5.6 Predicting Spikes

An unexpected, yet quite welcome result falls out of the receptive field maps calculated for the intracellular analysis. The edge stimulus will necessarily spend more time in the receptive field when it moves slowly than when it moves quickly. In fact an edge moving twice as fast would move across the receptive field in half the time. As a result, it would be expected that a slow moving stimulus would generate more spikes unless the frequency of spike generation depends on the speed of the stimulus. In this case, the STA would

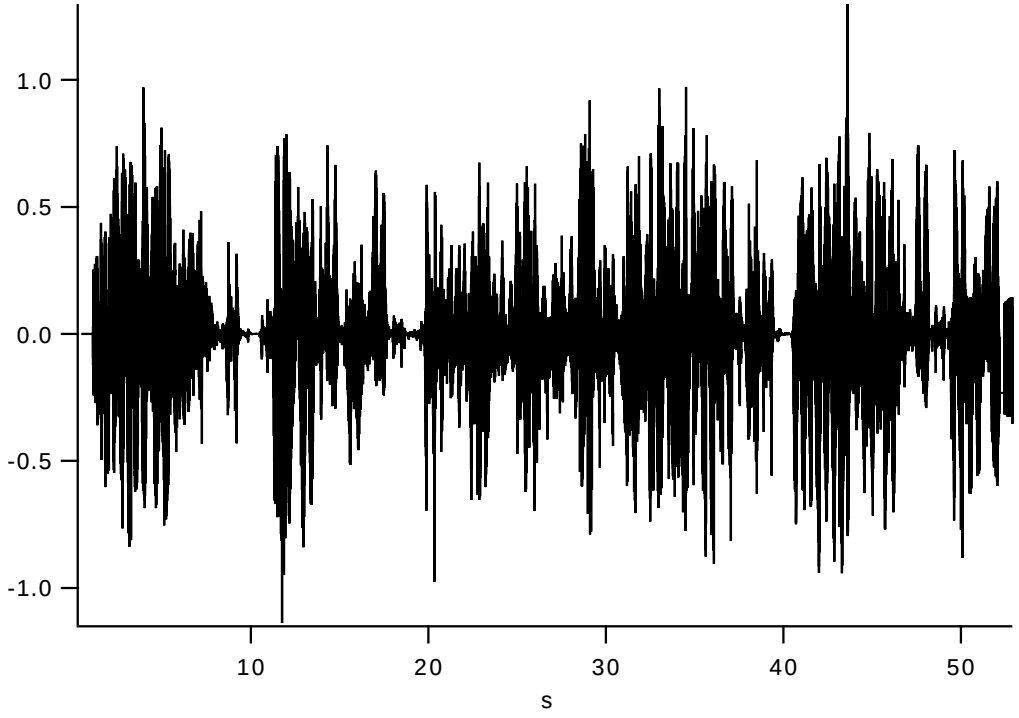

FIG. 5.20: Neural response estimated by convolution of kernel and stimulus for trial 2-159. The neural response itself is unitless, as defined in Chaper 3. The function shows the regions where spikes are most likely to occur, assuming a linear relationship.

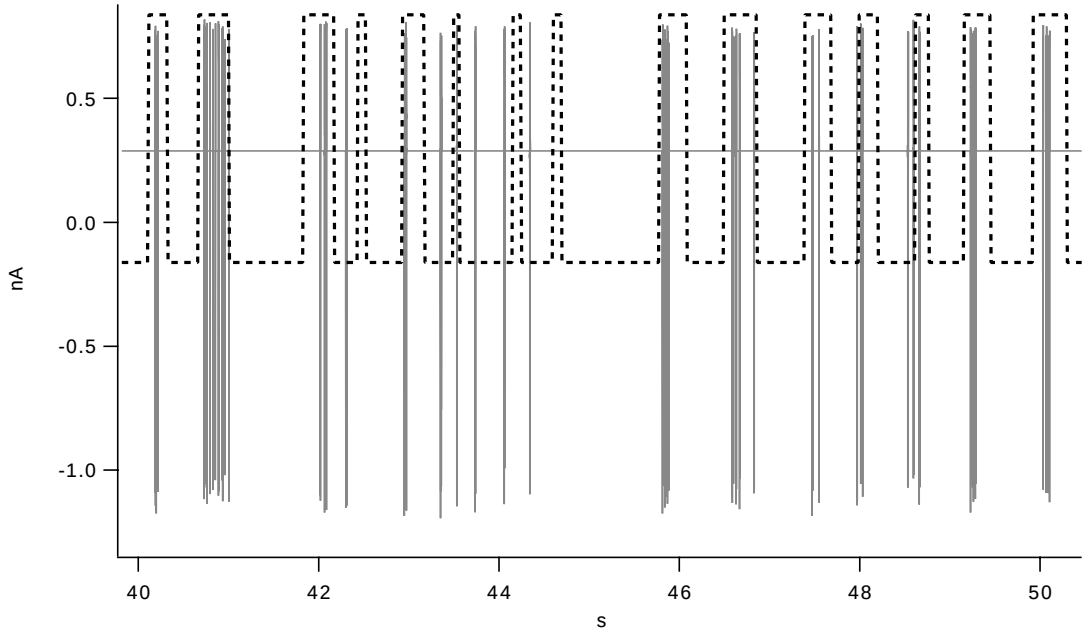

FIG. 5.21: Prediction of spike bursts with actual spike train recorded for trial 2-42. The bold, dashed line is the spike burst prediction, and the lighter line is the actual record. The spike bursts were predicted by applying a threshold to the the neural response estimate. The kernel used was calculated with data averaged from other runs, so the dashed line is actually a prediction rather than a recreation. Note that most spikes correspond to a predicted burst, and vice versa.

be biased towards low speeds.

Actual data shows, however, that the maximum value of an STA inevitably falls at the average value of the positive speeds of the stimulus (for example, see Figs. 5.6 and 5.7, in which the average stimulus speed is 5). It can be inferred from the lack of bias that as many spikes are generated at high speeds as are generated at low speeds, and the spiking frequency must be greater for higher stimulus speeds. Analogously, the HH model predicts higher spiking frequencies for higher injected currents. Thus the HH model was used to describe the correlation between stimulus speed and neural response.

The HH equations (Eqs. (2.30), (2.31), (2.32), and (2.39)) were solved using *Mathematica*. It was necessary to specify initial conditions to solve the equations numerically. Together, the HH equations and initial conditions take the form

```
initial :=
 {v[0] == 0, m[0] == m∞[0], n[0] == n∞[0], h[0] == h∞[0]}

diffeqs := {m'[t] == αm[v[t]] (1 - m[t]) - βm[v[t]] m[t],
  n'[t] == αn[v[t]] (1 - n[t]) - βn [v[t]] n[t],
  h'[t] == αh[v[t]] (1 - h[t]) - βh[v[t]] h[t],
  c v'[t] + gNa[t] (v[t] - ℰNa) +
    gK[t] (v[t] - ℰK) + gleak (v[t] - ℰleak) == i[t]},
```

where $'$ denotes the time derivative, and resting potentials are represented by $\mathcal{E}$s. The rate constants and electrical parameters used in this model were taken from a paper in which they were originally fit for data from DS cells in a cat retina [31]. They were then altered slightly to improve the model. The electrical properties of the cell are defined as

$$
\begin{aligned}
&\bar{g}_{Na} = 150\\
&\bar{g}_{K} = 90\\
&g_{leak} = 0.25\\
&c = 1\\
&\mathcal{E}_{Na} = 75\\
&\mathcal{E}_{K} = -85\\
&\mathcal{E}_{leak} = -70\\
&g_{Na}[t\_] = \bar{g}_{Na}\, m[t]^3\, h[t]\\
&g_{K}[t\_] = \bar{g}_{K}\, n[t]^4,
\end{aligned}
$$

where the potentials are in mV, the conductances g are in nS (nano-Siemens), and the capacitance c is in pF. The rate constants are defined in the conventional forms (see Section 2.4):

$$\alpha_m[v\_] := \frac{0.5\,(v+29)}{1-\text{Exp}[-0.18\,(v+29)]}$$

$$\beta_m[v\_] := 6\,\text{Exp}\left[-\frac{v+45}{15}\right]$$

$$\alpha_h[v\_] := 0.15 * \text{Exp}\left[-\frac{v+47}{20}\right]$$

$$\beta_h[v\_] := \frac{2.8}{1+\text{Exp}[-0.1\,(v+20)]}$$

$$\alpha_n[v\_] := \frac{0.0065\,(v+30)}{1-\text{Exp}[-0.3\,(v+30)]}$$

$$\beta_n[v\_] := 0.083\,\text{Exp}\left[-\frac{v+15}{15}\right]$$

$$m_\infty[v\_] := \frac{\alpha_m[v]}{\alpha_m[v]+\beta_m[v]}$$

$$h_\infty[v\_] := \frac{\alpha_h[v]}{\alpha_h[v]+\beta_h[v]}$$

$$n_\infty[v\_] := \frac{\alpha_n[v]}{\alpha_n[v]+\beta_n[v]} \quad .$$

The stimulus velocity is taken from *Igor* and converted to a membrane current in *Mathematica* by scaling the positive values up and the negative values down, as this matches the actual data much better than using an identical scalar for both positive and negative values. The precise values of the scalars are adjusted to better reproduce the actual spike train, though optimal values have yet to be deduced. Once the current has been defined the HH equations are solved, and the membrane potential is plotted.

As can be seen in the comparison of a reproduced spike train with the actual spike train in Fig. 5.22, this prediction method is far from reliable. This model is still in an infantile stage of development, and it is likely that additional manipulation of the stimulus transformation procedure, the rate constants, and electrical constants could greatly improve this model. Ideally, each of these parameters would be systematically optimized to produce reliable predictions.

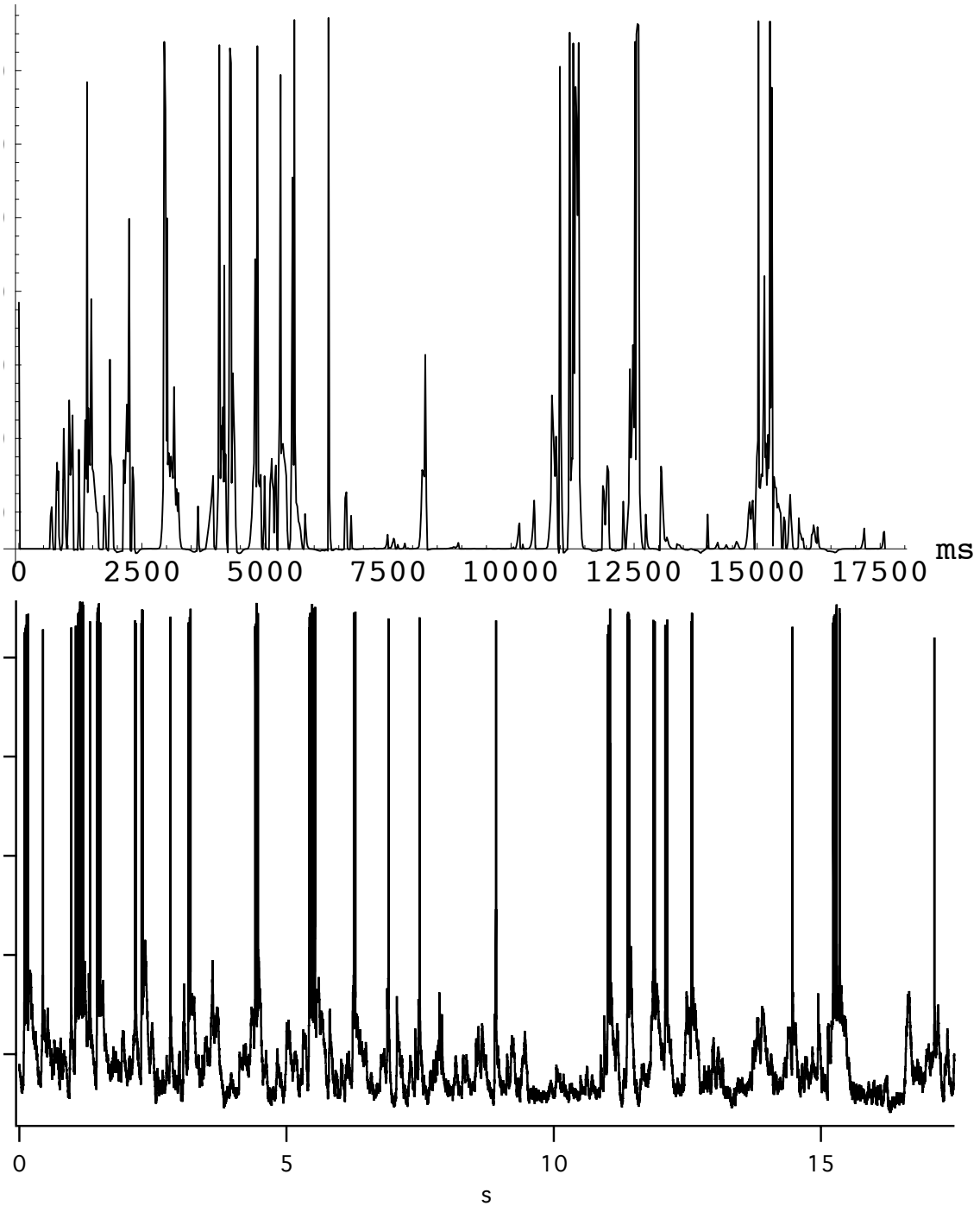

FIG. 5.22: A HH-like model is used to predict spikes for trial 2-159 with limited success. Although spikes appear in roughly the same places in each graph, the HH prediction (*top*) misses many of the spikes seen in the actual record (*bottom*). Presumably, this could be improved in future versions of the model.

5.7 Conclusion

A comparison of Figs. 5.21 and 5.22 shows that the Wiener kernel predictions are much more accurate than the HH model spike-train predictions. In general, the kernel prediction accounts for 75% to 85% of the bursts in the actual spike train. Unfortunately, the neural response estimate does not allow for the prediction of individual spikes. The relevant literature [28] suggests that individual spikes can be predicted using a Wiener kernel by averaging multiple presentations of an identical stimulus and calculating an average neural response estimate called a firing rate estimate. This method must also be incomplete, though, as it fails to address dynamical changes in the cell's response, such as adaptation to a stimulus.

The HH model is conveniently designed to handle such cell dynamics. For example, adaptation can be accounted for by adding Ca^{2+} ion channels to the HH model [31]. Theoretically, a HH-like model should be able to accurately predict not only bursts, but the number of spikes within each burst to a good approximation. (It is not, of course, possible to predict the exact timing of each spike due to the stochastic nature of action potential generation.) Currently, the HH model in this thesis yields at best a rough estimate of the actual spike train. It appears entirely feasible, however, that improvements to the model could produce predictions that are at least as accurate as those generated by the Wiener kernel method.

5.8 Suggested Extensions

Several extensions of this research have been suggested based on the inconclusive results found in this chapter. Other possibilities with broader foundations may be found in the relevant literature. In particular, decoding information from and modeling populations of retinal ganglion cells is currently a popular endeavor among scientists, and the literature is correspondingly extensive [28, 15]. Specifically, this problem would address the number of cells needed to efficiently and completely recreate a given stimulus.

The one-dimensional receptive field maps created in this thesis serve a very specific purpose, while highly detailed multi-dimensional receptive field maps of sensory neurons can reveal an incredible amount of information regarding the nervous system. This problem is also closely related to modeling responses of populations [32].

Perhaps the most obvious extension would be to attempt a refinement of the HH-like DS cell model. Computers can be used to find optimal parameters for the rate constants and other parameters that minimize the difference between the predicted response and the actual response. The model may also be improved by including calcium channels, which would help modulate spiking frequency and adaptation [18, 31].

Appendix A

Igor Code

The important elements of the *Igor* Code used for analysis are detailed in the following sections. These sections do not constitute a complete, working program, yet it should be elucidating enough that the ambitious reader would be able to recreate a reasonable facsimile of the original program using almost any full-featured mathematical software.

Important comments generally precede code, although certain less important comments are found within the code and delimited by a `//`. Similarly, most of the important variables are described in the text, whereas the reader is expected to recognize the purpose of the less important variables and indices from contextual clues. *Igor*'s syntax is unique in that lists of numbers or letters, most commonly known as arrays, are called *waves* in *Igor*. Waves should be considered to be one-dimensional unless otherwise noted.

A.1 Spike Train Filtering

Analysis of the data begins by cleaning up the spike train. The original data record, which consists of an array of current values recorded at 0.1 ms intervals, is loaded into memory under the wave name `CurrentData`. The average value of `CurrentData` is determined with `wavestats`, and a new wave, `Fil_out` is set equal to this value at all points. Each segment of `CurrentData` is checked to see if it surpasses the upper and lower thresholds (`UpperTemp_thrHold` and `LowerTemp_thrHold`). If it does, that section is copied to `Fil_out` and stored in a two-dimensional wave called `Allspikes`. The number of spikes is counted by the variable `Temp_count`. Every spike stored in `Allspikes` is averaged together to create a spike template called `AvgSpike`. The spike

template is compared against CurrentData, and the square of the difference at each point is stored in a new wave, Sp_match.

```
wave CurrentData=root:CurrentData

wavestats/q CurrentData
Fil_out = V_avg

for(j=0;j < S_pnts;j+=1)
Sp_max=V_avg
Sp_min=V_avg
Single_wave=V_Avg
for(k=0;k<Sp_width;k+=1)
Single_wave[k]=Currentdata[j+k]
if((k>=Sp_Width/2)&&(Single_wave[k-Sp_width/2]<Sp_min))
Sp_min=Single_wave[k-Sp_width/2]
endif
if((k>=Sp_width/2)&&(Single_wave[k-Sp_width/2]>Sp_max)&&(Sp_min<LTH))
Sp_max=Single_wave[k-Sp_width/2]
endif
endfor
if((Sp_max > UpperTemp_ThrHold)&&(Sp_min < LowerTemp_thrHold))
Temp_count+=1
for(k=0;k<Sp_width;k+=1)
Fil_out[j+k]=Single_wave[k]
endfor
Allspikes[0, SP_Width-1][SP_number]=Single_wave[p-1]
InsertPoints/M=1 Temp_Count,1, Allspikes
j+=Sp_width // Avoid double-counting spikes.
endif
endfor
for(j=0;j<Sp_width;j+=1)
for(k=0;k<Temp_count;k+=1)
Sumspikes[j]+=Allspikes[j][k]
endfor
endfor
Avgspike=Sumspikes/Temp_count

for(k=0;k<Sp_width;k+=1)
Sp_match[0, S_pnts]+= (Avgspike[k]-Currentdata[p+k])^2
endfor
```

After Sp_match has been generated, the user defines a lower threshold, which is

stored in Com_thrHold. Each time Sp_match dips below this threshold, the spike time is counted in Com_count and added to the list Com_times.

```
for(j=0;j<S_pnts;j+=1)
if((Sp_match[j] < Com_thrHold)&&(Sp_match[j]<Sp_match[j-1])
&&(Sp_match[j]<Sp_match[j+1]))
Com_count+=1
endif
endfor

make/o/n=(Com_count) Com_times=0
for(j=0;j<S_pnts;j+=1)
if((Sp_match[j] < Com_thrHold)&&(Sp_match[j]<Sp_match[j-1])
&&(Sp_match[j]<Sp_match[j+1]))
for(k=0;k<Sp_Width;k+=1)
if((Currentdata[j+k]<Currentdata[j+k-1])
&&(Currentdata[j+k]<Lowertemp_thrHold))
Com_times[m]=(j+k)*deltax(Currentdata)
endif
endfor
m+=1
j+=Sp_width/2 // Skips a few points to avoid double counting spikes.
endif
endfor
```

A.2 Stimulus Reproduction

The edge stimulus is reproduced in two waves, EdgePosition and EdgeVelocity, using the seed that was used to create the stimulus. The random number generator was originally programmed by Rowland Taylor (NSI). Because there is nothing particularly unique about the random number generator itself, this section mainly serves to show the origin of the velocity and position stimulus reproductions and to show how certain random probabilities might be adjusted. Also note that the stimulus is confined by the maximum speed, MasSpeed, and the screensize, numpix.

```
temp=ran1(-seed)
for(j=0;j<size;j+=1)
if(j==0)
```

```
temp=ran1(-seed);
else
temp=ran1(seed);
endif
tS[j] = (temp < propd) ? -1 : 1 // Prob for position change
uS[j] = (temp < propm) ? -1 : 1 // Prob for speed change
vS[j] = (temp < 0.5) ? -1 :  1
endfor
for(j=0;j<noisesize;j+=1)
NS[j][0] = tS[mod((size+j-gunoffset*0),size)]
endfor
for(j=0;j<noisesize;j+=1)
NS[j][1] = uS[mod((size+j-gunoffset*1),size)]
endfor
for(j=0;j<noisesize;j+=1)
NS[j][2] = vS[mod((size+j-gunoffset*2),size)]
endfor

Duplicate/O NS tempWave
make/O/N=(length) EdgePosition
make/O/N=(length) EdgeVelocity
make/O/N=(length) EdgeTime=x/FrameRate+Delay*0.001

for(j=0;j<=length;j+=1)
EdgePosition[j]=pixel
EdgeVelocity[j]=speed
if(tempWave[j][0]<0)
speed=-speed
endif
if(tempwave[j][1] < 0)
if(((tempwave[j][2]<0)&&(Speed<MaxSpeed))||(speed==-MaxSpeed))
speed+=1
elseif(((tempwave[j][2]>0)&&(speed>-MaxSpeed))||(speed==MaxSpeed))
speed-=1
endif
endif
if((pixel == 2)&&(speed < 0))
speed = -speed
endif
pixel=pixel+speed;
if(pixel>=numpix)
pixel=2*numpix-pixel-1
speed=-speed
endif
if(pixel<=2)
```

```
pixel=4-pixel
speed=-speed
endif
endfor
```

A.3 Spike-Triggered Average

This section of code reads the spike times from `Com_times` to segregate each spike by the position at which it occurs in the two-dimensional wave `AllAbsSSP` and to generate the STA in a wave called `AvgSSV`. `AllAbsSSP` can be used to generate the receptive field map. The variable `CC` is the spike count, and `stimlength_fr` is the length of the stimulus window corresponding to each spike.

```
For(j=0;j<CC;j+=1)
Pointer=round((Com_times[j]-Stimlength_s-delay)*framerate)
AllAbsSSP[0,Stimlength_fr][j]=EdgePosition[pointer+p+stimlength_fr/2]
AllSSV[0, Stimlength_fr][j]=EdgeVelocity[Pointer+p+stimlength_fr/2]
SumSSV[0,Stimlength_fr]+=AllSSV[p][j]
Net+=1
Endfor
AvgSSV=SumSSV/Net
```

A.4 Removing Autocorrelation

The reverse correlation process begins by generating the autocorrelation of the stimulus velocity wave `vstim`, which is a duplicate of `EdgeVelocity`. The relevant sections are saved in `Qvv`, which is normalized to 1 at $t = 0$. The stimulus-response cross correlation, `Qrv`, is calculated from `AvgSSV`. FFTs are calculated and saved as `Qvv_ft` and `Qrv_ft`. The Wiener kernel, `Velkernel`, is the inverse FFT of `Qrv_ft` divided by `Qvv_ft`.

```
correlate vstim vstim

duplicate/o AvgSSV Qrv
Qvv[0,T-1]=vstim[(numpnts(vstim)-1)/2-T/2+p]/vstim(0)

setscale x, -stimlength_s/2, stimlength_s/2, Qvv
```

```
setscale x, -stimlength_s/2, stimlength_s/2, Qrv
duplicate/o/c Qrv Qrv_ft
duplicate/o/c Qvv Qvv_ft

FFT Qrv_ft
FFT Qvv_ft

Duplicate/c/o Qrv_ft VelKernel
VelKernel/=Qvv_ft
IFFT VelKernel
```

A.5 Intracellular Analysis

Intracellular recordings are first analyzed using the routines written for spike-train data. All spike-like elements are identified if they exceed the threshold `UpperTemp_thrHold`, and cut off at the point were the derivative of the current exceeds the allowed `slope`. The spikeless current record is shifted, scaled, and saved as `nospikes`.

```
for(j=0;j<length;j+=1)
NoSpikes[j]=currentdata[j]
if(currentdata[j]>UpperTemp_thrHold)
k=0
m=0
do
k+=1
while(abs(currentdata[j-k]-currentdata[j-k+1])>slope)
do
m+=1
while(currentdata[j+m]>currentdata[j-k])
NoSpikes[j-k,j+m]=currentdata[j-k]
j+=m
endif
endfor
avg=mean(nospikes)
nospikes-=avg
wavestats/q nospikes
nospikes/=V_max
```

Code used to generate the intracellular Wiener kernel is similar to that used to generate the kernel from the spike train. The most significant portion of the following

code is the transformation of the stimulus. First EdgeVelocity and EdgePosition are stretched and saved as LongVel and LongPos so that each sample point in the data has a corresponding stimulus value.

```
Function IC_Correlate()
for(j=0;j<size;j+=1)
LongVel[delay*10+(j)*skip, delay*10+(j+1)*skip-1]=edgevelocity[m]
LongPos[delay*10+(j)*skip, delay*10+(j+1)*skip-1]=edgeposition[m]
m+=1
endfor
```

The edges of the receptive field are calculated and stored as edge1 and edge2. If LongPos is located outside of the receptive field at some point, the corresponding point in LongVel is scaled by a gaussian function, so that the stimulus is muted the farther it travels from this region.

```
wavestats/q avgssv

do
j+=1
while((sumsegpos[v_maxloc][j-1]<=com_count)
||(sumsegpos[v_maxloc][j]<=com_count))
edge1=j

j+=15
do
j+=1
while((sumsegpos[v_maxloc][j]>=com_count)
||(sumsegpos[v_maxloc][j+1]>=com_count))
edge2=j

for(j=0;j<length;j+=1)
if(longpos[j]<edge1)
longvel[j]*=exp(-(((longpos[j]-(edge1))/(20))^2))
elseif(longpos[j]>edge2)
longvel[j]*=exp(-(((longpos[j]-(edge2))/(20))^2))
endif
endfor
```

The autocorrelation function and cross-correlation funtion are calculated and saved as Rvv and Rvx, respectively. FFTs of these waves are saved as Svv and Svx. The kernel

is calculated in the usual manner and stored as `ic_vkernel`. Finally, `ic_vkernel` is smoothed using *Igor*'s internal binomial smoothing routine.

```
duplicate/o nospikes Rvx
correlate longvel Rvx

duplicate/o longvel Rvv
correlate longvel Rvv
j=rvv(0)
Rvv/=j

duplicate/o Rvx Svx
duplicate/o Rvv Svv
deletepoints 0, (length-stim_sp/2-1), Svx
deletepoints (stim_sp), (length-stim_sp/2), Svx
deletepoints 0, (length-stim_sp/2-1), Svv
deletepoints (stim_sp), (length-stim_sp/2), Svv
setscale x, -(stimlength_s/2), (stimlength_s/2), Svx
setscale x, -(stimlength_s/2), (stimlength_s/2), Svv

fft Svx
fft Svv
duplicate/o/c Svx ic_vkernel
ic_vkernel=svx/svv
ifft ic_vkernel
smooth/E=2 smth, ic_vkernel
wavestats/q ic_vkernel
```

A.6 Spike-Burst Prediction

The neural response function is estimated by the convolution of the Wiener kernel, `ic_vkernel`, with the stimulus, `longvel`. The resultant wave is compared to a threshold value, `TH`. When the convolution is above the threshold, a spike burst is predicted and recorded in the wave `K_Burst`. This prediction may need to be scaled in order to be compared to the original spike record.

```
make/o/n=(numpnts(longvel)) K_burst=0
make/o/n=(m) K_Temp
K_temp[0, m-1]=ic_vkernel[m-1-p]
```

```
duplicate/o longvel K_match
convolve K_temp K_match
for(j=0;j<numpnts(k_match);j+=1)
if(K_match[j]>TH)
K_burst[j]=1
endif
endfor
```

Appendix B

Mathematica Notebook

This appendix details the important elements of a sample *Mathematica* notebook used to predict spikes via an HH-like model. The only portion of the *Mathematica* notebook which changes significantly from trial to trial is the injected current, which is based on the stimulus velocity. The equations and terminology that follow should be considered in the context of Chapter 2 for full comprehension.

As previously noted, the rate constants and electrical constants for the membrane were adapted from a model of a cat DS cell [31]. The constants listed below presumably are not optimal values for minimizing the error in this model. Ideally, an automated method of optimizing these constants could be devised as an extension of this project. The rate constants were defined in *Mathematica* as

$$\begin{aligned}
\alpha_m[v_] &:= \frac{0.5\,(v+29)}{1-\text{Exp}[-0.18\,(v+29)]} \\
\beta_m[v_] &:= 6\,\text{Exp}\left[-\frac{v+45}{15}\right] \\
\alpha_h[v_] &:= 0.15 * \text{Exp}\left[-\frac{v+47}{20}\right] \\
\beta_h[v_] &:= \frac{2.8}{1+\text{Exp}[-0.1\,(v+20)]} \\
\alpha_n[v_] &:= \frac{0.0065\,(v+30)}{1-\text{Exp}[-0.3\,(v+30)]} \\
\beta_n[v_] &:= 0.083\,\text{Exp}\left[-\frac{v+15}{15}\right],
\end{aligned} \tag{B.1}$$

where the exponential forms are merely conventional and of no particular significance for this document.

The corresponding steady-state values and time constants are defined

$$
\begin{aligned}
m_\infty[v\_] &:= \frac{\alpha_m[v]}{\alpha_m[v] + \beta_m[v]} \\
h_\infty[v\_] &:= \frac{\alpha_h[v]}{\alpha_h[v] + \beta_h[v]} \\
n_\infty[v\_] &:= \frac{\alpha_n[v]}{\alpha_n[v] + \beta_n[v]} \\
\tau_m[v\_] &:= \frac{1}{\alpha_m[v] + \beta_m[v]} \\
\tau_h[v\_] &:= \frac{1}{\alpha_h[v] + \beta_h[v]} \\
\tau_n[v\_] &:= \frac{1}{\alpha_n[v] + \beta_n[v]}
\end{aligned}
\tag{B.2}
$$

and are plotted as functions of voltage with the commands

```
Plot[Evaluate[{m∞[v], h∞[v], n∞[v]}],
 {v, -150, 150}, PlotRange → All]

Plot[Evaluate[{τn[v], τm[v], τh[v]}],
 {v, -150, 150}, PlotRange → All]
```

to aid in visualization of the properties of the constants. These plots are shown in Fig. B.1 and B.2. (The significance of these figures is discussed in Chapter 2.) The electical constants are defined

$$
\begin{aligned}
&\bar{g}_{Na} = 150 \\
&\bar{g}_{K} = 90 \\
&g_{leak} = 0.25 \\
&c = 1 \\
&\mathcal{E}_{Na} = 75 \\
&\mathcal{E}_{K} = -85 \\
&\mathcal{E}_{leak} = -70 \\
&g_{Na}[t\_] = \bar{g}_{Na}\, m[t]^3\, h[t] \\
&g_{K}[t\_] = \bar{g}_{K}\, n[t]^4 ,
\end{aligned}
\tag{B.3}
$$

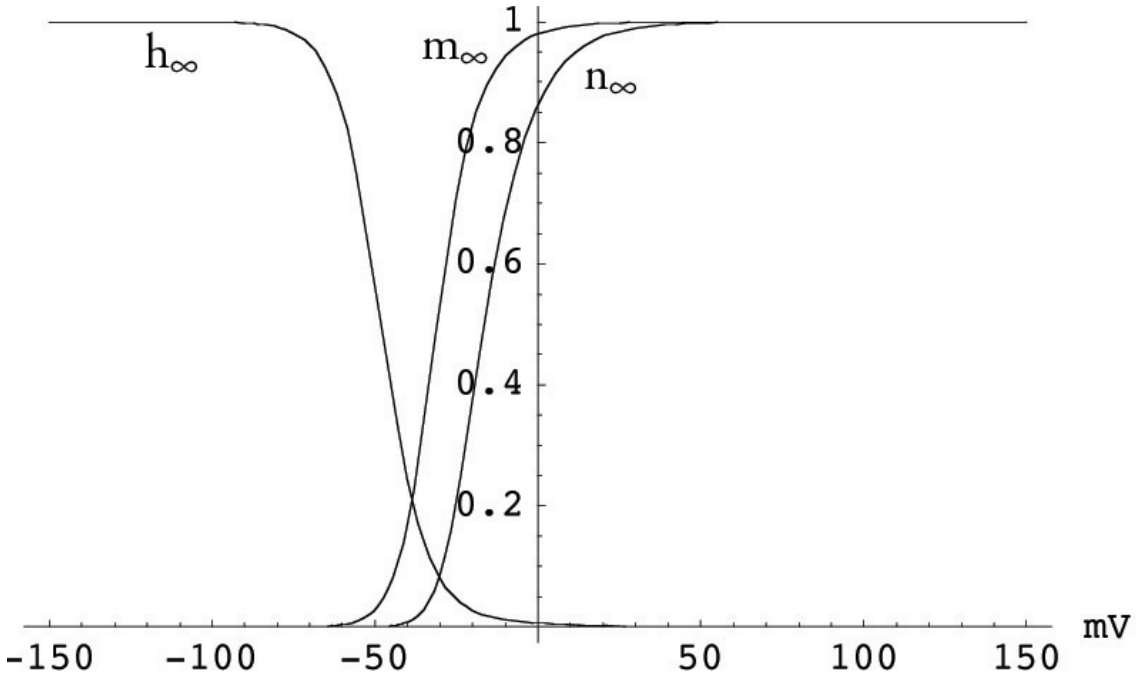

FIG. B.1: *Mathematica* plot of HH steady-state values vs. membrane voltage.

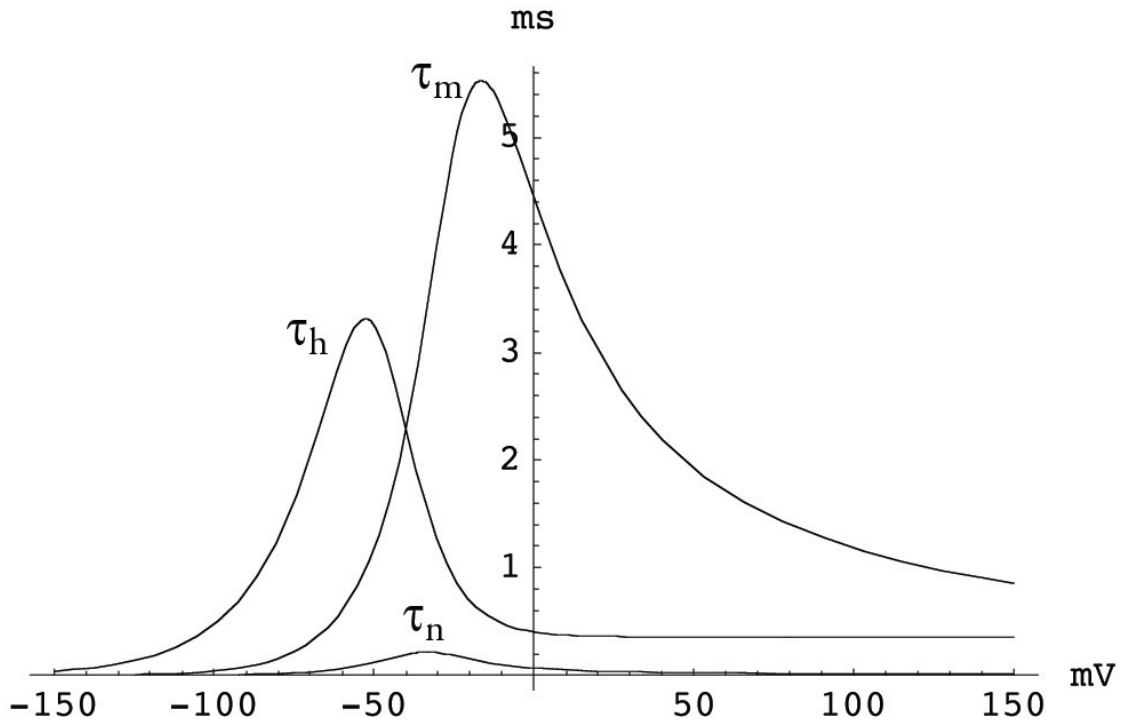

FIG. B.2: *Mathematica* plot of HH time constants vs. membrane voltage.

where the electromotive forces $\mathcal{E}$ are in mV, the conductances g are in nS, and the capacitance c is in pF.

In order to solve the HH equations numerically, *Mathematica* requires initial conditions for each of the variables. The equations and initial conditions are entered into the program in the following form:

```
initial :=
 {v[0] == 0, m[0] == m∞[0], n[0] == n∞[0], h[0] == h∞[0]}

diffeqs := {m'[t] == αm[v[t]] (1 - m[t]) - βm[v[t]] m[t],
  n'[t] == αn[v[t]] (1 - n[t]) - βn [v[t]] n[t],
  h'[t] == αh[v[t]] (1 - h[t]) - βh[v[t]] h[t],
  c v'[t] + gNa[t] (v[t] - ℰNa) +
    gK[t] (v[t] - ℰK) + gleak (v[t] - ℰleak) == i[t]} .
```

(B.4)

Here, ′ denotes the time derivative.

To construct the injected current, a list of numbers that describes the transformed edge velocity (see Chapter 5) is pasted into *Mathematica* from *Igor*:

```
Velocity := {0, 0, 0, 0, 0, 0, 0, 0, 0, 0, 0, 0, 0, 0, 0, 0,
  0, 0, 0, 0, 0, 0, 0, 0, 0, 0, 0, 0, 0, 0, 0, 0, 0, 0, 0,
  0, 0, 0, 0, 0, 0, 0, 0, 0, 0, 0, 0, 0, 0, 0, 0, 0, 0, 0,
  0, 0, 0, 1, 1, 2, -2, -2, -1, 0, -1, -1, -2, 2, 2, 1,
  1, 0, -1, -1, -2, -2, -2, -1.99113, 3, 3, 2, 1, 1, 0,
  0, 0, 0, 1, 2, 2, 1, 1, 1, 2, 3, -3, -2, -2, -1, -1,
  -1, -1, -1, -2, -2, 2, 1, 0, -1, -1, -1, 0, -1, -1,
  -2, 3, 4, 4, 4, 4, 3, 3, 2.97015, 2.88237, 2.74179,
  2.55643, 2.3364, 1.45069, 1.33915, 1.75213, 1.05458,
  0.943684, 0.836973, 0.735759, 0.641061, 0.553609,
  0.473856, 0.553559, 0.422575, -0.553559, -0.436938,
  -0.512752, -0.596395, -0.687543, -0.785608,
  -0.889716, -0.471842, -0.499352, -0.527292,
  0.943684, 0.444858, 0.418486, -0.444858, -0.471842,
  -1.05458, -1.83788, -2.90137, -3.3152, 2.90137,
  2.92022, 1.88737, 1.47152, 1.28188, 0.845067, etc ...}.
```

The velocity is then coupled with the the corresponding time in milliseconds using a `For`

loop:

```
For[index = 1, index < 1500, index++, cv =
  Union[cv, {{11.78 (index), If[Velocity[[index + 1]] > 0,
       5, 0.05] * Velocity[[index + 1]]}}]].
```

The 11.78 multiplier corresponds to the refresh rate of the monitor. This refresh rate was clocked at 84.9 Hz; therefore, the screen was updated every 11.78 ms. The `If` statement found within the loop scales positive velocities up by a factor of 5 and negative velocities down by a factor of 0.05, since it was noticed that the DS cells responded more strongly to excitatory signals than to inhibitory signals. *Mathematica*'s interpolation function is used to turn this list into a continuous function, which is graphed as a function of time:

```
i = Interpolation[cv, InterpolationOrder → 1]

Plot[i[t], {t, 0, 17658}, PlotRange → All] .
```

The resulting plot is shown in Fig. B.3.

Once `i[t]` is defined, the HH equations are solved numerically, and the potential is plotted as a function of time to reveal the spike train:

```
solution = NDSolve[{initial, diffeqs},
  {v, m, n, h}, {t, 0, 17600}, MaxSteps → 400000]

Plot[Evaluate[{v[t]} /. solution], {t, 0, 17600},
 {PlotRange → All, AxesLabel → {ms, AU}, AxesOrigin → -70}].
```

The plot can be seen in Fig. B.4.

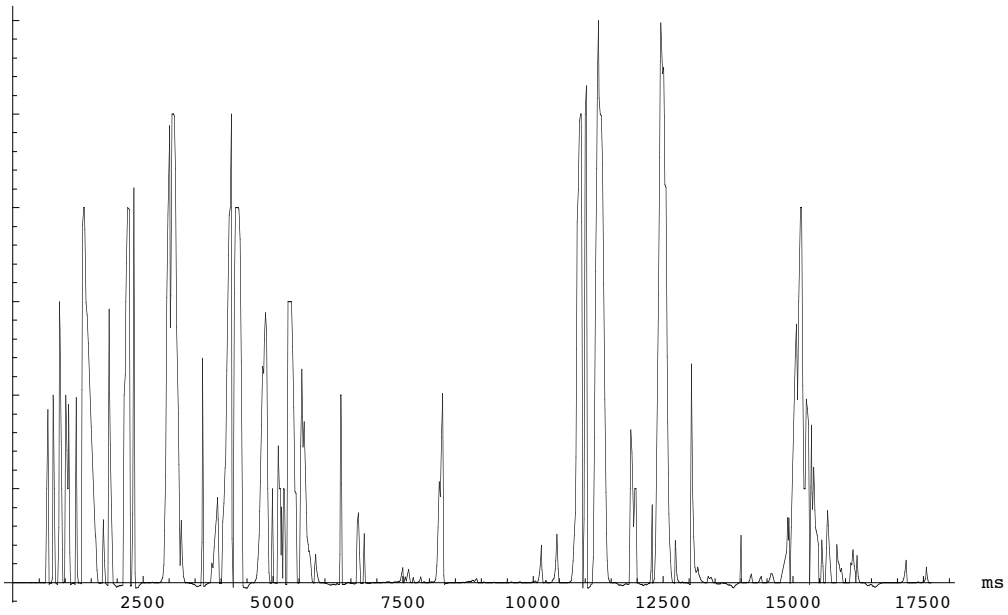

FIG. B.3: Simulated injected current as a function of time. The current is created by interpolating an altered form of the edge velocity.

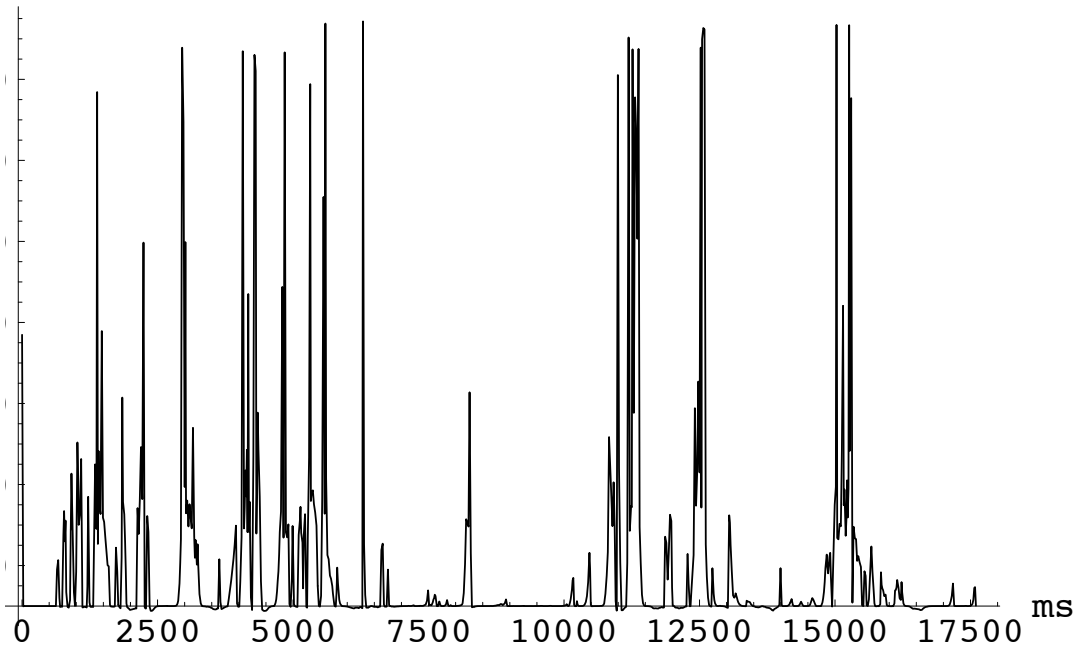

FIG. B.4: Membrane potential plotted as a function of time. This spike train represents the solution to the HH equations for the given membrane current.

Appendix C

Data Sets

Data for each trial referenced throughout Chapter 5 is contained here. Each data set consists of the stimulus velocity for the trial and the spike train or intracellular record that was produced. The caption below each set of graphs contains the reference number for that trial.

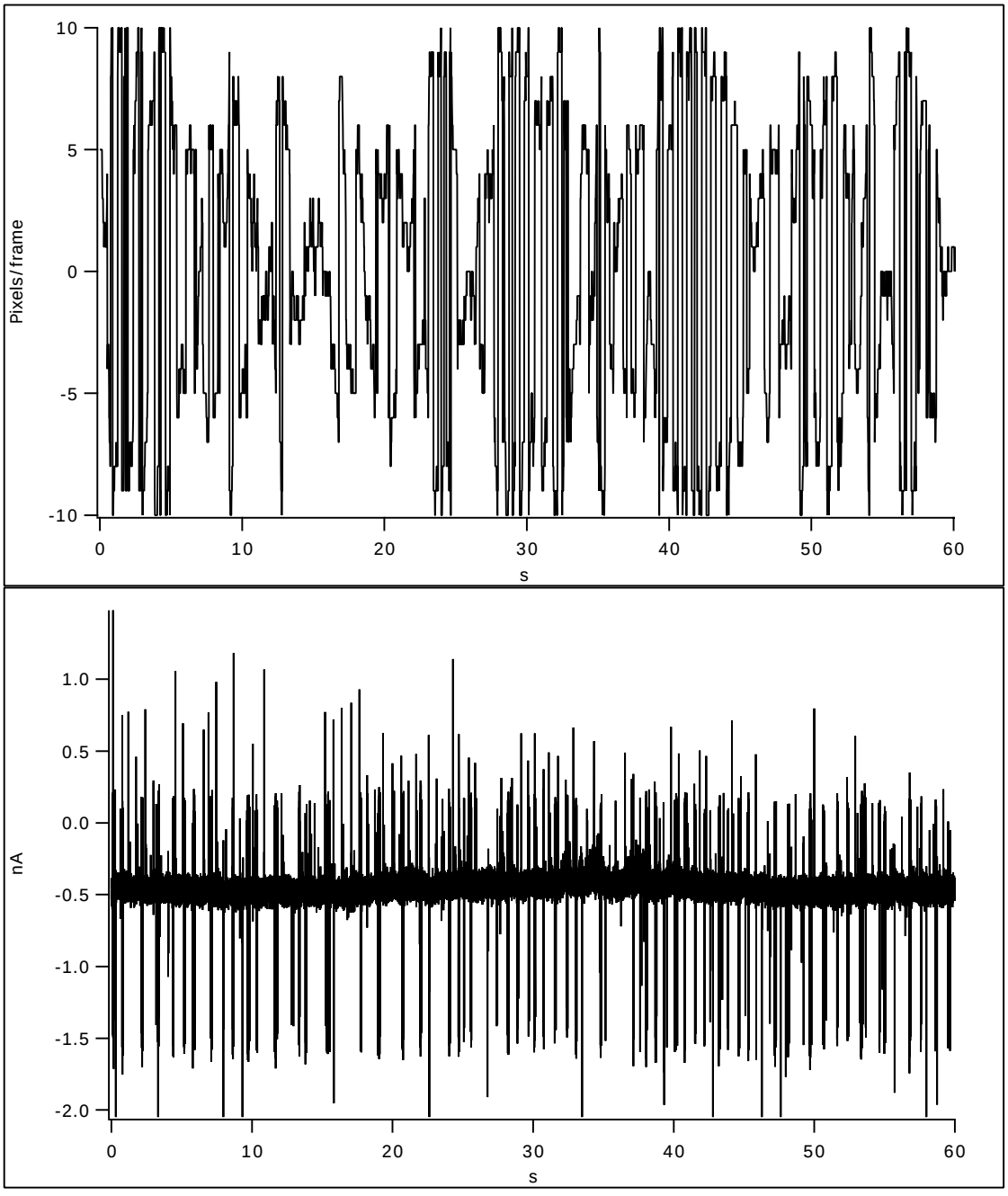

FIG. C.1: Stimulus velocity (*top*) and spike train (*bottom*) for trial 1-57.

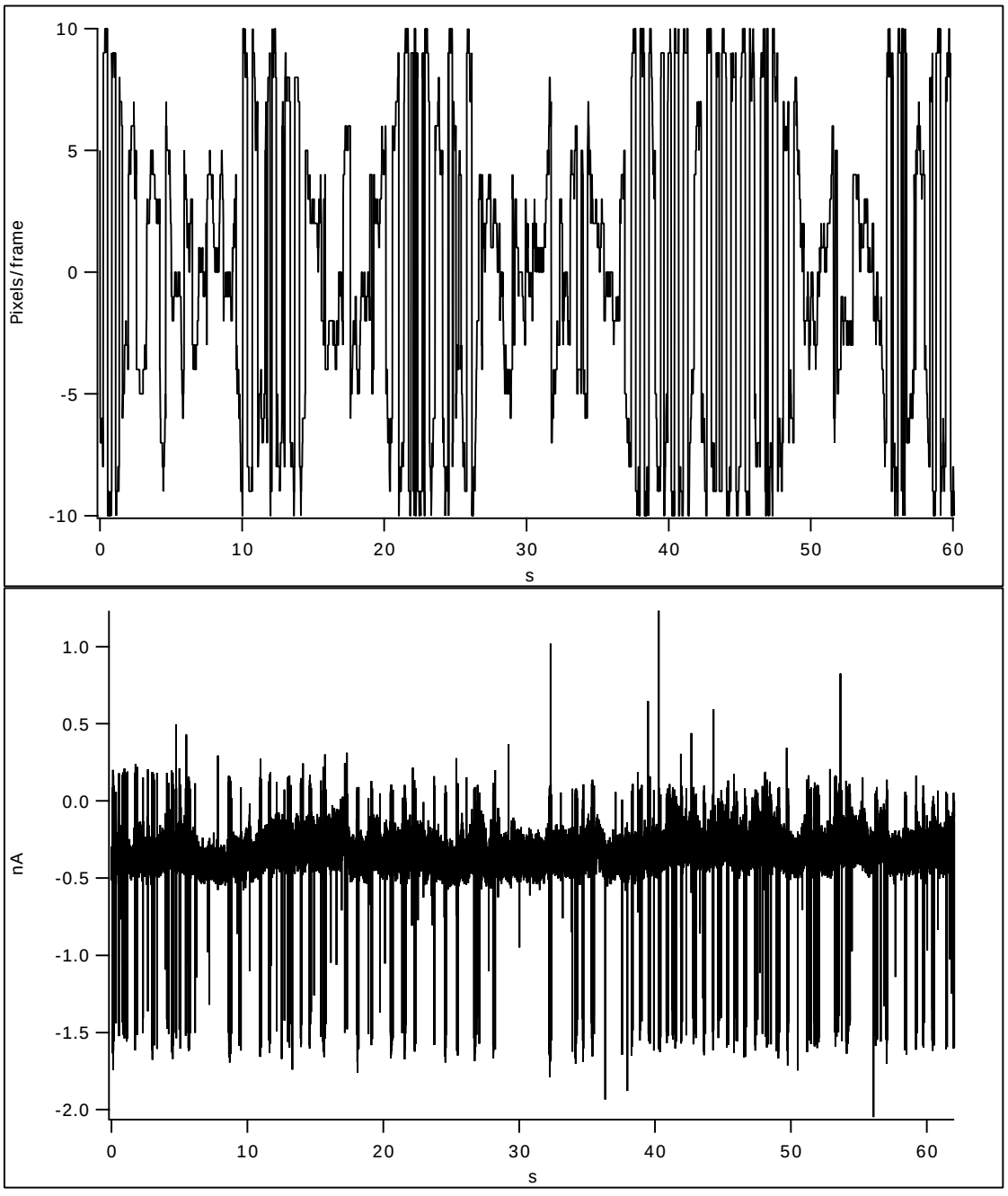

FIG. C.2: Stimulus velocity (*top*) and spike train (*bottom*) for trial 1-58.

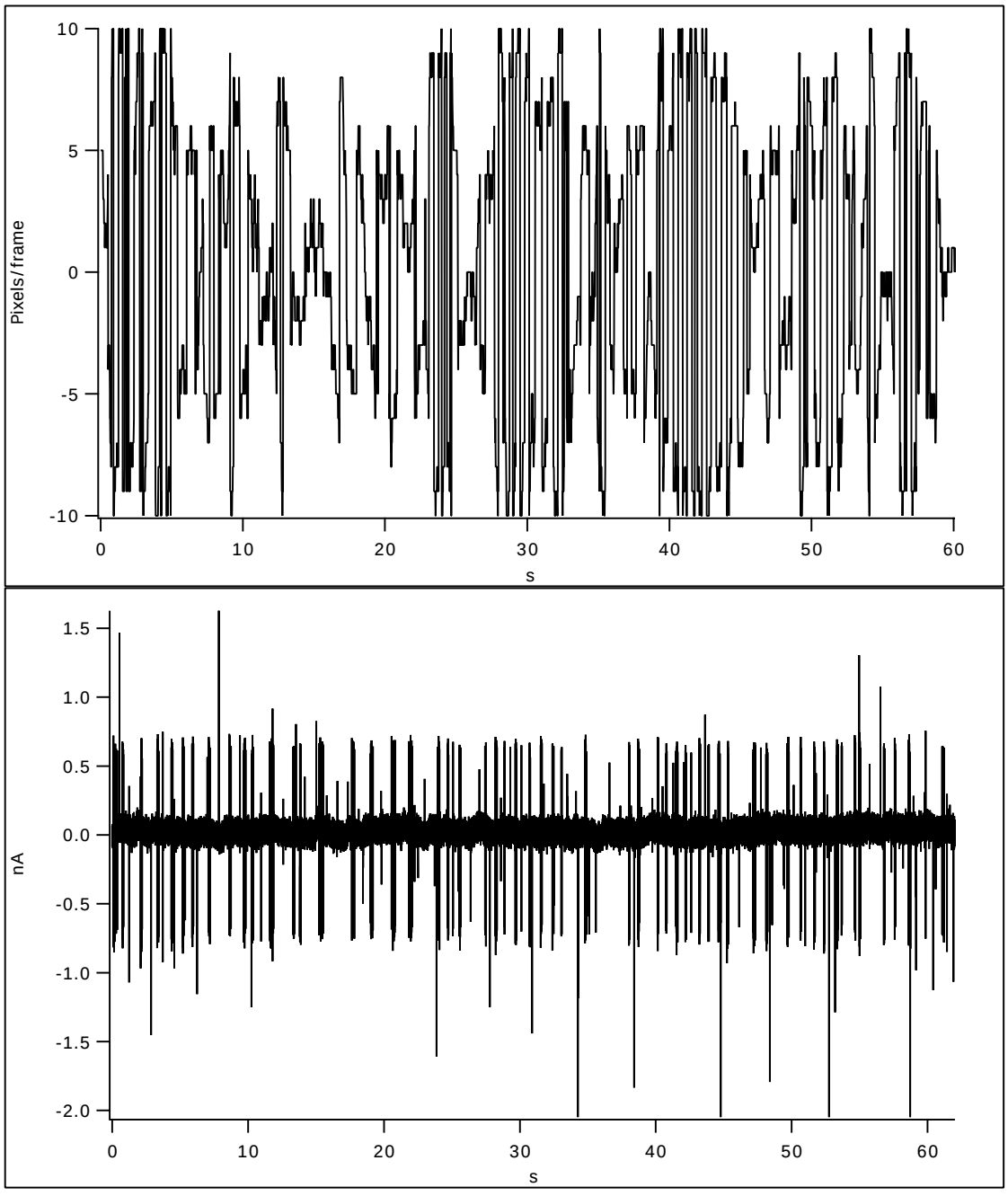

FIG. C.3: Stimulus velocity (*top*) and spike train (*bottom*) for trial 1-73.

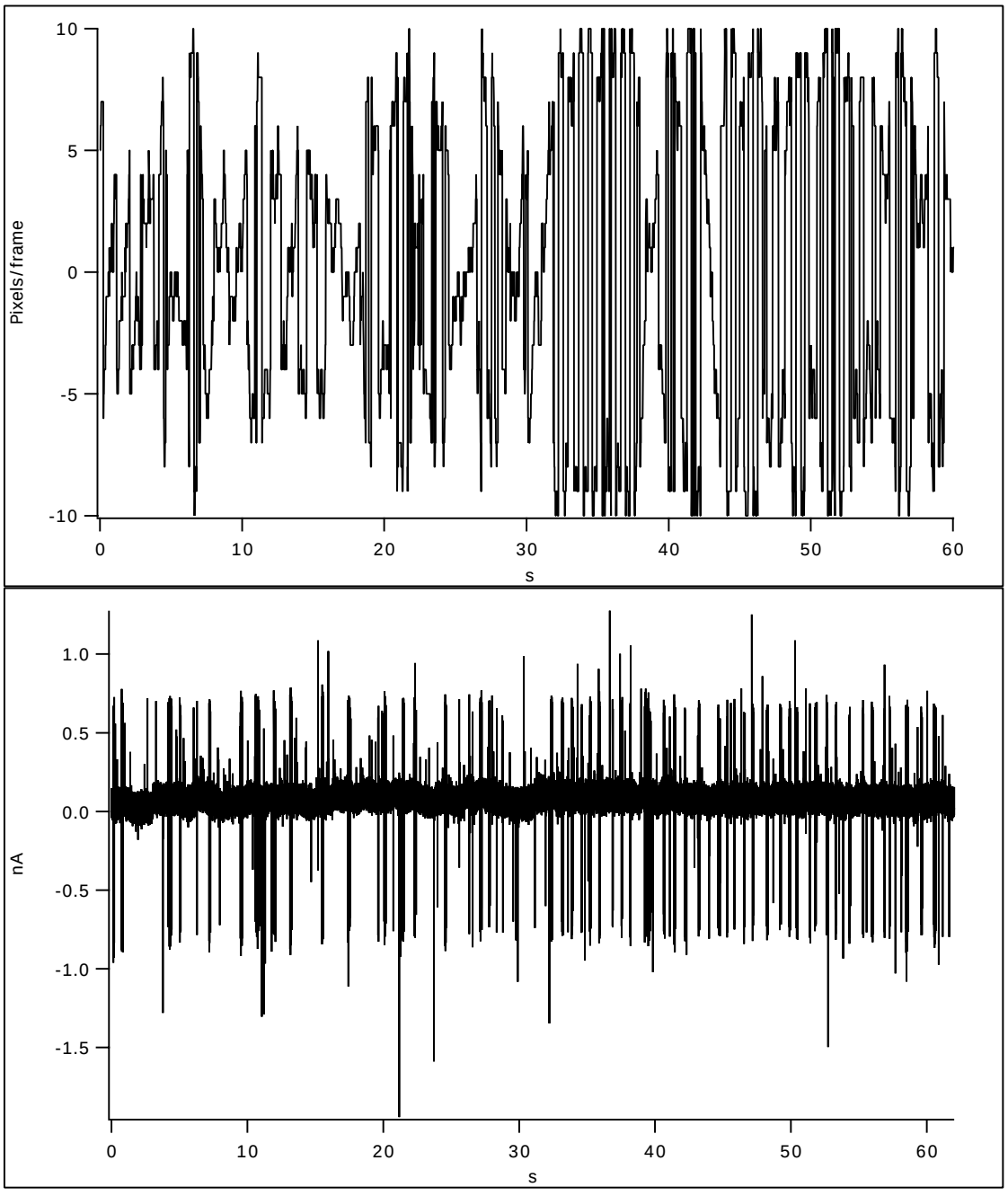

FIG. C.4: Stimulus velocity (*top*) and spike train (*bottom*) for trial 1-75.

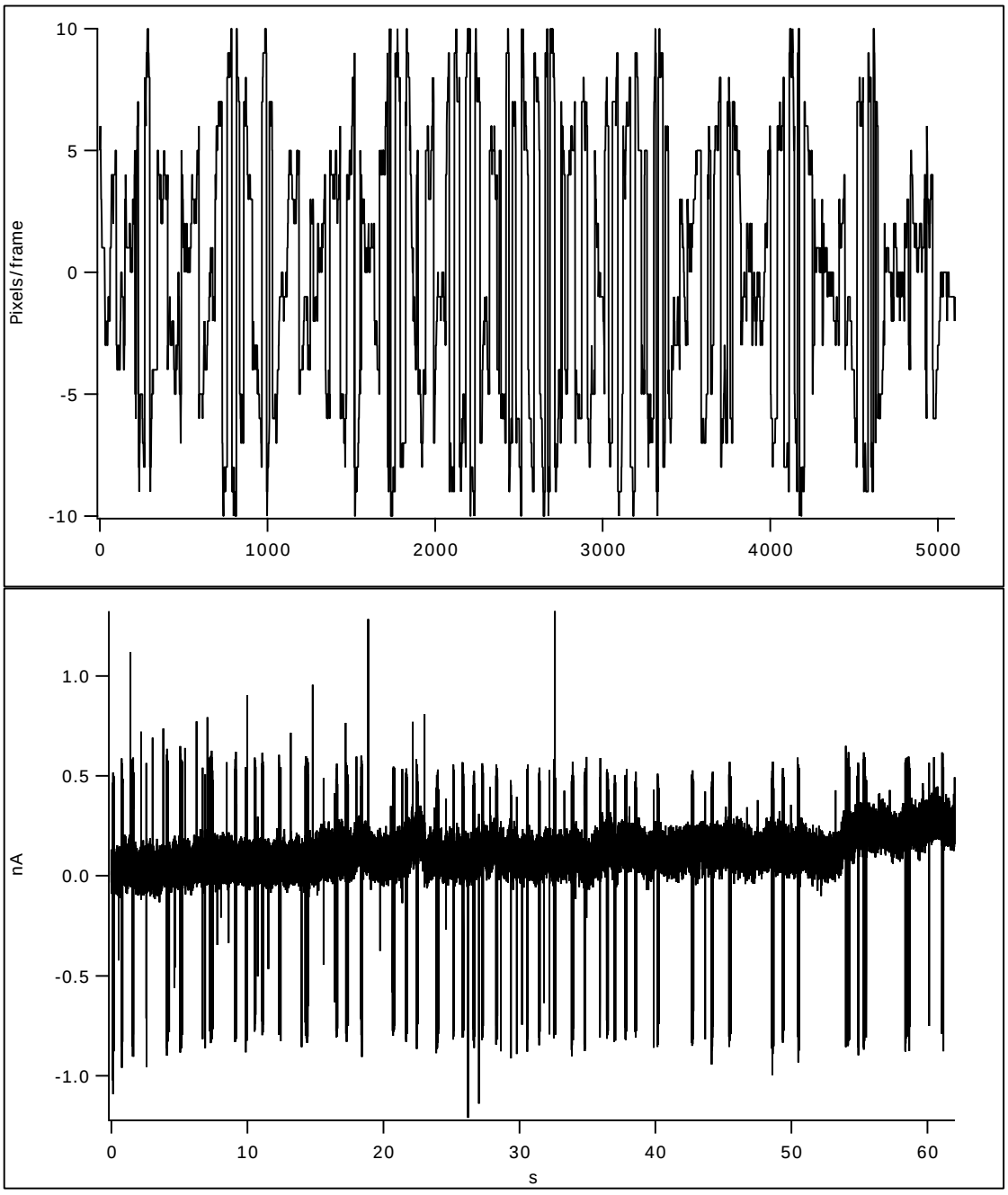

FIG. C.5: Stimulus velocity (*top*) and spike train (*bottom*) for trial 1-77.

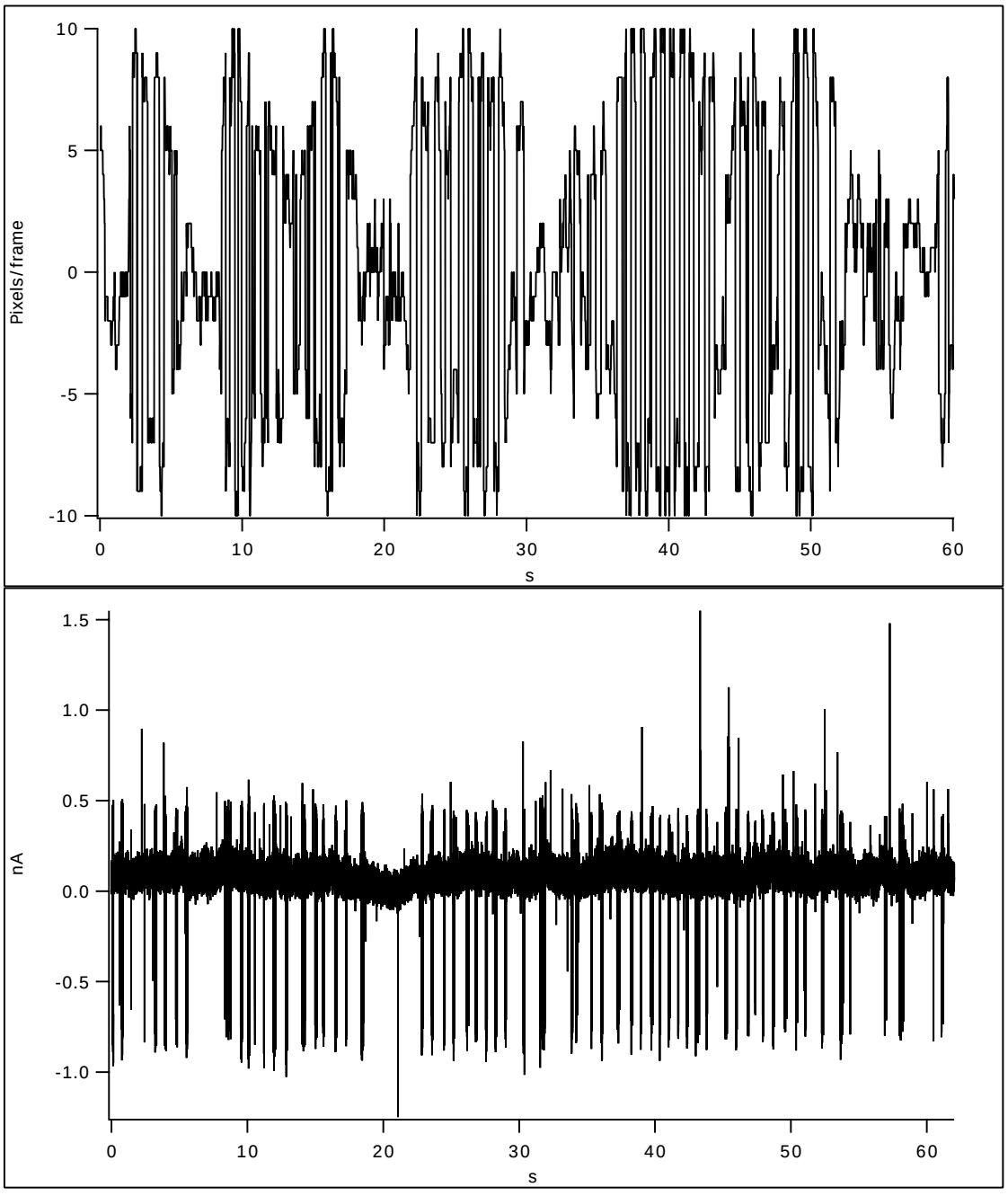

FIG. C.6: Stimulus velocity (*top*) and spike train (*bottom*) for trial 1-81.

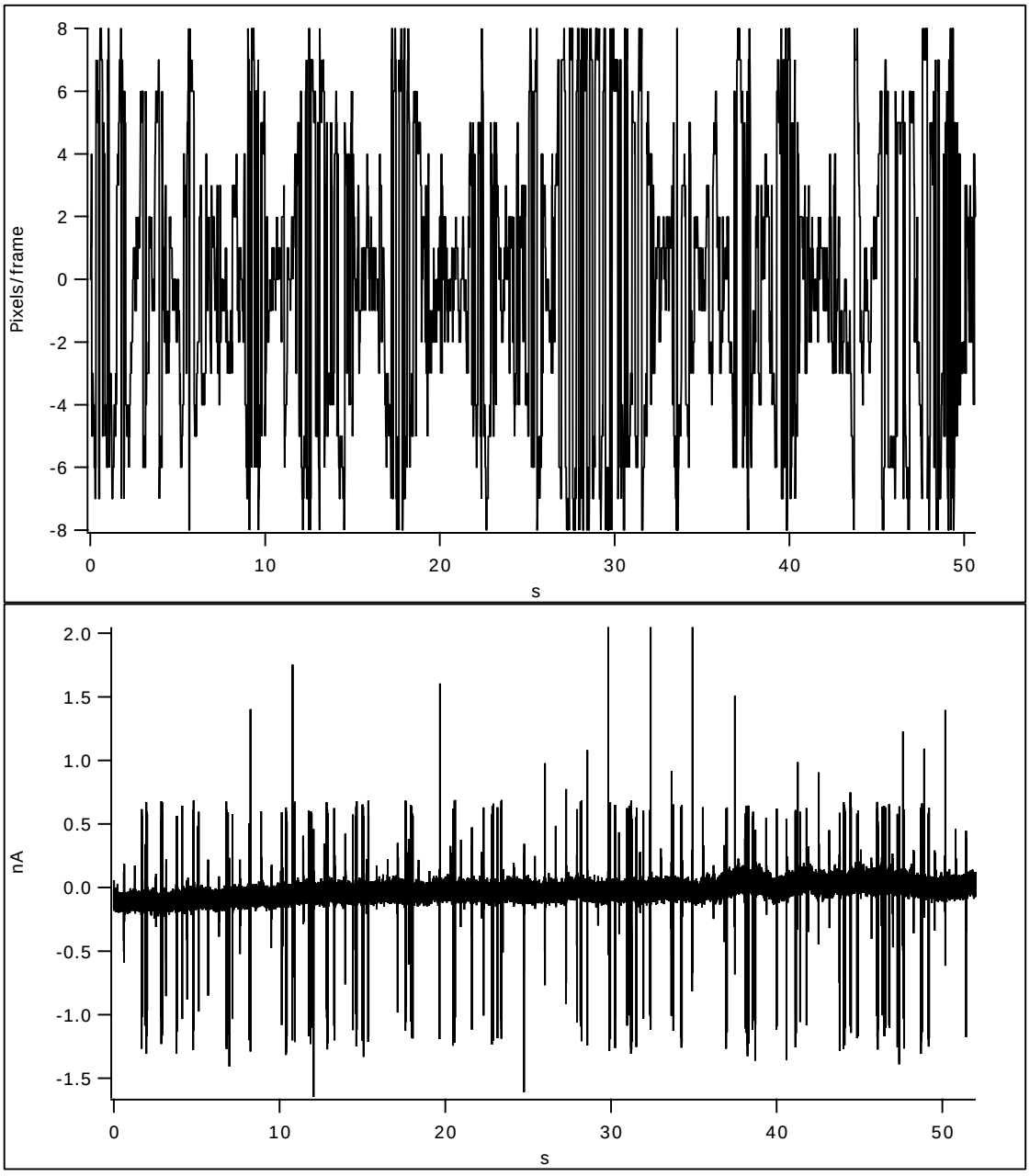

FIG. C.7: Stimulus velocity (*top*) and spike train (*bottom*) for trial 2-55.

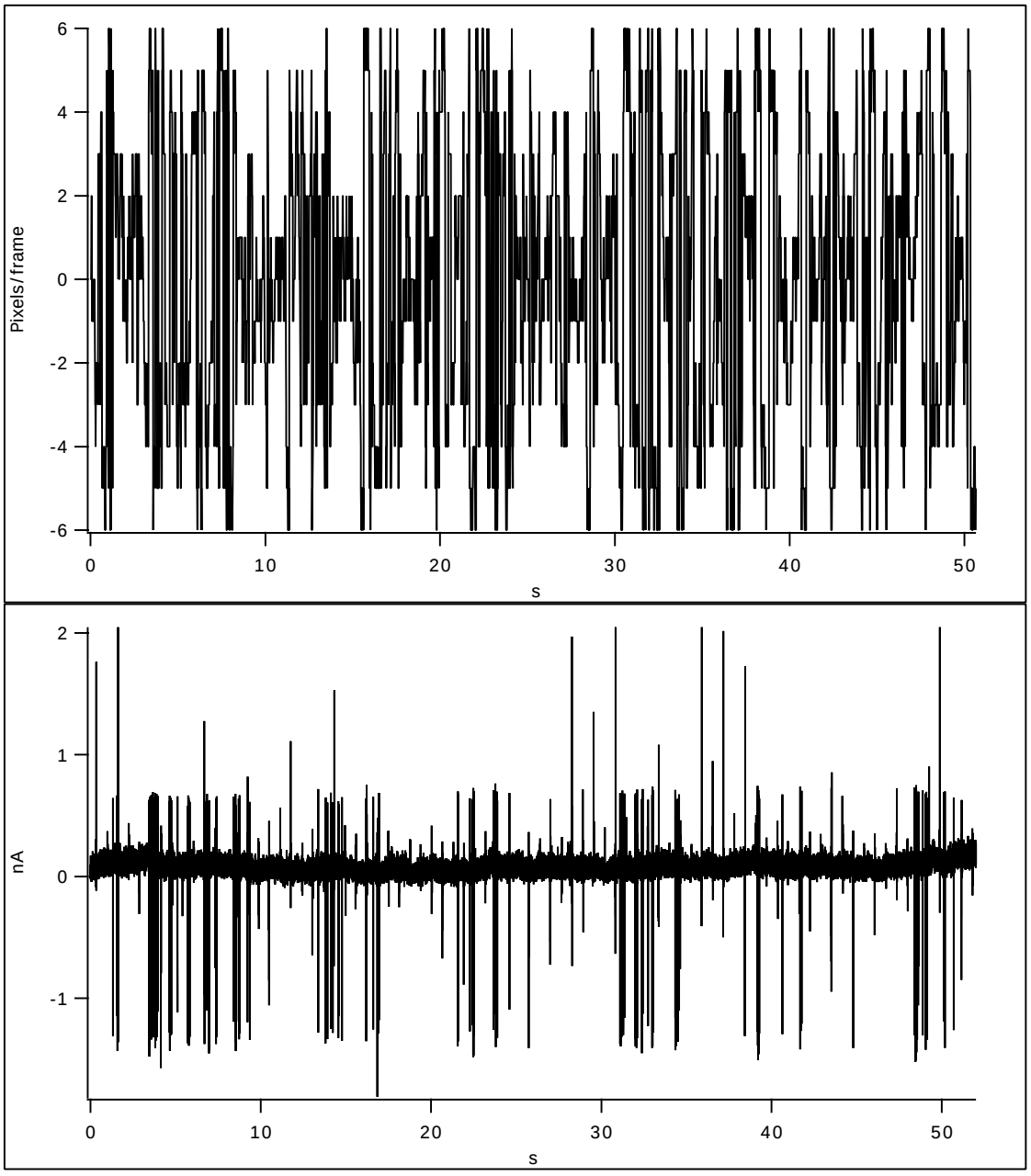

FIG. C.8: Stimulus velocity (*top*) and spike train (*bottom*) for trial 2-57.

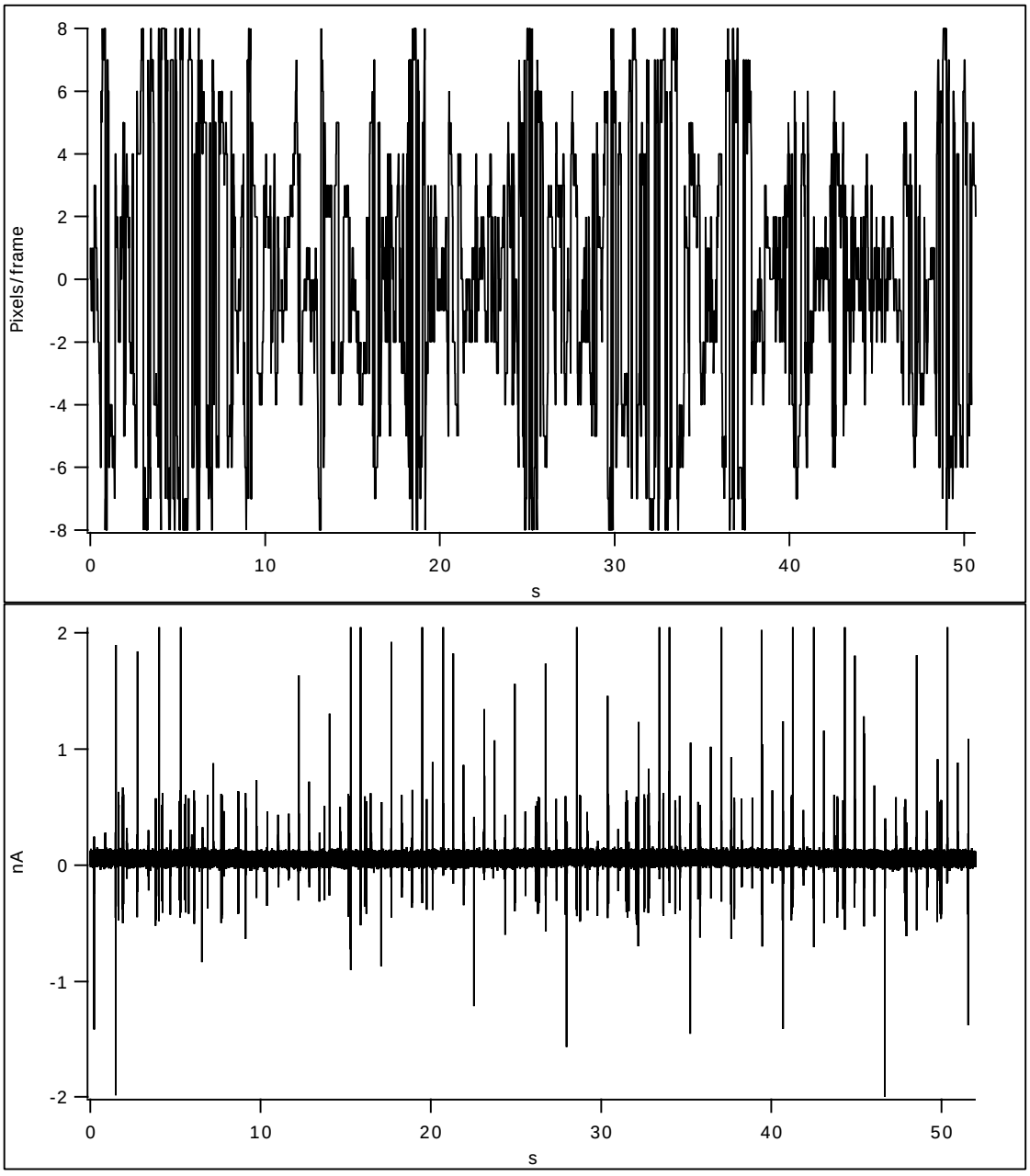

FIG. C.9: Stimulus velocity (*top*) and spike train (*bottom*) for trial 2-61.

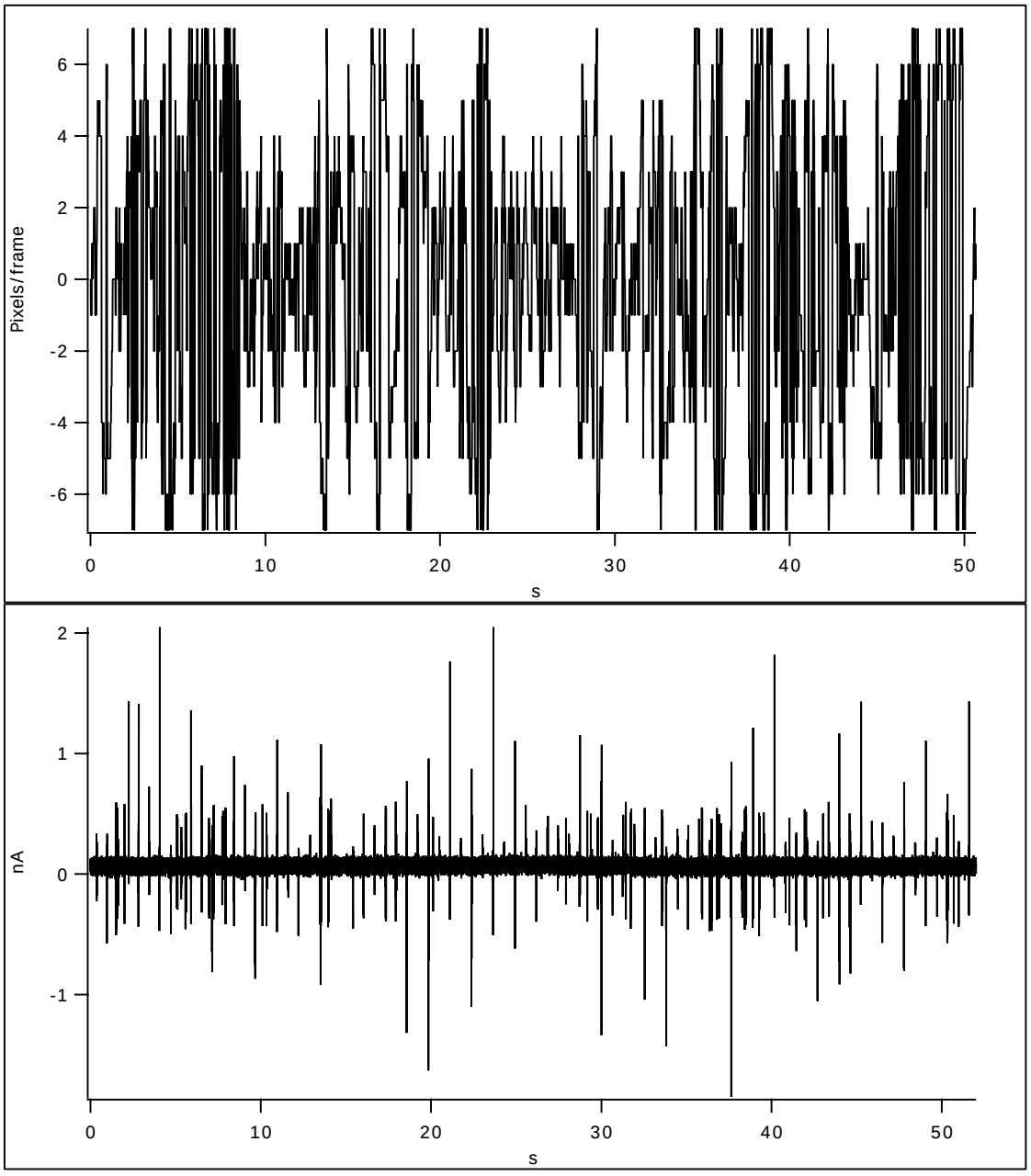

FIG. C.10: Stimulus velocity (*top*) and spike train (*bottom*) for trial 2-63.

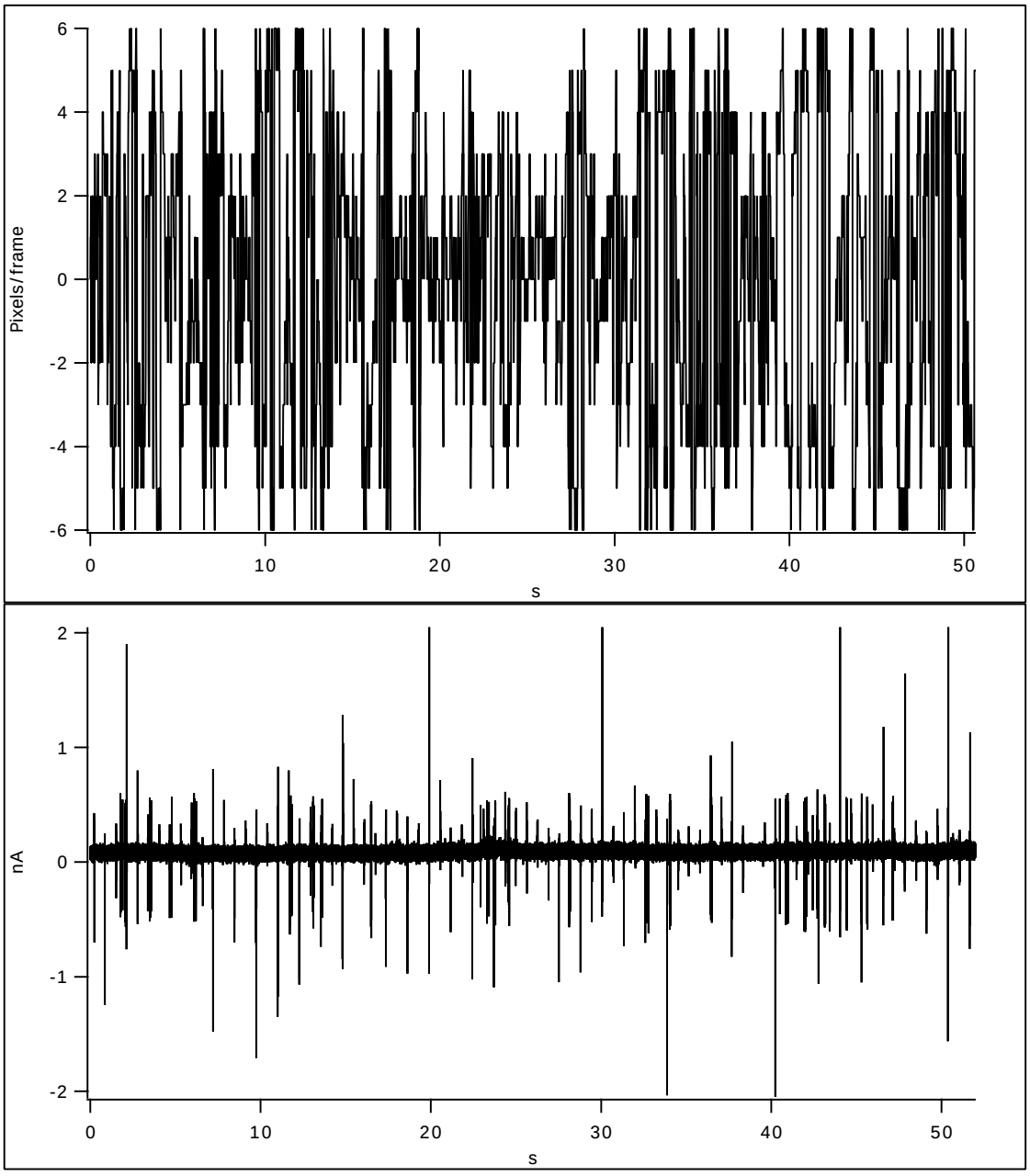

FIG. C.11: Stimulus velocity (*top*) and spike train (*bottom*) for trial 2-65.

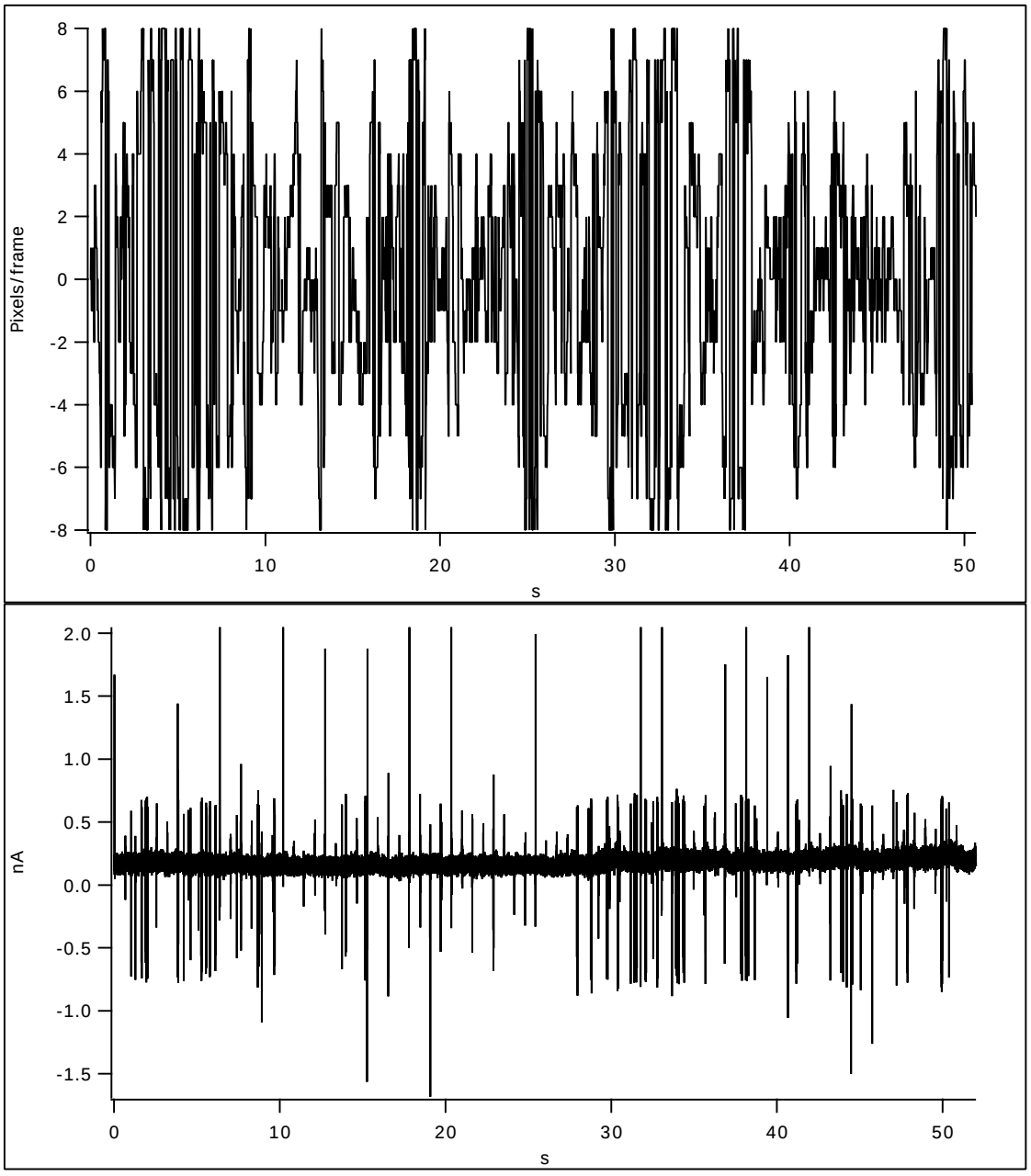

FIG. C.12: Stimulus velocity (*top*) and spike train (*bottom*) for trial 2-61a.

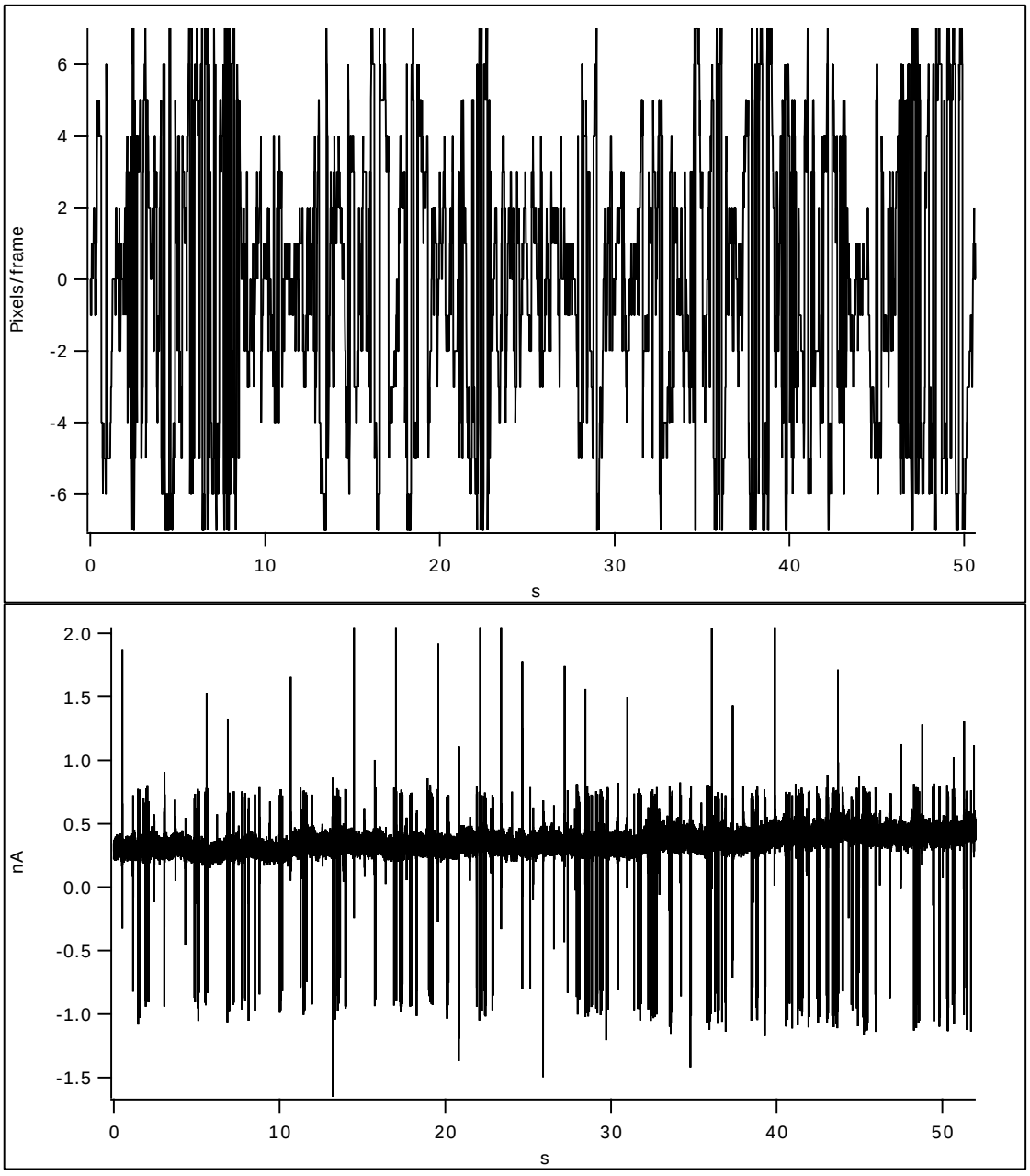

FIG. C.13: Stimulus velocity (*top*) and spike train (*bottom*) for trial 2-63a.

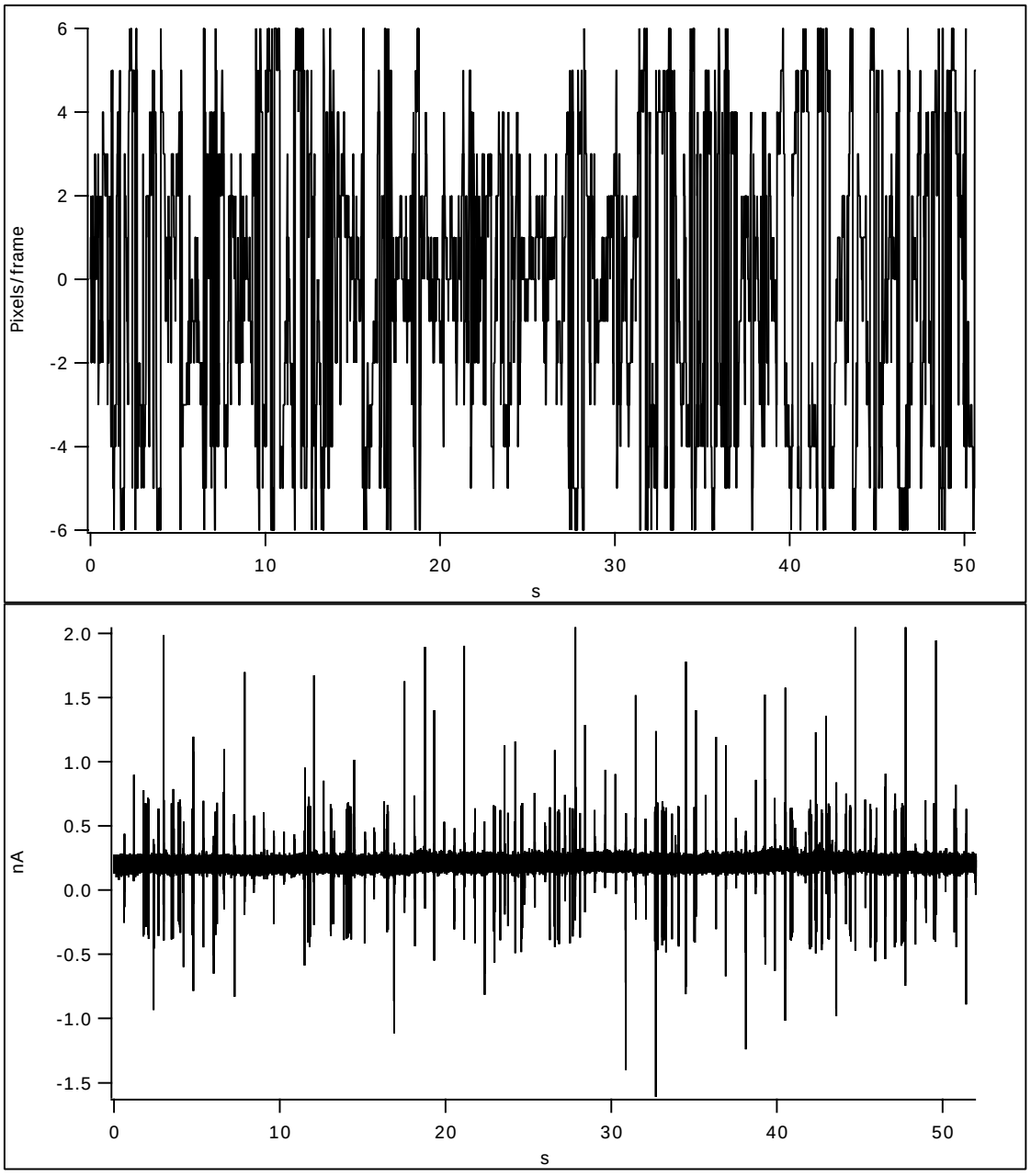

FIG. C.14: Stimulus velocity (*top*) and spike train (*bottom*) for trial 2-66.

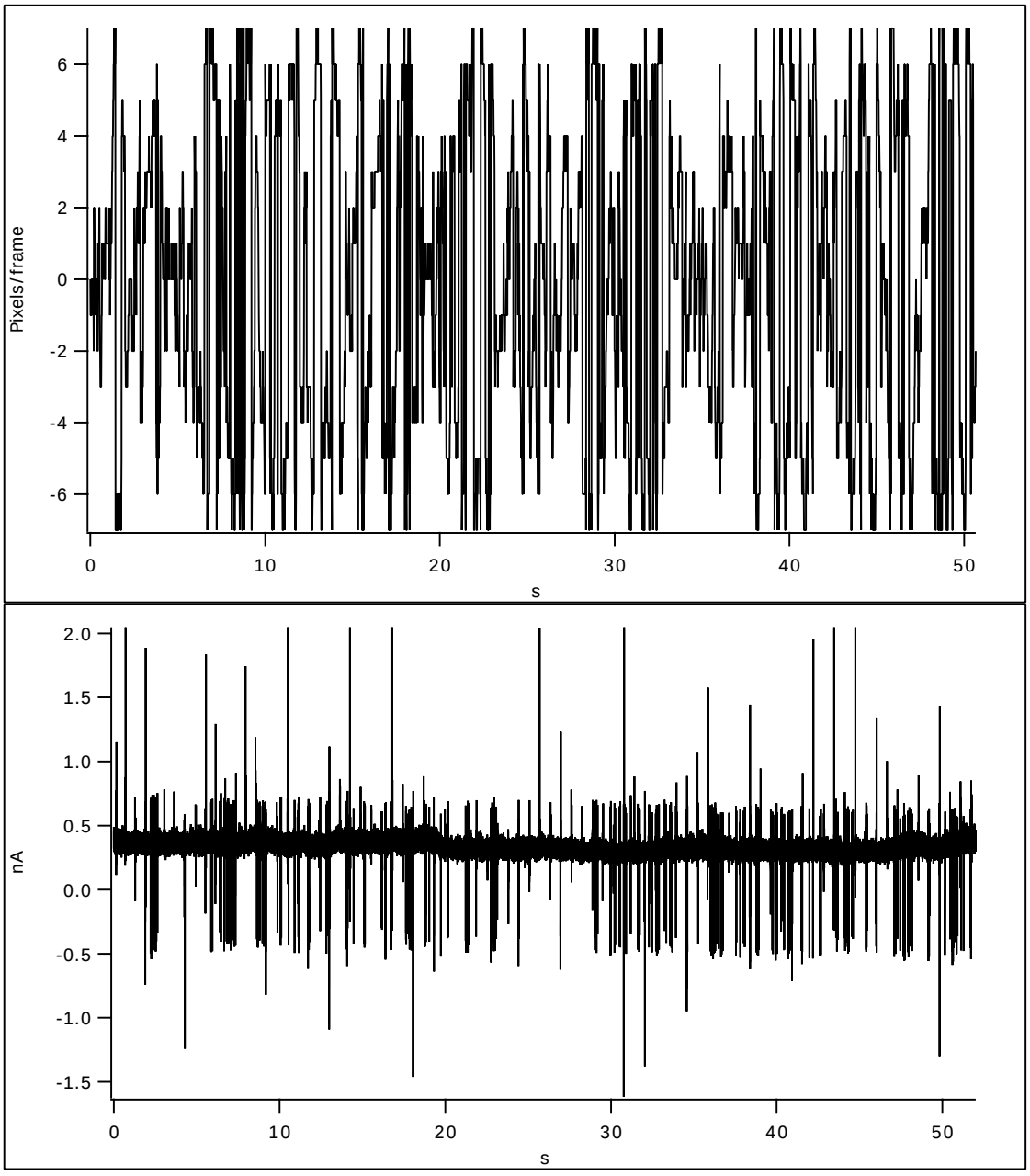

FIG. C.15: Stimulus velocity (*top*) and spike train (*bottom*) for trial 2-68.

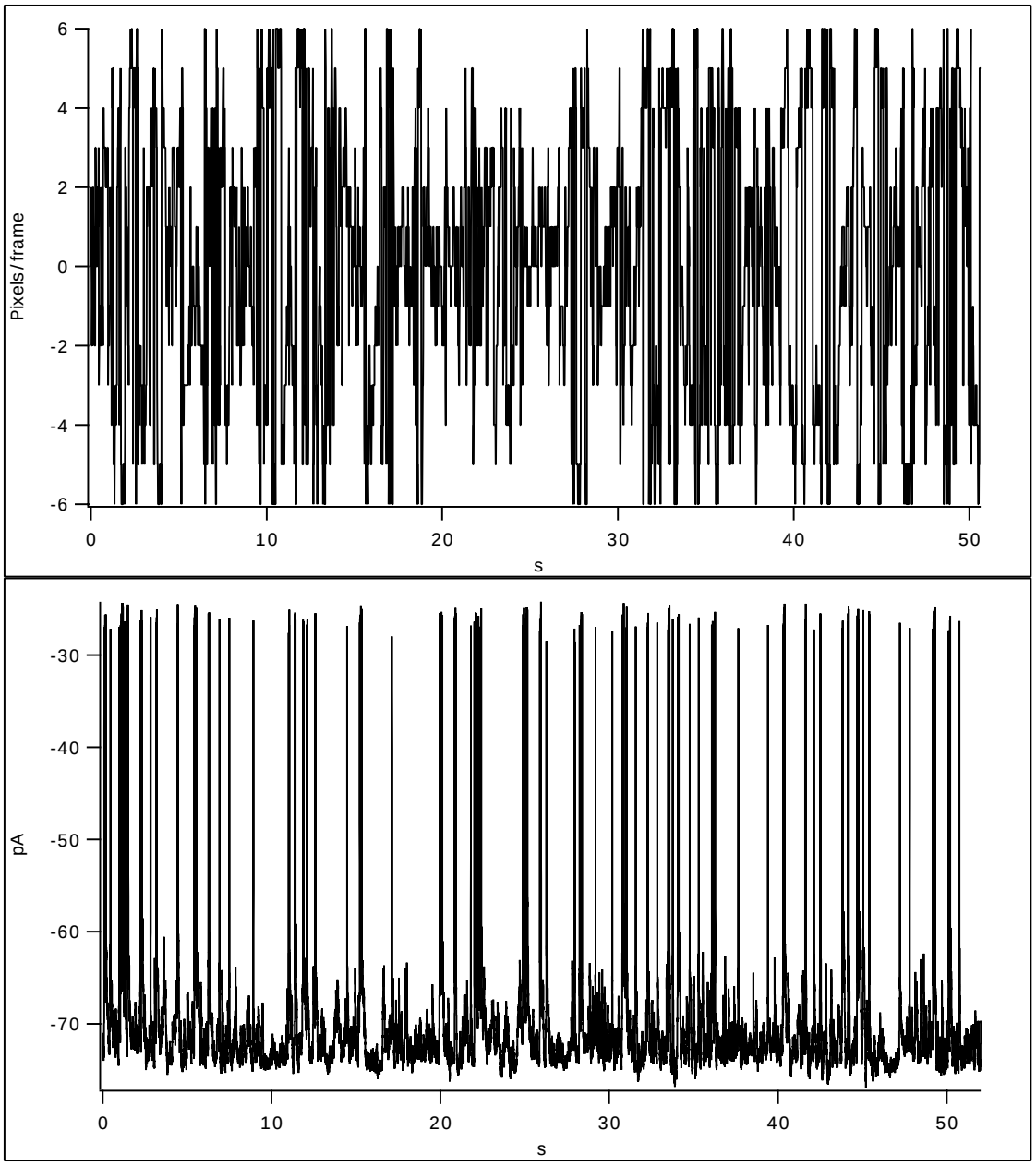

FIG. C.16: Stimulus velocity (*top*) and intracellular current record (*bottom*) for trial 2-159.

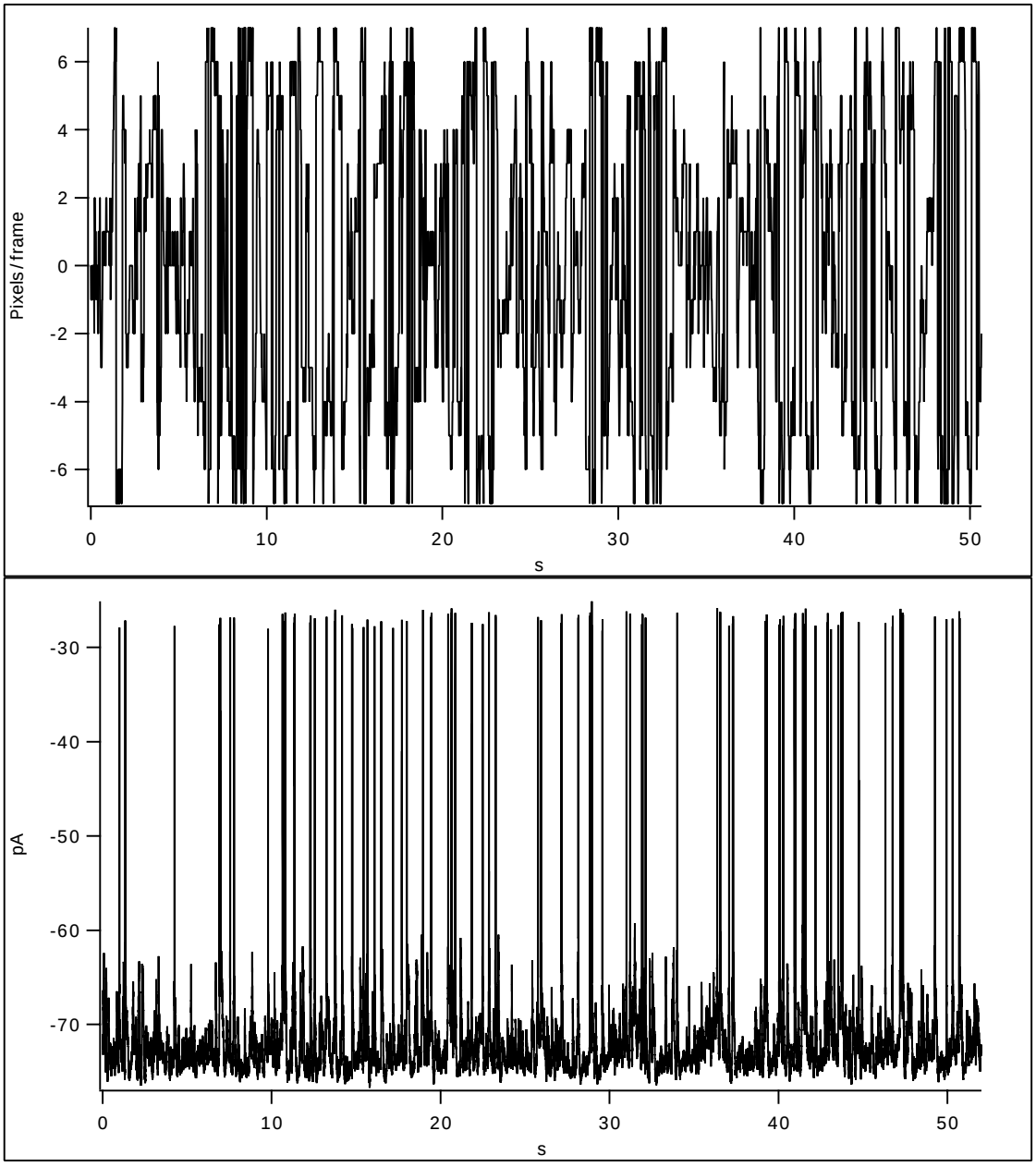

FIG. C.17: Stimulus velocity (*top*) and intracellular current record (*bottom*) for trial 2-160.

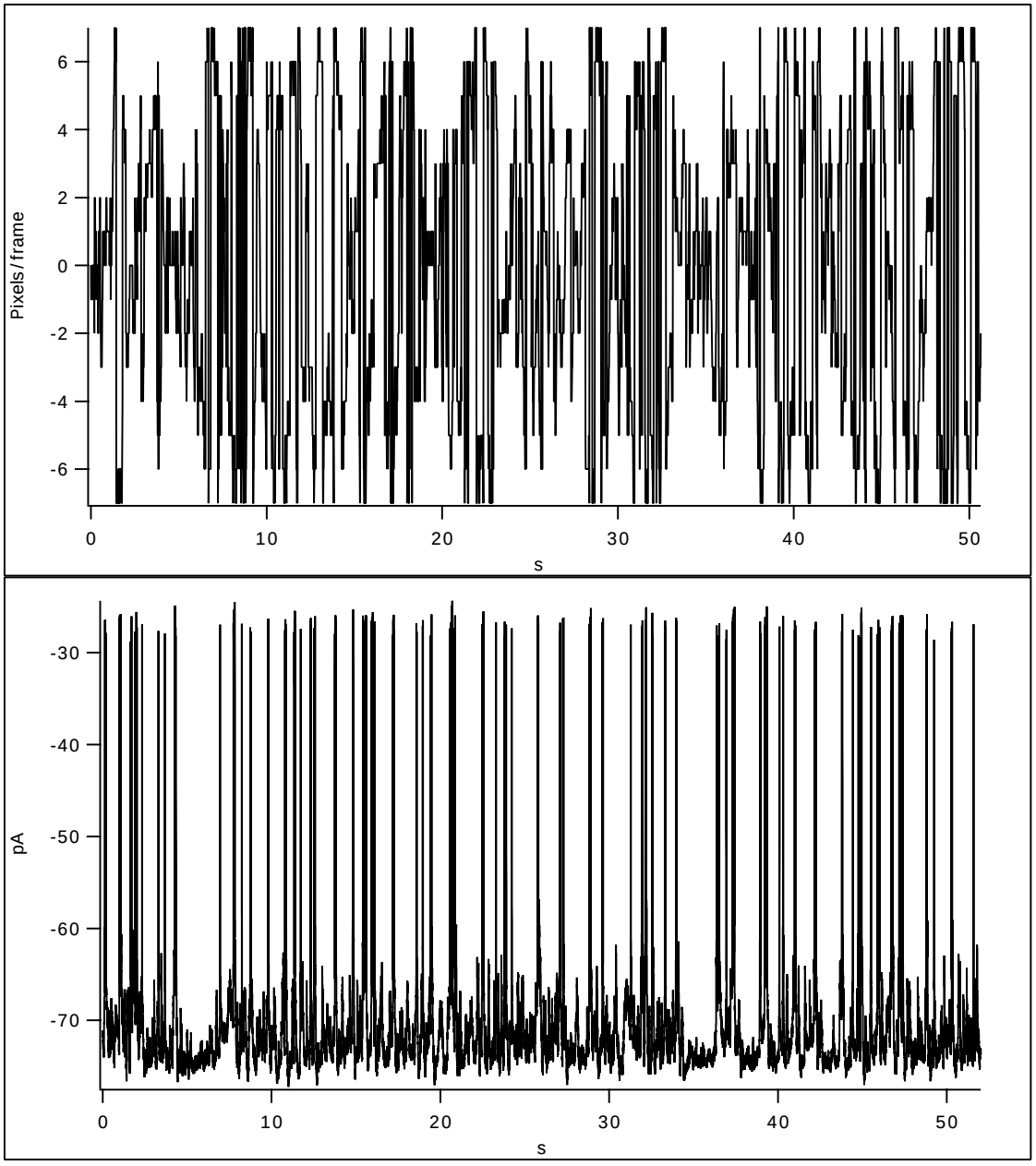

FIG. C.18: Stimulus velocity (*top*) and intracellular current record (*bottom*) for trial 2-161.

References

[1] Herodotus, *The Histories* (Penguin Books, New York, 1996).

[2] S. Finger, *Origins of Neuroscience: A History of Explorations into Brain Function* (Oxford Univ. Press, New York, 2001).

[3] R. P. Feynman, R. B. Leighton, and M. Sands, *Mainly Mechanics, Radiation, and Heat*, The Feynman Lectures on Physics Vol. 1 (Addison-Wesley Pub. Co., Reading, MA, 1963), chap. 3.

[4] M. Plischke and B. Bergersen, *Equilibrium Statistical Physics* (Scientific Pub., River Edge, NJ, 1994).

[5] E. Kandel, J. Schwartz, and T. Jessel, editors, *Principles of Neural Science* (McGraw-Hill, New York, 2000), chap. 2.

[6] B. Hille, *Ionic Channels of Excitable Membranes* (Sinauer Associates, Inc., Sunderland, MA, 1992).

[7] S. R. y Cajal, *Neuron Theory or Reticular Theory: Objective Evidence of the Anatomical Unity of Nerve Cells* (Consejo Superior de Investigaciones Cientificas, Madrid, 1954).

[8] L. Galvani, *De Biribus Electricitatus in Moto Musculari, Commentrius* (Typographia Instituti Scientarum, Bologna, 1791).

[9] M. W. Cowan and E. R. Kandel, A brief history of synapses and synaptic transmission, in *Synapses*, Johns Hopkins Univ. Press, Baltimore, 2001.

[10] http://chem.ch.huji.ac.il/ eugeniik/history/nobili.html.

[11] E. Kandel, J. Schwartz, and T. Jessel, editors, *Principles of Neural Science* (McGraw-Hill, New York, 2000), chap. 26.

[12] D. I. Vaney, S. He, W. R. Taylor, and W. R. Levick, Direction-selective ganglion cells in the retina, in *Motion Vision - Computational, Neural, and Ecological Restraints*, Springer Verlag, New York, 2001.

[13] G. Yang and R. H. Masland, J. Neurosci. **14**, 5267 (1994).

[14] H. B. Barlow and W. R. Levick, J. Physiol. **178**, 477 (1965).

[15] D. Warland, P. Reinagel, and M. Meister, J. Neurophysiol **78**, 2336 (1997).

[16] B. A. y Arcas and A. L. Fairhall, Neural Computation **15**, 1789 (2003).

[17] A. L. Hodgkin and A. F. Huxley, J. Physiol. (Lond.) **117**, 500 (1952).

[18] T. F. Weiss, *Electrical Properties*, Cellular Biophysics Vol. 2 (MIT Press, Cambridge, MA, 1996).

[19] L. Hermann, *Lehrbuch der Physiologie* (A. Hirschwild, Berlin, 1905).

[20] M. Planck, *The Theory of Heat Radiation* (Dover Publications, Inc., New York, 1991).

[21] W. Nernst, Z. Phys. Chem. **2**, 613 (1888).

[22] K. S. Cole, *Membranes, Ions, and Impulses: A Chapter of Classical Biophysics* (Univ. of California Press, Berkley, 1968).

[23] K. S. Cole and H. J. Curtis, J. Gen. Physiol. **22**, 649 (1939).

[24] A. L. Hodgkin and A. F. Huxley, J. Physiol. (Lond.) **116**, 449 (1952).

[25] A. L. Hodgkin, Proc. R. Soc. Lond. B **148**, 1 (1958).

[26] M. Born, *Natural Philosophy of Cause and Chance; being the Waynflete Lectures, Delivered in the College of St. Mary Magdalen, Oxford, in Hilary Term, 1948* (Dover Publications, New York, 1964).

[27] F. Rieke, D. Warland, R. de Ruyter van Steveninck, and W. Bialek, *Spikes: Exploring the Neural Code* (MIT Press, Cambridge, MA, 1997).

[28] P. Dayan and L. F. Abbot, *Theoretical Neuroscience: Computational and Mathematical Modeling of Neural Systems* (MIT Press, Cambridge, MA, 2001).

[29] Volterra, *Theory of Functionals* (Blackie and Son, Ltd., London, 1930), pp. 25–26.

[30] E. Neher and B. Sakmann, Nature **260**, 799 (1976).

[31] G. Benison, J. Keizer, L. M. Chalupa, and D. W. Robinson, J. Theor. Biol. **210**, 187 (2001).

[32] F. E. Theunissen *et al.*, Comput. Neural Syst. **12**, 289 (2000).